Performance Analysis of Hybrid Optical Wireless and Radio Frequency Communication Systems

by

Tamer Rakia
B.Sc., Military Technical College, 2002
M.Sc., Military Technical College, 2011

A Dissertation Submitted in Partial Fulfillment of the
Requirements for the Degree of

DOCTOR OF PHILOSOPHY

in the Department of Electrical and Computer Engineering

University of Victoria

Performance Analysis of Hybrid Optical Wireless and Radio Frequency Communication Systems

by

Tamer Rakia
B.Sc., Military Technical College, 2002
M.Sc., Military Technical College, 2011

Supervisory Committee

Dr. Hong-Chuan Yang, Co-Supervisor
(Department of Electrical and Computer Engineering)

Dr. Fayez Gebali, Co-Supervisor
(Department of Electrical and Computer Engineering)

Dr. Wu-Sheng Lu, Departmental Member
(Department of Electrical and Computer Engineering)

Dr. Yang Shi, Outside Member
(Department of Mechanical Engineering)

Supervisory Committee

Dr. Hong-Chuan Yang, Co-Supervisor
(Department of Electrical and Computer Engineering)

Dr. Fayez Gebali, Co-Supervisor
(Department of Electrical and Computer Engineering)

Dr. Wu-Sheng Lu, Departmental Member
(Department of Electrical and Computer Engineering)

Dr. Yang Shi, Outside Member
(Department of Mechanical Engineering)

ABSTRACT

In this thesis, we analyze the performance of heterogeneous wireless communication systems that are composed of Optical Wireless Communication (OWC) and Radio Frequency (RF) systems. OWC systems further include long range outdoor Free Space Optical (FSO) systems and short range indoor Visible Light Communication (VLC) systems.

Hybrid FSO/RF systems have emerged as a promising solution for high data rate wireless transmissions. Various transmission schemes including switch-over and soft-switching had been presented for hybrid FSO/RF systems. To overcome the drawbacks of existing schemes, we present a new transmission strategy for hybrid FSO/RF systems exploring an adaptive combining technology. This new strategy shows an improved outage performance. Typically, when the transmitter and the receiver are provided with channel state information, the transmission schemes can be adaptively designed allowing the channel to be used more efficiently. We present two new joint adaptive transmission schemes for hybrid FSO/RF systems. The first one is joint adaptive modulation and adaptive combining scheme which improves the spectral efficiency of hybrid FSO/RF systems. The other one is joint power adaptation and adaptive combining scheme which improves the throughput and the outage performance of hybrid FSO/RF systems. We accurately evaluate the performance of both schemes. FSO technology can be used effectively in multiuser scenarios to support Point-to-Multi-Point (P2MP) networks. In P2MP networks, FSO links are used for data transmission from a central location to multiple users. In this thesis, we present a new P2MP network based on hybrid FSO/RF transmission system. A common backup RF link is used by the central station for data transmission to any user in case of the failure of its corresponding FSO link. Based on a Markov Chain formulation, we study the performance of the resulting system. P2MP Hybrid FSO/RF network achieves considerable performance improvement over the P2MP FSO-only network.

In VLC, Light Emitting Diode (LED) is used for the purpose of simultaneous illumination and data communication at high data rate. However, the light originating from a LED source is naturally confined to a small area and is susceptible to blockages. Hybrid VLC/RF systems have been emerged as a promising solution to provide enhanced communication coverage. We introduce a new dual-hop VLC/RF system with energy harvesting relay to extend the coverage of indoor wireless system based on VLC. The second-hop RF transmission uses the harvested energy over the first-hop VLC transmission. In this thesis, we propose two different approaches for energy harvesting at the relay terminal. In the first approach, the relay harvests light energy from different artificial light sources and sunlight entering the room. In this approach, we propose a novel statistical model for the harvested electrical power and analyze the probability of data packet loss. In the second approach, the relay harvests energy from the VLC link by extracting the direct current component of the received optical signal. In this approach, we investigate the optimal design of the hybrid VLC/RF system in terms of data rate maximization. In both cases, we present extensive numerical examples to define important design guide lines for VLC/RF systems.

Contents

List of Tables

List of Figures

List of Abbreviations

AP	Access Point
AWGN	Additive White Gaussian Noise
BER	Bite Error Rate
CSI	Channel State Information
CDF	Cumulative Distribution Function
CM	Coherent Modulation
DC	Direct Current
DD	Direct Detection
FSO	Free Space Optical
HD	Heterodyne Detection
IM	Intensity Modulation
IR	Infra Red
LED	Light Emitting Diode
Li-Fi	Light-Fidelity
LO	Local Oscillator
MMW	Milli-Meter Wavelength
MRC	Maximal Ratio Combining
OWC	Optical Wireless Communication
P2MP	Point-to-Multi-Point
PAT	Pointing, Acquisition and Tracking

PDF	Probability Density Function
PPL	Phase Locked Loop
PSK	Phase Shift Keying
QAM	Quadrature Amplitude Modulation
QoS	Quality of Service
RF	Radio Frequency
TCI	Truncated Channel Inversion
SIM	Subcarrier Intensity Modulation
SNR	Signal-to-Noise Ratio
UV	Ultra Violet
VLC	Visible Light Communication
WISP	Wireless Internet Service Provider

ACKNOWLEDGMENTS

In the name of Allah, the Most Gracious and the Most Merciful

Alhamdulillah, all praises belongs to Allah the merciful for his blessing and guidance. He gave me the strength to reach what I desire. I would like to thank:

Dr. Hong-Chuan Yang and Dr. Fayez Gebali, for their enthusiasm, guidance, advice, encouragement, and support during my work under their supervision. It would not possible to finish my research without their valuable help of constructive comments and suggestions during all stages of my PhD study.

Dr. Wu-Sheng Lu and Dr. Yang Shi, for their willingness to serve on my supervisory committee. I really appreciate their valuable time and constructive comments on my thesis.

Also, I would like to thank:

Dr. Lutz Lampe from University of British Columbia for serving as my external examiner. It is my great honor to have such an expert on my committee.

Finally, I would like to thank:

My parents and my family for their patience, understanding, support, love and continuing encouragement over all these years.

DEDICATION

To my parents

for their continuous guidance and dedication

To my lovely wife

for her love and support

PREFACE

This thesis is based on the publications listed below.

Journal Publications

J1. **T. Rakia**, H.-C. Yang, M.-S. Alouini, and F. Gebali, "Outage Analysis of Practical FSO/RF Hybrid System with Adaptive Combining", *IEEE Communication Letters*, vol. 19, no. 8, pp. 1366–1369, August 2015.

J2. **T. Rakia**, H.-C. Yang, M.-S. Alouini, and F. Gebali, "Power Adaptation Based on Truncated Channel Inversion for Hybrid FSO/RF Transmission with Adaptive Combining", *IEEE Photonics Journal*, vol. 7, no. 4, pp. 1–12, August 2015.

Conference Publications

C1. **T. Rakia**, H.-C. Yang, F. Gebali, and M.-S. Alouini, "Joint Adaptive Modulation and Combining for Hybrid FSO/RF Systems", *15th IEEE International Conference on Ubiquitous Wireless Broadband, ICUWB'2015* , Montreal, Canada, 2015.

C2. **T. Rakia**, H.-C. Yang, F. Gebali, and M.-S. Alouini, "Outage Performance of Hybrid FSO/RF System with Low-Complexity Power Adaptation", *IEEE Global Communications Conference, Globecom'2015*, San Deigo, USA, 2015.

Journal Publications (accepted)

AJ1. **T. Rakia**, H.-C. Yang, F. Gebali, and M.-S. Alouini, "Optimal Design of Dual-Hop VLC/RF Communication System with Energy Harvesting", *IEEE Communication Letters*, accepted for publication.

Journal Publications (submitted)

SJ1. **T. Rakia**, F. Gebali, H.-C. Yang, and M.-S. Alouini, "Cross Layer Analysis of Point-to-Multi-Point Hybrid FSO/RF Network", *Journal of Optical Communications and Networking*, submitted for publication.

Conference Publications (submitted)

SC1. **T. Rakia**, H.-C. Yang, F. Gebali, and M.-S. Alouini, “Dual-Hop VLC/RF Transmission System with Energy Harvesting Relay under Delay Constraint”, *IEEE Global Communications Conference (Globecom’2016) Workshops*, submitted for publication.

Chapter 1

Introduction

1.1 Background

Optical Wireless Communication (OWC) refers to data transmission in unguided propagation media through the use of an optical carrier. OWC are categorized into three main types, which are Free-Space Optical (FSO) communications, Visible Light Communications (VLC), and Ultra-Violet (UV) Communications. FSO communications and UV Communications use the Infra-Red (IR) band (750 nm - 1600 nm) and the UV band (200 nm - 280 nm), respectively, to allow for outdoor long and short ranges data transmission [1, 2]. On the other hand, VLC - also known as Li-Fi for Light-Fidelity - uses the visible light band (380 nm - 780 nm) to allow for indoor short range data transmission [3].

1.2 Literature Review and Motivation

1.2.1 Free-Space Optical Communications

FSO technology has gained an increasing interest in implementing point-to-point data transmission links, owing to its high data rate, high transmission security, large unregulated spectrum, compared to Radio Frequency (RF) technology, and fast and cheap deployment, compared to fiber optics [4]. Point-to-point FSO links had found their way in many terrestrial and satellite applications. FSO links can be used to connect one Local Area Network (LAN) to another LAN and connect them to Backbone networks, typically implemented with optical fibers as shown in Fig. 1.1 [5], where the black arrows are FSO links. FSO links can be used also as a robust outdoor backhaul

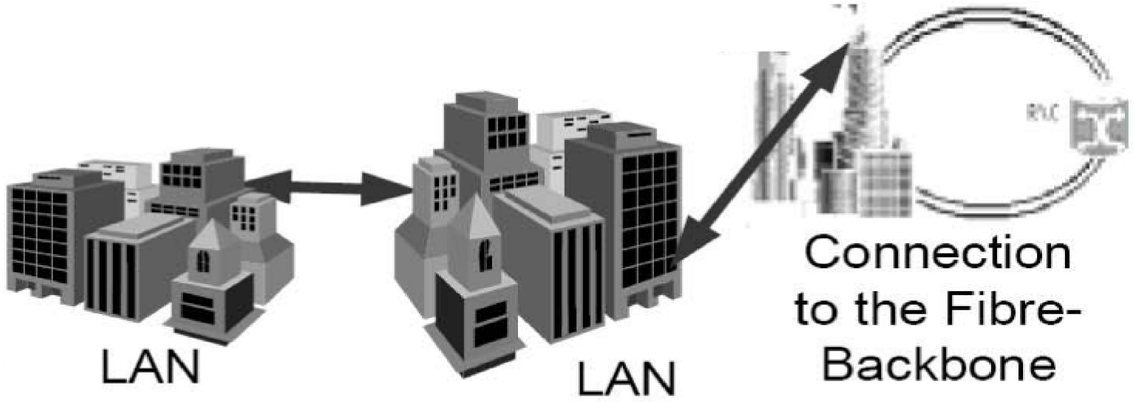

Figure 1.1: LAN-to-LAN FSO connectivity © 2005 IEEE

solution for small radio cells, such as WiFi, LTE and 5G as shown in Fig. 1.2 [6], where the red arrows are FSO links. Other terrestrial applications of FSO include

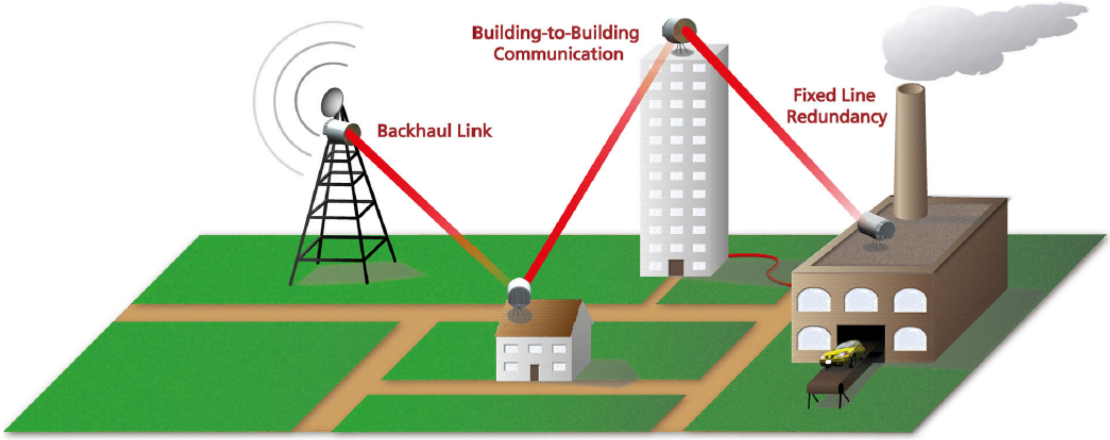

Figure 1.2: Point-to-point backhaul FSO link © 2016 IEEE

last-mile applications to connect end users to a broadband network backbone [7], recovery links for a network which is partially disconnected due to natural disasters [8] and wireless video surveillance and monitoring [9]. Satellite applications of FSO include inter-satellite communications [10] and data transmission between the satellite and the ground stations [11]. We focus on terrestrial applications in this thesis.

An FSO transmission system consists of an optical transmitter and an optical receiver which uses the atmosphere as the transmission media for the optical signal (specifically, a laser beam) as shown in Fig. 1.3. FSO systems are categorized according to the type of detection into Intensity Modulation/Direct Detection (IM/DD)

FSO systems [12] and Coherent Modulation/Heterodyne Detection (CM/HD) FSO systems [13].

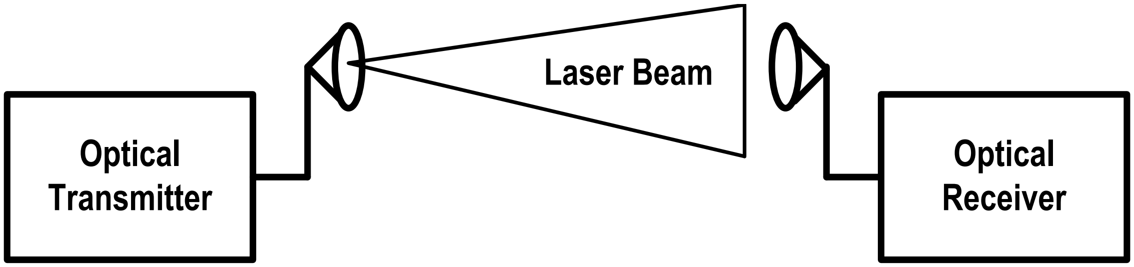

Figure 1.3: FSO system block diagram

The optical signal transmitting through the atmosphere is greatly affected by fading due to atmospheric turbulences and pointing errors [14–18] as shown in Fig. 1.4 [19]. Turbulence-induced fading, known as scintillation, causes irradiance fluctuations in the received optical signal as a result of variations in the atmospheric refractive index [20]. Dynamic wind loads and weak earthquakes can cause vibrations of the transmitted optical beam, which also causes random irradiance fluctuations in the received optical signal. Moreover, the optical power is attenuated as the distance between the transmitter and the receiver increases due to a constant atmospheric loss [17].

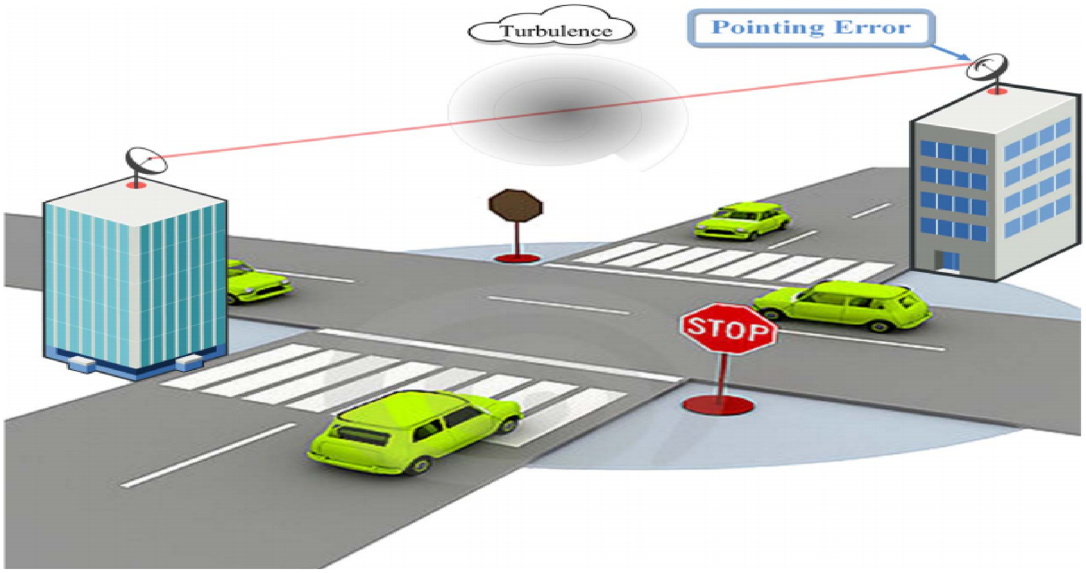

Figure 1.4: Atmospheric turbulence and pointing error in FSO system © 2014 IEEE

Hybrid FSO/RF Implementation

Integrating the FSO link with a Milli-Meter wavelength (MMW) RF link, to form what is known as hybrid FSO/RF system, improves the performance of FSO links. This is owed to the fact that FSO and RF links are affected quite differently by atmospheric and weather effects. FSO links suffer from extremely high attenuation in the presence of fog but are less affected by rain. In contrast, fog has practically no effect on MMW RF links but rain significantly increases link attenuation. Similarly, while atmospheric turbulence is the main cause of small–scale fading in FSO links [20], RF links are impaired by fading due to multipath propagation [21]. Besides the high data rates comparable to FSO links, MMW RF links offer other similar advantages to FSO links of deployment flexibility, license free operation, and inherent security due to high link attenuation.

This complementary nature of FSO and MMW RF links has led to various approaches in implementing hybrid FSO/RF data transmission systems. Two main approaches had been presented in implementing hybrid FSO/RF systems. One approach is the switch-over hybrid FSO/RF scheme, which applies hardware switching between FSO and MMW RF links [22]. However, this approach will lead to frequent hardware switching between the FSO and RF links [23]. Another approach is to use both FSO and RF links for data transmission all the time. One way in this approach, is to transmit identical data simultaneously on both links and apply diversity combining techniques to received signals from both links [24, 25]. In this way, the system's data rate is limited to the lower rate of RF link. Another way, is to divide the coded data stream between the two links, which may have a significant improvement on total system capacity [26]. In general, this soft-switching approach requires FSO and RF links to be active continuously, even when FSO link has very good quality and can support the required bit-error rate by itself. In this scenario, RF transmission power is wasted and system generates unnecessary RF interference to the environment.

These drawbacks of previously presented hybrid FSO/RF systems had motivated us to develop a new scheme for hybrid FSO/RF transmission. This scheme is called hybrid FSO/RF transmission with adaptive combining [27]. In this scheme, FSO link is used alone for data transmission as long as its quality is acceptable and the RF link is put on standby mode. When FSO link's quality becomes unacceptable, the system activates the RF link and applies Maximal Ratio Combining (MRC) scheme on signals received from both FSO and RF links. When the quality of the FSO link alone becomes acceptable again, the RF link is put on standby mode again to save power and spectrum utilization. Thus, the proposed adaptive combining scheme for hybrid FSO/RF systems: 1) improves communication system's reliability, without suffering from switch-over schemes problems, 2) prevents generation of unnecessary RF interference to the environment, 3) conserves RF power, and 4) benefits from FSO higher data rate most of the time.

Adaptive Transmission

Since both FSO and MMW RF channels typically experience slow-fading [17, 28], the transmitter and the receiver of the hybrid FSO/RF system can adapt to the Channel State Information (CSI), allowing the channel to be used more efficiently over time varying channel conditions. Previously, hybrid FSO/RF systems with link adaptation were introduced in [29] and [30]. In [29], transmitted data frame is divided between the FSO and RF links, where both links are simultaneously active. In this case different symbol rates and modulation schemes are used adaptively in a jointly manner according to each link condition. Although, this link adaptation scheme provides good throughput, transmitting different data on both links does not allow the RF link to support the FSO link when its quality is poor. Moreover, using different symbol rates and modulation schemes for both links add extra hardware complexity to both transmitter and receiver terminals. In [30], switch-over hybrid FSO/RF system with adaptive modulation transmission scheme is introduced, where different sets of modulation schemes are used over FSO and RF links. In this scheme, the data rate of the FSO link is gradually reduced, and only switches to RF link in the worst scenario. When the hybrid system uses the RF link alone, transmission rate is also varied according to the RF channel states. Once more, using different modulation schemes sets with both links adds extra hardware complexity to both transmitter and receiver.

Motivated by the previous work in this field and aiming to solve some of drawbacks of the previous presented systems, we present a new joint adaptive modulation and adaptive combining scheme for hybrid FSO/RF system [31]. In this adaptive transmission scheme, the data rate on the FSO link is adjusted in discrete manner according to the FSO link's instantaneous received Signal-to-Noise Ratio (SNR), aiming to achieve the maximum spectral efficiency. If the FSO link's quality is too poor to be able to support the minimum SNR required to satisfy the target Bit-Error-Rate

(BER), the system activates the RF link along with the FSO link. When the RF link is activated, simultaneous transmission of the same modulated data takes place on both links, where the received signals from both links are combined using an MRC scheme. In this case, the data rate of the system is determined in discrete manner according to the instantaneous combined SNRs of both links to maintain the target BER value, while aiming to maximize the system spectral efficiency. When the quality of the FSO link alone becomes acceptable again, the RF link is put on standby mode. Thus, the proposed joint adaptation strategy: 1) provides a low complexity hybrid FSO/RF system with discrete-rate adaptation using the same digital modulation scheme on both links, 2) does not suffer from problems of hardware-switching between the two links [23] that exist in the switch-over scheme [30], and 3) conserves RF power and prevents generation of unnecessary RF interference to the environment by activating the RF link only when is necessary.

Power Adaptation

Power adaptation offers a simple but effective solution to improve link reliability and data throughput, while conserving transmission power [32]. To further improve our hybrid FSO/RF system with adaptive combining, we present a joint power adaptation and adaptive combining scheme for hybrid FSO/RF systems [33, 34]. Previous work on hybrid FSO/RF systems with power adaptation includes [35] and [36]. Particular, [35] considers a hybrid FSO/RF system, in which the system switches to the reliable RF link if the FSO link is obscured to maintain communication, and apply water-filling power adaptation scheme only on the FSO link. In [36], power adaptation has been applied on both FSO and RF links of the hybrid FSO/RF system, assuming that both links are active all the time but transmitting with different rates. The proposed joint adaptive scheme is similar to the adaptive combining scheme [27]. However, when the RF link is activated, the transmit power over the RF link is adapted according to a modified Truncated Channel Inversion (TCI) power adaptation policy, such that the MRC combination of the RF and FSO links maintains a constant received SNR. The proposed joint adaptive combining and power adaptation scheme: 1) improves communication system's reliability by maintaining constant received SNR, while enhancing its outage performance, 2) benefits from FSO higher data rate most of the time, 3) prevents generation of unnecessary RF interference to the environment, 4) conserves RF power, and 5) increases the system outage capacity.

Point-to-Multi-Point Transmission

The interesting and unique features of the FSO systems had motivated a wide range of interest. But most of the current literature is limited to point-to-point data transmissions with FSO technology. On the other hand, FSO can be used effectively in multiuser scenarios [37, 38] to support Point-to-Multi-Point (P2MP) topologies. P2MP topology is a common network architecture for outdoor wireless networks to connect multiple locations to one single central location. In these P2MP networks, FSO links are used for data transmission from a central location to multiple users as in Wireless Internet Service Provider (WISP) networks or the WiMAX networks [39]. In a WISP network, subscribers are connected at the edge of the network using a client device typically mounted on the roof of their houses. The central base station is mounted on a high building where it has line of sight with the client devices.

Motivated by the scarcity in the literature in this field, we present P2MP hybrid FSO/RF network as a new approach in multiuser scenarios. The proposed P2MP hybrid FSO/RF data transmission network consists of a number of remote nodes along with a central node. Each remote node in the network is connected to the central node via a separate primary FSO link. A common backup RF link is shared among all the remote nodes. Using a common RF channel will have the major advantages of: 1) sharing the scarce RF spectrum, 2) preventing the generation of unnecessary RF interference to the environment, and 3) conserving the RF transmission power.

1.2.2 Visible Light Communications

VLC had attracted a lot of attention as an extension for the wireless optical technology in indoor applications [40–43]. In VLC system, the optical signal from a Light Emitting Diode (LED) is used for the purpose of simultaneous illumination and data communication at high data rates [44]. However, the light originating from a LED source is naturally confined to a small area and is susceptible to blockages. Thus, data link may be unreliable when the receiving terminal goes far from the LED. As a solution for this problem, hybrid VLC/RF systems emerged in order to provide enhanced communication coverage [45,46]. In [45], a number of VLC and RF Access Points (AP) are used to improve the coverage and the overall rate performance of the hybrid VLC/RF system. However, each single user may detect the optical intensity from multiple VLC APs which leads to inter-user interferences. These interferences may severely degrade the system performance [47,48]. In [46], VLC is integrated with an RF-based wireless networks to improve the achievable data rates of mobile users.

To extend the coverage of indoor wireless system based on VLC, we introduce a new approach in hybrid VLC/RF systems, which is a dual-hop VLC/RF system as shown in Fig. 1.5. In this approach, a second-hop RF channel is used to extend the coverage of the VLC system. This proposed hybrid VLC/RF system provides coverage within the entire space of the room with only one VLC system and one relay equipped with an RF system, instead of using many VLC and RF systems as introduced in [45]. The proposed system can be used in high data rate Internet access in indoor environment.

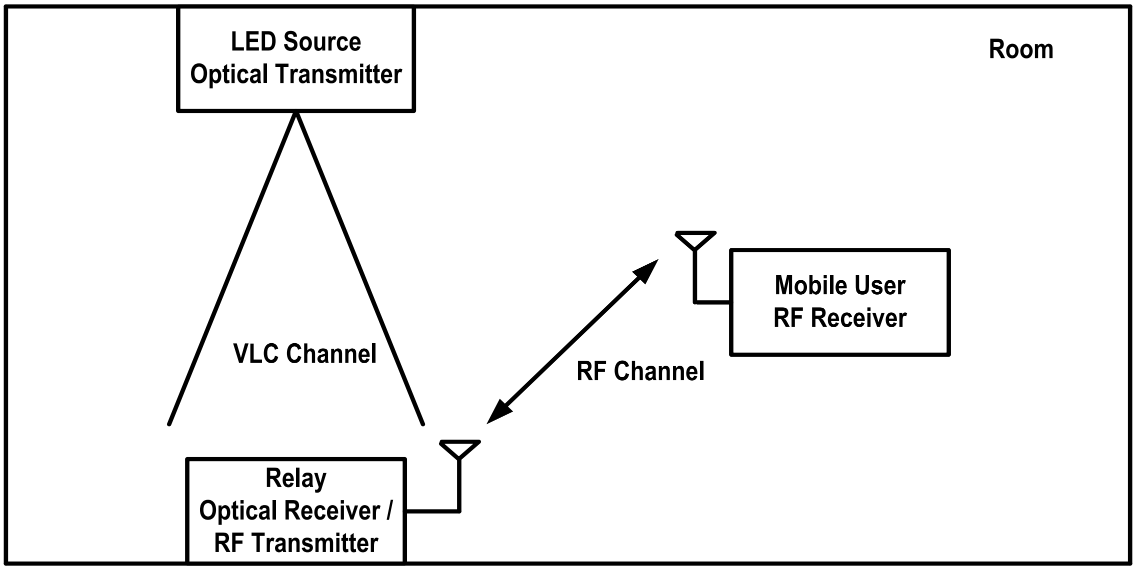

Figure 1.5: Dual-hop VLC/RF system

Recently, harvesting energy from light sources has been introduced in [49], where a solar-panel is used as a passive photo-detector for both information detection and energy harvesting. In order to reduce power consumption, the relay in our proposed dual-hop VLC/RF system is capable of harvesting optical energy and converts it into electrical energy [50, 51]. The relay uses the harvested energy to retransmit the data received over the first-hop VLC link to a mobile terminal over the second-hop RF link.

1.3 Thesis Organization

This thesis consists of eight chapters. A summary of each remaining chapter and its contributions are presented as follows:

Chapter 2 presents and analyzes a new transmission scheme for the hybrid FSO/RF communication system based on adaptive combining. Specifically, only FSO link is active as long as the instantaneous SNR at the FSO receiver is above a certain threshold level. When it falls below this threshold level, the RF link is activated along with the FSO link and the signals from the two links are combined at the receiver using a dual-branch MRC scheme. Novel analytical expression for the Cumulative Distribution Function (CDF) of the received SNR for the proposed hybrid system is obtained. This CDF expression is used to study the system outage performance. This chapter has been included in a published journal article [J1].

In Chapter 3, we present and analyze a new transmission scheme for hybrid FSO/RF communication system based on joint adaptive modulation and adaptive combining. Specifically, the data rate on the FSO link is adjusted in discrete manner according to the FSO link's instantaneous received SNR. If the FSO link's quality is too poor to maintain the target BER, the system activates the RF link along with the FSO link. When the RF link is activated, simultaneous transmission of the same modulated data takes place on both links, where the received signals from both links are combined using MRC scheme. In this case, the data rate of the system is adjusted according to the instantaneous combined SNRs. Novel analytical expression for the CDF of the received SNR for the proposed adaptive hybrid system is obtained. This CDF expression is used to study the spectral and outage performances of the proposed adaptive hybrid FSO/RF system. This chapter has been included in a published conference article [C1].

In chapter 4, we present power adaptation strategies based on TCI for hybrid FSO/RF system employing adaptive combining. Specifically, we adaptively set the RF link transmission power when FSO link quality is unacceptable to ensure constant combined SNR at receiver. Two adaptation strategies are proposed. One strategy depends on the received RF SNR, while the other one depends on the combined SNR of both links. Analytical expressions for the outage probability of the hybrid system with and without power adaptation are obtained. This chapter has been included in a published journal article [J2] and published conference article [C2].

In chapter 5, we present and analyze a P2MP network that uses a number of FSO links for data transmission from the central node to the different remote nodes of the network. A common backup RF link can be used by the central node for data transmission to any remote node in case of the failure of any one of the FSO links. Each remote node is assigned a transmit buffer at the central node. Considering the transmission link from the central node to a tagged remote node, we study various performance metrics. Specifically, we study the throughput from central node to the tagged node, the average transmit buffer size, the symbol queuing delay in the transmit buffer, the efficiency of the queuing system, the symbol loss probability, and the RF link utilization. We compare the performance of the proposed P2MP hybrid FSO/RF network with that of a P2MP FSO-only network. This chapter has been included in a submitted journal article [SJ1].

In chapter 6, we introduce a dual-hop VLC/RF transmission system to extend the coverage of indoor VLC systems. The relay between the two hops is able to harvest light energy from different artificial light sources and sunlight entering the room. The relay receives data packet over a VLC channel and uses the harvested energy to retransmit it to a mobile terminal over an RF channel. We propose a novel statistical model for the harvested electrical power and analyze the probability of data packet loss. This chapter has been included in a submitted conference article [SC1].

In chapter 7, we consider the same dual-hop heterogeneous VLC/RF communication system with energy harvesting relay that was introduced in chapter 6. However, we propose in this chapter a different technique for energy harvesting at the relay terminal. The relay is able to extract the Direct Current (DC) component of the received optical signal over the VLC link and uses it to retransmit the data to a mobile terminal over the second-hop RF link. We investigate the optimal design of the hybrid system in terms of data rate maximization. This chapter has been included in a revised journal article [AJ1].

Finally, we summarize the thesis in Chapter 8 and suggest some further research topics related to this thesis.

1.4 Research Methodology

There are in general two approaches to evaluate the performance of hybrid OWC/RF systems with different proposed transmission schemes under the effects of fading and path losses in OWC and RF links. One approach is to conduct experiments, which are typically costly and time consuming. On the other hand, analytical system performance evaluation can be good alternative to experiments, and the obtained numerical results can be used efficiently at the beginning stage of system design. In this thesis, we will focus on efficient analytical performance evaluation of the proposed hybrid OWC/RF systems, which will provide important engineering insights into hybrid OWC/RF systems design.

1.5 Thesis Contributions

1.5.1 Contributions in FSO Communications Field

- Contributions of chapter 2:
    - Novel transmission scheme for hybrid FSO/RF communications system based on adaptive combining scheme is proposed.
    - Novel analytical expression for the cumulative distribution function of the received SNR for the proposed hybrid system is obtained.
    - The outage performance of the proposed hybrid FSO/RF system with adaptive combing is studied .
    - The proposed hybrid FSO/RF system with adaptive combing had shown superior outage performance, compared to other FSO systems.
- Contributions of chapter 3:
    - Novel transmission scheme for hybrid FSO/RF communication system based on joint adaptive modulation and adaptive combining is proposed.
    - Novel analytical expression for the CDF of the received SNR for the proposed joint adaptive hybrid system is obtained.
    - Spectral and outage performances of the proposed system are studied.
    - The proposed joint adaptive hybrid FSO/RF system had shown superior spectral and outage performances, compared to other hybrid FSO/RF systems.
- Contributions of chapter 4:
    - Novel transmission scheme for hybrid FSO/RF communication system based on joint power adaptation and adaptive combining is proposed.

  - Practical power adaptation strategies are proposed.
  - The corresponding analytical expressions for the outage probability of the proposed joint adaptive hybrid system are obtained.
  - The proposed joint adaptive hybrid FSO/RF system had shown superior outage performances, compared to other hybrid FSO/RF systems.

- Contributions of chapter 5:
  - Novel P2MP hybrid FSO/RF network is proposed.
  - Cross layer Markov chain model of the proposed network is developed.
  - The main parameters affecting the performance of the proposed P2MP hybrid FSO/RF network are identified.
  - Several performance metrics are studied.

1.5.2 Contributions in VLC Field

- Contributions of chapter 6:
  - Novel hybrid VLC/RF transmission system setup with a light energy harvesting relay is presented.
  - Novel statistical model for the electrical power harvested from indoor light energy is presented.
  - Packet loss probability under hard delay constraint for overall system is analyzed.
  - Optimal design of energy harvesting and packet transmission duration for the second hop is done.

- Contributions of chapter 7:
  - Novel dual-hop VLC/RF transmission system setup with a relay harvesting the bias component from the received optical signal over the first hop VLC transmission is proposed.
  - Two novel strategies for optimal bias design of the proposed system are introduced.
  - The corresponding end-to-end average data rate of the system is analyzed in every case of the two strategies.

Chapter 2

Practical FSO/RF Hybrid System with Adaptive Combining

In this chapter, we present a new scheme for hybrid FSO/RF transmission systems. We name this scheme hybrid FSO/RF transmission system with adaptive combining. In this scheme, FSO link is used alone as long as its quality is acceptable. When FSO link's quality becomes unacceptable, the system activates the RF link, and applies MRC scheme on signals received from both FSO and RF links. When the quality of the FSO link alone becomes acceptable again, the RF link is deactivated to save power and spectrum utilization. We drive the CDF of the receiver SNR, which is then used to study the outage performance of the proposed hybrid adaptive scheme.

The remainder of the chapter is organized as follows. In section 2.1, we introduce the model of the hybrid FSO/RF transmission system with adaptive combining scheme. In section 2.2, we deduce the CDF of the receiver SNR and study the outage performance of the proposed adaptive combining scheme. Finally, section 2.3 presents some numerical examples to investigate the performance of the proposed scheme, followed by the chapter summary in section 2.4.

2.1 Hybrid FSO/RF System with Adaptive Combining Modeling

We consider a hybrid FSO/RF system as shown in Fig. 2.1, where only the FSO link is active as long as its instantaneous SNR at the optical receiver, denoted by γ_{FSO}, is above a certain threshold, defined by γ_T. When γ_{FSO} falls below the predetermined threshold γ_T, the receiver sends a 1-bit feedback signal to activate the RF link along with the FSO link for simultaneous transmission of the same data. In this case, the data received from both links are combined using an MRC scheme. The receiver SNR, denoted by γ_c, will equal to γ_{FSO} when $\gamma_{FSO} \geq \gamma_T$. On the other hand, when $\gamma_{FSO} < \gamma_T$, γ_c will equal to the sum of γ_{FSO} and γ_{RF}, where γ_{RF} is the receiver instantaneous SNR of the RF link. Thus, this proposed hybrid system with adaptive combining has two modes of operation which are:

- FSO only mode, as long as $\gamma_{FSO} \geq \gamma_T$.
- Combined FSO/RF mode, as long as $\gamma_{FSO} < \gamma_T$.

At the transmitter, the data is modulated using a Phase Shift Keying (PSK) digital modulation scheme, where the PSK modulated signal can be expressed as:

$$x(t) = \sum_k g(t - kT)cos(2\pi f_s t + \phi_k) \tag{2.1}$$

where T denotes the symbol period, f_s is the frequency of the PSK subcarrier which must satisfy $f_s = q/T$ with $q \geq 1$, $g(t)$ is the shaping pulse, and $\phi_k \in [0, ..., (M-1)\frac{2\pi}{M}]$ is the phase of the kth transmitted symbol with M is the modulation order, which depends upon the bit transmission rate R_b according to $R_b = \log_2(M)/T$. This PSK modulated signal is available for transmission through both FSO and RF links.

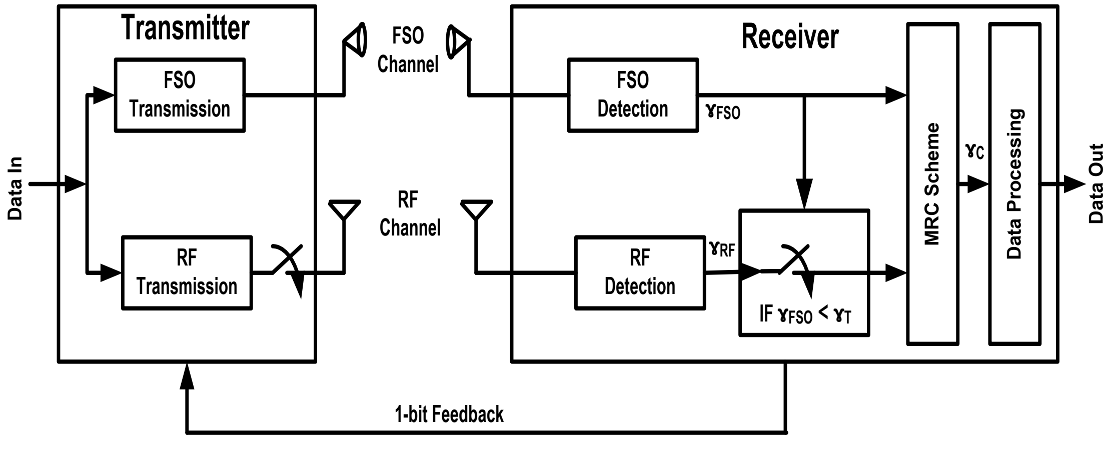

Figure 2.1: Hybrid FSO/RF system with adaptive combining

2.1.1 Modeling the FSO Link

We adopt for the FSO link Sub-carrier Intensity Modulation/Direct Detection (SIM/DD) system [52]. In such system, a DC bias is added to the PSK modulated signal to satisfy non-negativity input constraint of IM/DD systems, before it is used to modulate the intensity of the optical signal, specifically, a laser beam. Hence, the intensity of the transmitted optical signal can be written as [24]:

$$I(t) = P_{FSO}[1 + \mu x(t)], \tag{2.2}$$

where P_{FSO} is the transmitted optical power and μ is the modulation index ($0 < \mu < 1$) that ensured that the laser avoids over-modulation induced clipping.

At the FSO receiver, direct detection of the optical signal takes place, and then further demodulation of the sub-carrier follows to retrieve the data. After filtering the DC bias, the received discrete-time equivalent electrical signal can be modeled as [24]:

$$r_{FSO}[k] = \mu\eta P_{FSO} h_{FSO} G_{FSO} \sqrt{E_s} x[k] + n_{FSO}[k] \tag{2.3}$$

where η is the optical-to-electrical efficiency, $x[k] = \cos\phi_k +$ j $\sin\phi_k$, $E_s = E_g/2$ is the average symbol energy with E_g is the energy of the shaping pulse and $n_{FSO}[k]$ is the shot-noise which is modeled as additive white Gaussian noise (AWGN) with variance σ^2_{FSO}. h_{FSO} is the turbulence induced fading gain over the FSO link, with $E[h_{FSO}]$ normalized to unity, where $E[.]$ is the expectation operator. G_{FSO} is the optical power attenuation, given by Beers-Lambert law as $G_{FSO} = \alpha_{FSO} z$ [26], with α_{FSO} being the weather-dependent attenuation coefficient (in dB/Km) and z is the link range from the transmitter to the receiver. The attenuation G_{FSO} is considered as a fixed scaling factor, and no randomness exists in its behavior [17].

Assuming perfect alignment between FSO transmitter and receiver apertures[1], and considering Gamma-Gamma turbulence-induced fading, h_{FSO} will have the following Probability Density Function (PDF) [20]:

$$f_{h_{FSO}}(h_{FSO}) = \frac{2(\alpha\beta)^{\frac{\alpha+\beta}{2}}}{\Gamma(\alpha)\Gamma(\beta)} h_{FSO}^{\frac{\alpha+\beta}{2}-1} K_{\alpha-\beta}(2\sqrt{\alpha\beta h_{FSO}}) \quad , h_{FSO} \geq 0. \tag{2.4}$$

---

[1] Perfect alignment between FSO transmitter and receiver apertures can be achieved by using Pointing, Acquisition and Tracking (PAT) systems. However, these PAT systems add extra hardware complexity to FSO systems.

where α and β are parameters related to the atmospheric turbulences and $K_\nu(.)$ is the νth order modified Bessel function of the second kind defined as [53, Eq. (8.407)]. Typically, α and β are the effective number of small-scale and large-scale eddies of the turbulent environment, respectively. According to the values of α and β, the atmospheric turbulence can be modeled from weak to strong turbulence regimes because these parameters are directly related to the atmospheric turbulence conditions. Expressions for calculating the parameters α and β for different propagation conditions can be found in [54]. Assuming spherical wave propagation, expressions for calculating α and β in (2.4) are given by [54]:

$$\alpha = \left[\exp\left(\frac{0.49\chi^2}{(1+0.18d^2+0.56\chi^{\frac{12}{5}})^{\frac{7}{6}}}\right)-1\right]^{-1} \tag{2.5}$$

$$\beta = \left[\exp\left(\frac{0.51\chi^2(1+0.69\chi^{\frac{12}{5}})^{-\frac{5}{6}}}{(1+0.9d^2+0.62d^2\chi^{\frac{12}{5}})^{\frac{5}{6}}}\right)-1\right]^{-1} \tag{2.6}$$

where $\chi^2 = 0.5C_n^2k^{7/6}L^{11/6}$ is the Rytov variance and $d = (kD^2/4L)^{1/2}$ with $k = 2\pi/\lambda_{FSO}$ is the optical wave number. Here, C_n^2, D, and λ_{FSO} are respectively the refractive index structure parameter, the diameter of the optical receiver aperture and the optical wavelength.

The instantaneous received electrical SNR of the FSO link is related to h_{FSO} as $\gamma_{FSO} = \bar{\gamma}_{FSO}h_{FSO}^2$ [24], where $\bar{\gamma}_{FSO}$ is the average electrical SNR which is defined as $\bar{\gamma}_{FSO} = E_s\mu^2\eta^2P_{FSO}^2G_{FSO}^2/\sigma_{FSO}^2$ [24]. Using power transformation of random variables, it is easy to show that the PDF of γ_{FSO} is given by:

$$f_{\gamma_{FSO}}(\gamma_{FSO}) = \frac{(\alpha\beta/\sqrt{\bar{\gamma}_{FSO}})^{\frac{\alpha+\beta}{2}}}{\Gamma(\alpha)\Gamma(\beta)}\gamma_{FSO}{}^{\frac{\alpha+\beta}{4}-1}K_{\alpha-\beta}\left(2\sqrt{\frac{\alpha\beta}{\sqrt{\bar{\gamma}_{FSO}}}\gamma_{FSO}{}^{\frac{1}{2}}}\right), \gamma_{FSO} \geq 0. \tag{2.7}$$

By using [55, Eqs. (14)] to express $K_{\alpha-\beta}(.)$ in terms of Meijer G-function $G_{p,q}^{m,n}\left(z \,\middle|\, \begin{smallmatrix} a_1,\ldots,a_p \\ b_1,\ldots,b_q \end{smallmatrix}\right)$ defined as [53, Eq. (9.301)], and [53, Eq. (9.31.5)], (2.7) can be expressed as:

$$f_{\gamma_{FSO}}(\gamma_{FSO}) = \frac{\gamma_{FSO}{}^{-1}}{2\Gamma(\alpha)\Gamma(\beta)}G_{0,2}^{2,0}\left(\frac{\alpha\beta}{\sqrt{\bar{\gamma}_{FSO}}}\gamma_{FSO}{}^{\frac{1}{2}}\,\middle|\, \begin{matrix} - \\ \alpha,\ \beta \end{matrix}\right). \tag{2.8}$$

By using [56, Eq. (07.34.21.0084.01)], and some simple algebraic manipulations, the

CDF of γ_{FSO} can be expressed as:

$$F_{\gamma_{FSO}}(\gamma_{FSO}) = \frac{2^{\alpha+\beta-2}}{\pi\Gamma(\alpha)\Gamma(\beta)} G_{1,5}^{4,1}\left(\frac{(\alpha\beta)^2}{16\bar{\gamma}_{FSO}}\gamma_{FSO} \middle| \begin{matrix} 1 \\ \frac{\alpha}{2}, \frac{\alpha+1}{2}, \frac{\beta}{2}, \frac{\beta+1}{2}, 0 \end{matrix} \right). \tag{2.9}$$

2.1.2 Modeling the RF Link

The electrical PSK-modulated signal, is up-converted to MMW RF (typically, 60 GHz) carrier frequency, to be transmitted over the RF link. The received discrete-time signal, after demodulation process, can be modeled as [24]:

$$r_{RF}[k] = \sqrt{G_{RF}P_{RF}}h_{RF}\sqrt{E_s}x[k] + n_{RF}[k], \tag{2.10}$$

where G_{RF} is the average power gain of the RF link, P_{RF} is the RF transmit power, and h_{RF} is the fading gain over the RF channel, with $E[h_{RF}^2]$ normalized to unity. $n_{RF}[k]$ is the zero-mean circularly symmetric AWGN component with variance σ_{RF}^2. The average power gain G_{RF} is defined as [24]:

$$G_{RF}[dB] = G_T + G_R - 20\log_{10}\left(\frac{4\pi z}{\lambda_{RF}}\right) - \alpha_{oxy}z - \alpha_{rain}z, \tag{2.11}$$

where G_T and G_R denote the transmit and receive antenna gains, respectively and λ_{RF} is the wavelength of the RF subsystem. α_{oxy} and α_{rain} are the attenuations caused by oxygen absorption[2] and rain, respectively. The noise variance in the RF channel is given by $\sigma_{RF}^2 = WN_0N_F$ [24], where W is the RF bandwidth, N_0 is the noise power spectral density and N_F is the noise figure of the RF receiver.

The instantaneous received SNR of the RF link γ_{RF} is given by $\gamma_{RF} = \bar{\gamma}_{RF}h_{RF}^2$, where $\bar{\gamma}_{RF}$ is the average SNR of the RF link defined as $\bar{\gamma}_{RF} = E_sP_{RF}G_{RF}/\sigma_{RF}^2$ [24].

The fading gain h_{RF} is modeled by Nakagami-m distribution, which represents a wide variety of realistic Line-of-Sight (LOS), and Non-LOS (NLOS) fading channels encountered in practice [58]. Accordingly, the received SNR γ_{RF} will have the following PDF [59]:

$$f_{\gamma_{RF}}(\gamma_{RF}) = \frac{\left(\frac{m}{\bar{\gamma}_{RF}}\right)^m {\gamma_{RF}}^{m-1}}{\Gamma(m)} \exp\left(\frac{-m\gamma_{RF}}{\bar{\gamma}_{RF}}\right), \gamma_{RF} \geq 0. \tag{2.12}$$

---

[2] Oxygen absorption at 60 GHz attenuates the signal at all times, regardless of the weather [57].

By using [53, Eq. (3.351.1)], and some simple algebraic manipulations, the CDF of γ_{RF} can be expressed as:

$$F_{\gamma_{RF}}(\gamma_{RF}) = \frac{1}{\Gamma(m)}\gamma\left(m, \frac{m\gamma_{RF}}{\bar{\gamma}_{RF}}\right) \quad , \gamma_{RF} \geq 0, \tag{2.13}$$

where $\gamma(\cdot,\cdot)$ is the lower incomplete Gamma function defined in [53, Eq. (8.350.1)].

2.2 Outage Analysis of Hybrid FSO/RF System with Adaptive Combining

When the instantaneous output SNR γ_c falls below a given threshold γ_{out}, the communication system goes in a state called outage, in which the received SNR can't support the target BER of the system. The probability that the SNR γ_c falls below the outage threshold γ_{out} can be simply calculated by evaluating the CDF of γ_c at γ_{out} as $\mathrm{P}_{out} = F_{\gamma_c}(\gamma_{out})$.

Based on the modes of operation of the proposed hybrid FSO/RF system, the CDF of γ_c, is given by:

$$\begin{aligned} F_{\gamma_c}(x) &= \mathrm{P_r}[\gamma_{FSO} \geq \gamma_T, \gamma_{FSO} < x] + \mathrm{P_r}[\gamma_{FSO} < \gamma_T, \gamma_{FSO} + \gamma_{RF} < x] \\ &= \begin{cases} F_1(x) & \text{if } x \leq \gamma_T \\ F_{\gamma_{FSO}}(x) - F_{\gamma_{FSO}}(\gamma_T) + F_2(x) & \text{if } x > \gamma_T, \end{cases} \end{aligned} \tag{2.14}$$

where $F_1(x)$ is defined as:

$$F_1(x) = \int_0^x f_{\gamma_{FSO}+\gamma_{RF}}(y)dy, \tag{2.15}$$

and $F_2(x)$ is defined as:

$$F_2(x) = \int_0^{\gamma_T} f_{\gamma_{FSO}}(\gamma_{FSO})F_{\gamma_{RF}}(x - \gamma_{FSO})d\gamma_{FSO}, \tag{2.16}$$

with $F_{\gamma_{FSO}}(.)$, and $F_{\gamma_{RF}}(.)$ are given by (2.9), and (2.13) respectively.

Noting that the FSO and RF links are statistically independent, $f_{\gamma_{FSO}+\gamma_{RF}}(y)$ in

(2.15) can be evaluated as:

$$f_{\gamma_{FSO}+\gamma_{RF}}(y)=\int_{0}^{y} f_{\gamma_{FSO}}(\gamma_{FSO})f_{\gamma_{RF}}(y-\gamma_{FSO})d\gamma_{FSO}. \tag{2.17}$$

After substituting (2.8) and (2.12) into (2.17) and applying the binomial expansion defined in [53, Eq. (1.111)], and the series expansion of the exponential defined in [53, Eq. (1.211.1)], along with [56, Eq. (07.34.21.0084.01)], $f_{\gamma_{FSO}+\gamma_{RF}}(y)$ can be evaluated as:

$$\begin{aligned} f_{\gamma_{FSO}+\gamma_{RF}}(y) =& \frac{2^{\alpha+\beta-2}e^{\frac{-my}{\bar{\gamma}_{RF}}}(\frac{m}{\bar{\gamma}_{RF}})^{m}y^{m-1}}{\pi\Gamma(\alpha)\Gamma(\beta)\Gamma(m)}\Bigg\{\sum_{n=0}^{\infty}\frac{(\frac{my}{\bar{\gamma}_{RF}})^{n}}{n!}\sum_{i=0}^{m-1}\binom{m-1}{i} \\ & \times(-1)^{i}G_{1,5}^{4,1}\left(\frac{(\alpha\beta)^{2}y}{16\bar{\gamma}_{FSO}}\ \Big|\ {K_1 \atop K_2}\right)\Bigg\}, \end{aligned} \tag{2.18}$$

where $K_1 = 1-n-i$ and $K_2=\frac{\alpha}{2},\frac{\alpha+1}{2},\frac{\beta}{2},\frac{\beta+1}{2},-n-i$.

Substituting with (2.18) in (2.15), using the series expansion of the exponential, and applying [55, Eq. (26)], $F_1(x)$ can be expressed as:

$$\begin{aligned} F_1(x) =& \frac{2^{\alpha+\beta-2}(\frac{mx}{\bar{\gamma}_{RF}})^{m}}{\pi\Gamma(\alpha)\Gamma(\beta)\Gamma(m)}\Bigg\{\sum_{n=0}^{\infty}\frac{(\frac{mx}{\bar{\gamma}_{RF}})^{n}}{n!}\sum_{i=0}^{m-1}\binom{m-1}{i}(-1)^{i}\sum_{k=0}^{\infty}\frac{(\frac{-mx}{\bar{\gamma}_{RF}})^{k}}{k!} \\ & \times G_{2,6}^{4,2}\left(\frac{(\alpha\beta)^{2}x}{16\bar{\gamma}_{FSO}}\ \Big|\ {K_3 \atop K_4}\right)\Bigg\}, \end{aligned} \tag{2.19}$$

where $K_3 = 1-n-i, 1-k-n-m$ and $K_4=\frac{\alpha}{2},\frac{\alpha+1}{2},\frac{\beta}{2},\frac{\beta+1}{2},-k-n-m,-n-i$.

Substituting with (2.8) and (2.13) in (2.16), $F_2(x)$ can be expressed in the integral form as:

$$F_2(x)=\int_{0}^{\gamma_T}\frac{\gamma(m,\frac{m(x-\gamma_{FSO})}{\bar{\gamma}_{RF}})\gamma_{FSO}{}^{-1}}{2\Gamma(\alpha)\Gamma(\beta)\Gamma(m)}G_{0,2}^{2,0}\left(\frac{\alpha\beta\gamma_{FSO}{}^{1/2}}{\sqrt{\bar{\gamma}_{FSO}}}\ \Big|\ {- \atop \alpha,\ \beta}\right)d\gamma_{FSO}. \tag{2.20}$$

By using the series representation of $\gamma(\cdot,\cdot)$, defined in [53, Eqs. (8.352.1)], and then applying the binomial expansion rule, along with the series expansion of the exponential, the term $\gamma\left(m, \frac{m(x-\gamma_{FSO})}{\bar{\gamma}_{RF}}\right)$ in (2.20) can be represented by:

$$\begin{aligned}\gamma\left(m, \frac{m(x-\gamma_{FSO})}{\bar{\gamma}_{RF}}\right) = (m-1)!\Bigg[1 - e^{\frac{-mx}{\bar{\gamma}_{RF}}} \sum_{n=0}^{\infty} \frac{\left(\frac{m\gamma_{FSO}}{\bar{\gamma}_{RF}}\right)^n}{n!} \sum_{k=0}^{m-1} \frac{\left(\frac{m}{\bar{\gamma}_{RF}}\right)^k}{k!} \\ \times \sum_{j=0}^{k} \binom{k}{j} x^{k-j} (-\gamma_{FSO})^j\Bigg].\end{aligned} \tag{2.21}$$

By plugging (2.21) in (2.20) and applying [56, Eq. (07.34.21.0084.01)], $F_2(x)$ can be evaluated as:

$$\begin{aligned}F_2(x) = &\frac{(m-1)!}{\Gamma(m)} F_{\gamma_{FSO}}(\gamma_T) - \Bigg\{ \frac{2^{\alpha+\beta-2} e^{\frac{-mx}{\bar{\gamma}_{RF}}} (m-1)!}{\pi\Gamma(\alpha)\Gamma(\beta)\Gamma(m)} \sum_{n=0}^{\infty} \frac{(m\gamma_T/\bar{\gamma}_{RF})^n}{n!} \\ &\times \sum_{k=0}^{m-1} \frac{(mx/\bar{\gamma}_{RF})^k}{k!} \sum_{j=0}^{k} \binom{k}{j} \left(\frac{-\gamma_T}{x}\right)^j G_{1,5}^{4,1}\left(\frac{(\alpha\beta)^2\gamma_T}{16\bar{\gamma}_{FSO}} \,\middle|\, \begin{matrix} K_5 \\ K_6 \end{matrix}\right)\Bigg\},\end{aligned} \tag{2.22}$$

where $K_5 = 1-n-j$ and $K_6 = \frac{\alpha}{2}, \frac{\alpha+1}{2}, \frac{\beta}{2}, \frac{\beta+1}{2}, -n-j$.

Finally, the CDF of γ_c is obtained after substituting (2.19) and (2.22) into (2.14).

2.3 Numerical Results

In this section, we present several numerical examples to illustrate our analysis. We assume fading severity over RF link of m=5. In Figs. 2.2 and 2.3, we consider clear weather condition, which is the hybrid FSO/RF system's operational condition most of the time. We used typical values of α and β for strong atmospheric turbulence ($\alpha = 2.064$, and $\beta = 1.342$ [60]), which has the dominant effect on hybrid system's performance in this case. In Figs. 2.4 and 2.5, we consider adverse weather conditions, mainly fog and rain, which may last shortly. In Fig. 2.4, we assume moderate rain weather condition with weather-dependent attenuation coefficient $\alpha_{FSO} = 5.8$ dB/km, RF rain attenuation coefficient $\alpha_{rain} = 5.6$ dB/km, and $C_n^2 = 5 \times 10^{-15}$ [24]. In Fig. 2.5, we assume light fog weather condition with weather-dependent attenuation coefficient $\alpha_{FSO} = 20$ dB/km, RF rain attenuation coefficient $\alpha_{rain} = 0$ dB/km, and $C_n^2 = 5 \times 10^{-15}$ [17]. The values of FSO and RF sub-systems parameters, used to obtain results in Figs. 2.4 and 2.5 are given in Table 2.1. Assume using binary PSK digital modulation, $\gamma_T = 10.5$ dB to satisfy target BER of 10^{-6}.

It can be seen from Fig. 2.2 that the hybrid FSO/RF system gives much better

Table 2.1: Parameters of FSO and RF subsystems

Parameter	Symbol	Value
FSO Subsystem		
Wavelength	λ_{FSO}	1550 nm
Shot Noise Variance	σ^2_{FSO}	2×10^{-14}
Responsivity	η	0.5 A/W
Photodetector Diameter	D	20 cm
RF Subsystem		
Carrier Frequency	f_{RF}	60 GHz
Bandwidth	W	250 MHz
Transmit Antenna Gain	G_T	43 dBi
Receive Antenna Gain	G_R	43 dBi
Noise Power Spectral Density	N_0	-114 dBm/MHz
Receiver Noise Figure	N_F	5 dB
Oxygen Attenuation	α_{oxy}	15.1 dB/Km

outage performance than using FSO-only or RF-only systems in clear weather conditions. Also, as expected, it can be observed that the performance of the hybrid system is improved with the increase of $\bar{\gamma}_{RF}$. The numerical results shown in Fig. 2.2 are obtained using n=30 and k=30 in (2.19) and n=30 in (2.22). As can be observed from Fig. 2.2, evaluating the outage probability using the truncated values of (2.19) and (2.22) gives accurate results that coincide with the values of the outage probability obtained by evaluating the integrals in (2.15) and (2.16) using numerical methods.

It can be seen from Fig. 2.3 that, when γ_{out} is less than γ_T, the outage performance of the hybrid FSO/RF system is improved, because the system activates RF link before the FSO link goes in outage. In this case, and as expected, outage probability decreases as $\bar{\gamma}_{RF}$ increases. On the other hand, when γ_{out} is greater than γ_T, the outage performance of the hybrid system does not decrease, as the RF link quality improves because the system goes in outage before it activates the RF link.

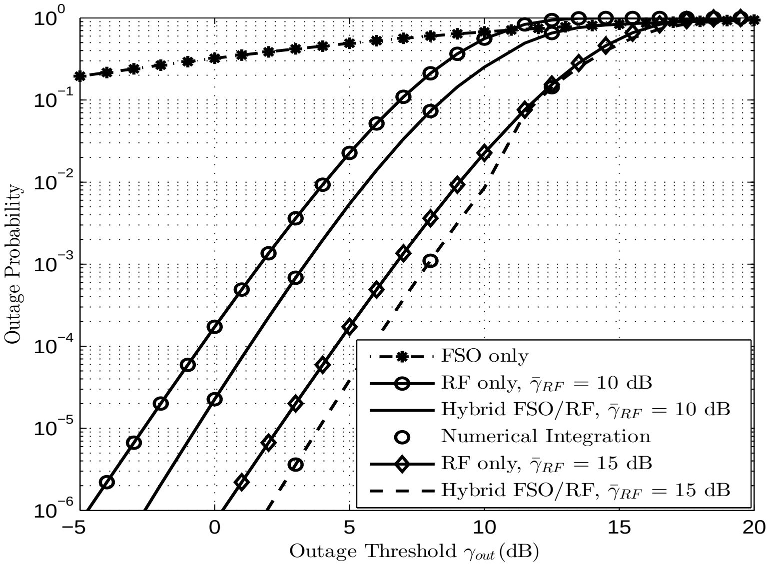

Figure 2.2: Outage probability of a hybrid FSO/RF system as a function of the outage threshold with $\bar{\gamma}_{FSO} = 10$ dB.

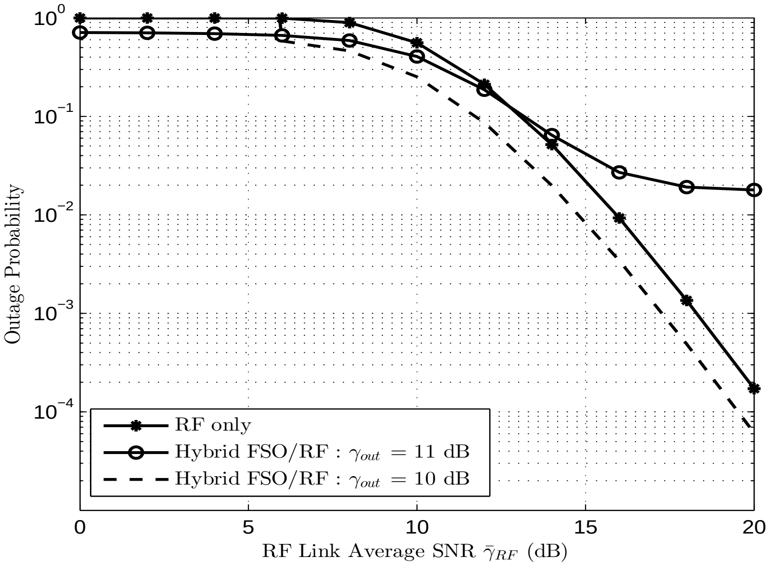

Figure 2.3: Outage probability of a hybrid FSO/RF system as a function of the average SNR of the RF link with $\bar{\gamma}_{FSO} = 10$ dB compared to the RF-only system.

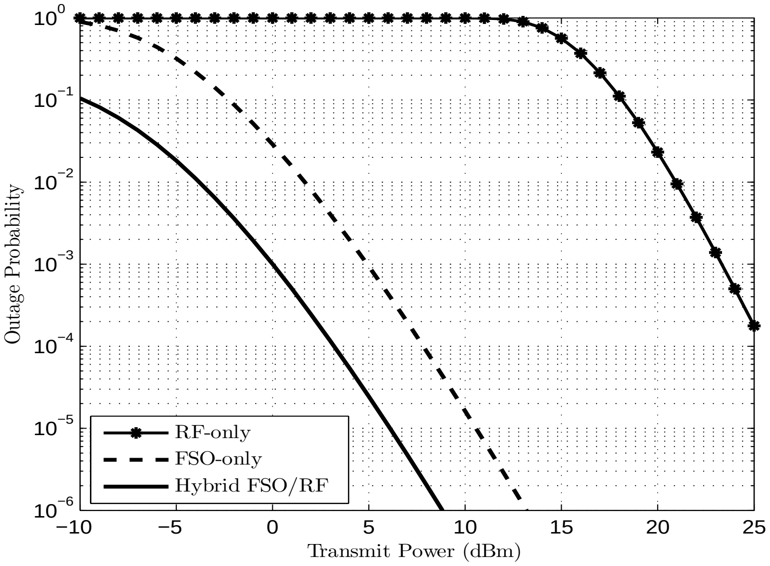

Figure 2.4: Outage probability of a hybrid FSO/RF system as a function of transmit power in moderate rain conditions, with γ_{out}=10 dB, and link range z=4000 m.

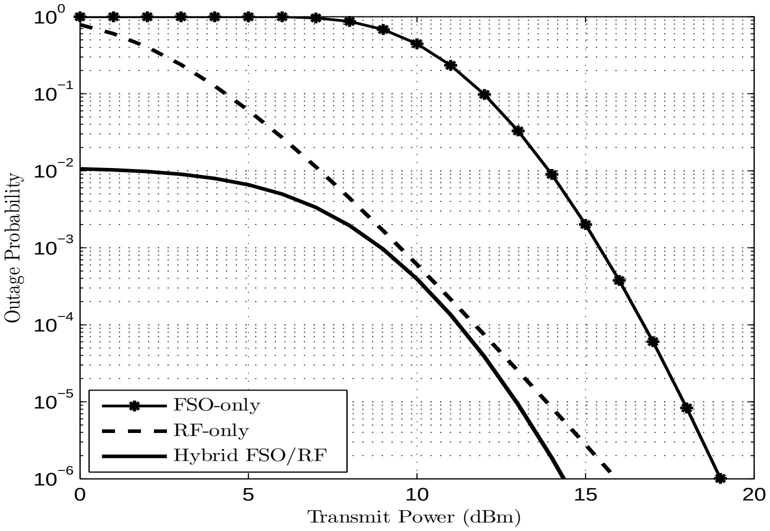

Figure 2.5: Outage probability of a hybrid FSO/RF system as a function of transmit power in light fog conditions, with γ_{out}=10 dB, and link range z=2000 m.

It can be seen from Fig. 2.4 that, FSO link's quality degrades due to weak atmospheric turbulence in rain conditions. As observed, considering the "five nines" reliability criterion which implies an outage performance of 10^{-6}, there is an improvement by using the hybrid system of about 4 dB in transmit power over the FSO-only system.

It can be seen from Fig. 2.5 that, FSO link's quality degrades much in fog conditions. Thus, activating the MMW RF link, which is not affected by fog conditions, greatly improves the outage performance of the hybrid system with an improvement of about 5 dB in transmit power over the FSO-only system considering the "five nines" reliability criterion.

2.4 Summery

In this chapter, we analyzed the performance of a hybrid FSO/RF transmission scheme based on adaptive combining. We offered a closed-form of the exact CDF of the received SNR for the proposed hybrid system, which is used to study its outage performance. Numerical results show that hybrid FSO/RF system with adaptive combining transmission scheme has superior outage performance compared to FSO-only and RF-only systems in all weather conditions and atmospheric turbulence regimes.

Chapter 3

Joint Adaptive Modulation and Combining for Hybrid FSO/RF Systems

In this chapter, we present and analyze a new transmission scheme for hybrid FSO/RF communication system based on joint adaptive modulation and adaptive combining. Specifically, the data rate on the FSO link is adjusted in discrete manner according to the FSO link's instantaneous received SNR. If the FSO link's quality is too poor to maintain the target BER, the system activates the RF link along with the FSO link. When the RF link is activated, simultaneous transmission of the same modulated data takes place on both links, where the received signals from both links are combined using MRC scheme. In this case, the data rate of the system is adjusted according to the instantaneous combined SNRs. We study the spectral and outage performances of the proposed joint adaptive hybrid FSO/RF system.

The remainder of the chapter is organized as follows. In section 3.1, we introduce the system and channel modeling. Subsequently, the performance metrics of the proposed adaptive hybrid system are introduced in section 3.2. Section 3.3 briefly introduces the performance metrics of switch-over hybrid system. Finally, Section 3.4 presents some numerical examples to express the performance of the proposed joint adaptive hybrid system followed by the chapter summary in section 3.5.

3.1 System and Channel Modeling

We consider hybrid FSO/RF system, which is composed of coherent/heterodyne FSO and RF communication subsystems. Coded digital baseband signal, created by signal source, is converted to analog electrical signal through electrical modulator, which can adaptively use one of N different M- square quadrature amplitude modulation (QAM) schemes. M-QAM is widely used in high-rate data transmissions over FSO links [61], and RF links [62], because of its high spectral efficiency, and ease of signal modulation/demodulation process. A particular constellation size M is chosen to achieve the highest possible spectral efficiency, while maintaining the instantaneous BER below the target value of BER_0. Let $\gamma_{T1}, \gamma_{T2}, ..., \gamma_{TN}$ be the N different thresholds corresponding to constellation sizes of $M = 4, 16, ..., 2^{2N}$, respectively such that $\gamma_{T1} < \gamma_{T2} < ... < \gamma_{TN}$. Note that $\gamma_{TN+1} = \infty$. To meet a BER requirement of BER_0, the thresholds are set using [32]:

$$\gamma_{Tn} = (2^{2n} - 1)[-\frac{2}{3}\ln(5\ \text{BER}_0)], \quad n \geq 1, \tag{3.1}$$

where the instantaneous BER of coherent M-QAM of size 2^{2n}, can be well approximated by [32]:

$$BER_n(\gamma_{Tn}) = 0.2 \exp\left(\frac{-1.5}{2^{2n} - 1}\gamma_{Tn}\right), \quad 2^{2n} \geq 4, \quad 0 \leq \gamma_{Tn} \leq 30\text{dB}. \tag{3.2}$$

3.1.1 Modeling the FSO Link

At the FSO transmitter terminal, QAM electrical signal is mixed with an optical carrier, produced by an optical frequency Local Oscillator (LO) to produce the optical signal. At the FSO receiver terminal, the received optical signal under goes heterodyne detection process. The instantaneous SNR per symbol of the FSO receiver is given by [63, 64]:

$$\gamma_{FSO} = \bar{\gamma}_{FSO} h_{FSO}, \tag{3.3}$$

where $\bar{\gamma}_{FSO}$ and h_{FSO} are respectively, the average SNR and the fading gain over the FSO link, with $E[h_{FSO}]$ is normalized to unity, where $E[.]$ is the expectation operator. Assume using phase-locked loop (PLL) to compensate for phase noise in the received optical signal and using large enough LO power, such that thermal and background noises can be neglected [63]. In this case, the average SNR $\bar{\gamma}_{FSO}$ is given by $\bar{\gamma}_{FSO} = 2E_{avg}\eta^2 P_{LO} P_{FSO} G_{FSO}/\sigma^2_{FSO}$ [63, 64], where E_{avg}, η, P_{LO} , P_{FSO}, G_{FSO}, and σ^2_{FSO} are the average QAM symbol energy, photodetector responsivity, LO power, average transmitted optical power, optical power attenuation, and variance of shot noise which is modeled as AWGN, respectively. The shot noise variance σ^2_{FSO} is given by $\sigma^2_{FSO} = 2q\eta P_{LO}/T$ [63], where q is the electronic charge and $1/T$ is the transmission rate in bits/second. The optical power attenuation G_{FSO} is given by Beers-Lambert law as $G_{FSO} = \alpha_{FSO} z$ [26], with α_{FSO} being the weather-dependent attenuation coefficient (in dB/Km) and z is the link range from the transmitter to the receiver. The attenuation G_{FSO} is considered as a fixed scaling factor, and no randomness exists in its behavior [17]. The fading gain is defined as $h_{FSO} = h_a h_p$, where h_a is Gamma-Gamma atmospheric turbulence-induced fading gain factor [54] and h_p is Gaussian pointing errors-induced fading gain factor [17].

Following the same procedure used in [65], it is easy to show that the PDF of γ_{FSO} is given by:

$$f_{\gamma_{FSO}}(\gamma_{FSO}) = \frac{\xi^2 \gamma_{FSO}{}^{-1}}{\Gamma(\alpha)\Gamma(\beta)} G^{3,0}_{1,3}\left[\frac{\xi^2\alpha\beta\gamma_{FSO}}{(\xi^2+1)\bar{\gamma}_{FSO}} \,\Big|^{\xi^2+1}_{\xi^2,\ \alpha,\ \beta}\right], \tag{3.4}$$

where ξ is the ratio between the equivalent beam radius ω_{eq} and the pointing error (jitter) standard deviation σ_s given by $\xi = \omega_{eq}/2\sigma_s$. Here, $\omega^2_{eq} = \omega^2_z \sqrt{\pi}\mathrm{erf}(\nu)/2\nu \exp(-\nu^2)$, where erf(.) is the error function and ω_z is the beam radius calculated at distance z from the transmitter aperture and $\nu = \sqrt{\pi}D/2\sqrt{2}\omega_z$ with D is the photodetector diameter. ω_z is given by $\omega_z = \theta_0 z$, where θ_0 is the transmit divergence at $1/e^2$. $\Gamma(.)$ in (3.4) is the standard Gamma function with α and β are the scintillation parameters that are related to the refractive index structure parameter C^2_n [54]. $G[.]$ is the Meijer G-function as defined in [53, Eq. (9.301)]. By using [56, Eq. (07.34.21.0084.01)] and some simple algebraic manipulations, the CDF of γ_{FSO} can be expressed as:

$$F_{\gamma_{FSO}}(\gamma_{FSO}) = \frac{\xi^2}{\Gamma(\alpha)\Gamma(\beta)} G^{3,1}_{2,4}\left[\frac{\xi^2\alpha\beta\gamma_{FSO}}{(\xi^2+1)\bar{\gamma}_{FSO}} \,\Big|^{1,\ \xi^2+1}_{\xi^2,\ \alpha,\ \beta,\ 0}\right]. \tag{3.5}$$

3.1.2 Modeling the RF Link

At the RF transmitter, QAM electrical signal's frequency is up-converted using 60 GHz RF carrier, produced by RF LO. The instantaneous received SNR from the RF branch, denoted by γ_{RF}, can be given by [24]:

$$\gamma_{RF} = \bar{\gamma}_{RF} h_{RF}^2, \tag{3.6}$$

where h_{RF} is the fading gain over the RF channel, with $E[h_{RF}^2]$ normalized to unity, and $\bar{\gamma}_{RF}$ is the average SNR of the RF channel, given by $\bar{\gamma}_{RF} = E_{avg}P_{RF}G_{RF}/\sigma_{RF}^2$ [24], with E_{avg}, P_{RF}, σ_{RF}^2, and G_{RF} are respectively, average QAM symbol energy, transmitted RF power, noise variance, assuming zero-mean circularly symmetric AWGN, and average power gain of the RF channel, which is given by [24]:

$$G_{RF}[dB] = G_T + G_R - 20\log_{10}\left(\frac{4\pi z}{\lambda_{RF}}\right) - \alpha_{oxy} z - \alpha_{rain} z, \tag{3.7}$$

where G_T and G_R denote the transmit and receive antenna gains, respectively, λ_{RF} is the wavelength of the RF subsystem, α_{oxy} and α_{rain} are the attenuations caused by oxygen absorption and rain, respectively and z is the link distance. The noise variance in the RF channel is given by [24], $\sigma_{RF}^2 = WN_0N_F$, where W is the RF bandwidth, N_0 is the noise power spectral density and N_F is the noise figure of the RF receiver.

The fading gain h_{RF} follows Nakagami-m distribution, which represents a wide variety of realistic LOS and non LOS fading channels encountered in practice [58]. The PDF and CDF of γ_{RF} are respectively given by [59]:

$$f_{\gamma_{RF}}(\gamma_{RF}) = \left(\frac{m}{\bar{\gamma}_{RF}}\right)^m \frac{{\gamma_{RF}}^{m-1}}{\Gamma(m)} \exp\left(\frac{-m\gamma_{RF}}{\bar{\gamma}_{RF}}\right), \tag{3.8}$$

$$F_{\gamma_{RF}}(\gamma_{RF}) = \frac{1}{\Gamma(m)}\gamma\left(m, \frac{m\gamma_{RF}}{\bar{\gamma}_{RF}}\right). \tag{3.9}$$

where $\gamma(\cdot,\cdot)$ is the lower incomplete Gamma function defined in [53, Eq. (8.350.1)].

3.2 Performance Analysis of the Proposed Joint Adaptive Scheme

To achieve the maximum spectral efficiency, the FSO link uses the modulation scheme 2^{2N}-QAM as long as γ_{FSO} is greater than or equal to γ_{T_N}. If γ_{FSO} decreases beyond γ_{T_N}, the receiver checks another threshold γ_{T_n} in a descending order until one threshold satisfies $\gamma_{FSO} \geq \gamma_{T_n}$. In this case, the receiver sends a feedback signal to the transmitter indicating the modulation scheme 2^{2n}-QAM should be used without activating RF subsystem. If the thresholds checking process reaches γ_{T1} and γ_{FSO} is less than γ_{T1}, the receiver sends a feedback signal to activate the RF link along with the FSO link for simultaneous transmission of the same data. Therefore, the feedback required is $\lceil \log_2(N+1) \rceil$ bits for the first stage. At the receiver terminal, the data transmitted along both links will be combined using MRC combiner. In this case, the receiver SNR, denoted by γ_c, will equal to the sum of γ_{FSO} and γ_{RF}. Note that γ_c is equal to γ_{FSO} as long as $\gamma_{FSO} \geq \gamma_{T1}$. To this end, the receiver checks whether γ_c is greater than or equal to γ_{T_N}. If so, the receiver sends a feedback signal for the transmitter to use the modulation scheme 2^{2N}-QAM on both FSO link and RF link. If not, the receiver checks another threshold γ_{T_n} in a descending order until one threshold satisfies $\gamma_c \geq \gamma_{T_n}$. In this case, the receiver sends a feedback signal to the transmitter to select the modulation scheme 2^{2n}-QAM. If the receiver thresholds checking process reaches γ_{T1} and $\gamma_c < \gamma_{T1}$, the receiver sends a signal to suspend data transmission over both FSO and RF links[1]. In this second stage, if necessary, the feedback load is again $\lceil \log_2(N+1) \rceil$ bits. The average feedback of the proposed adaptive hybrid system is $\lceil \log_2(N+1) \rceil \ (1 + \mathrm{P_r}[\gamma_{FSO} < \gamma_{T1}])$ bits. Fig. 3.1 summerizes the joint adaptive modulation and combining operation of the the hybrid FSO/RF system.

Before we study the performance of this joint adaptive scheme, we need to deduce the CDF of γ_c. Based on the modes of operation of this joint adaptive scheme, the CDF of γ_c, is given by:

$$\begin{aligned} F_{\gamma_c}(x) &= \mathrm{P_r}[\gamma_{FSO} \geq \gamma_{T1}, \gamma_{FSO} < x] + \mathrm{P_r}[\gamma_{FSO} < \gamma_{T1}, \gamma_{FSO} + \gamma_{RF} < x] \\ &= \begin{cases} F_1(x), & \text{if } x \leq \gamma_{T1} \\ F_{\gamma_{FSO}}(x) - F_{\gamma_{FSO}}(\gamma_{T1}) + F_2(x), & \text{if } x > \gamma_{T1}, \end{cases} \end{aligned} \tag{3.10}$$

where $F_1(x)$ is defined as:

$$F_1(x) = \int_0^x f_{\gamma_{FSO}+\gamma_{RF}}(y) dy, \tag{3.11}$$

---

[1] When data transmission is suspended, pilot signal is assumed to be continuously transmitted over the FSO link to check its status as it is the main channel of the system that provides high data rate transmission.

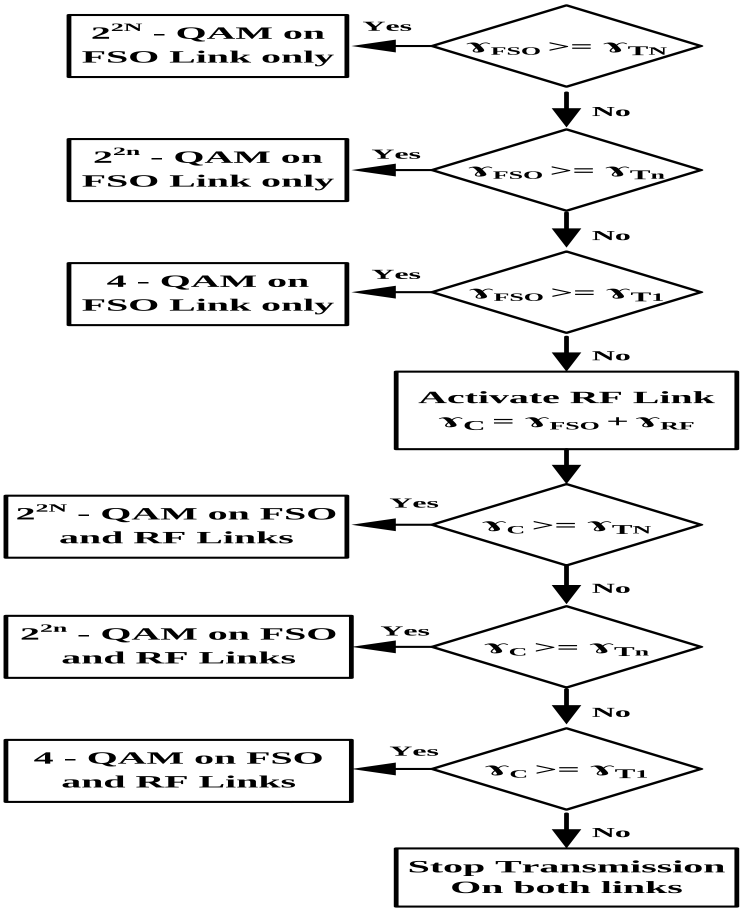

Figure 3.1: Flow chart of the operation of the joint adaptive hybrid FSO/RF scheme.

and $F_2(x)$ is defined as:

$$F_2(x) = \int_{0}^{\gamma_{T1}} f_{\gamma_{FSO}}(\gamma_{FSO}) F_{\gamma_{RF}}(x - \gamma_{FSO}) d\gamma_{FSO}. \tag{3.12}$$

Noting that the FSO and RF links are statistically independent, $f_{\gamma_{FSO}+\gamma_{RF}}(y)$ in (3.11) can be evaluated as:

$$f_{\gamma_{FSO}+\gamma_{RF}}(y) = \int_{0}^{y} f_{\gamma_{FSO}}(\gamma_{FSO}) f_{\gamma_{RF}}(y - \gamma_{FSO}) d\gamma_{FSO}. \tag{3.13}$$

After substituting (3.4) and (3.8) into (3.13) and applying the binomial expansion, and the series expansion of the exponential function, along with [56, Eq. (07.34.21.0084.01)],

$f_{\gamma_{FSO}+\gamma_{RF}}(y)$ can be evaluated as:

$$
\begin{aligned}
f_{\gamma_{FSO}+\gamma_{RF}}(y) = \frac{\xi^2 e^{\frac{-my}{\bar{\gamma}_{RF}}} (\frac{m}{\bar{\gamma}_{RF}})^m y^{m-1}}{\Gamma(\alpha)\Gamma(\beta)\Gamma(m)} \Bigg\{ \sum_{n=0}^{\infty} \frac{(\frac{my}{\bar{\gamma}_{RF}})^n}{n!} \sum_{i=0}^{m-1} \binom{m-1}{i} (-1)^i \\
\times G_{2,4}^{3,1} \left[\frac{\xi^2 \alpha\beta y}{(\xi^2+1)\bar{\gamma}_{FSO}} \;\Big|^{1-n-i,\xi^2+1}_{\xi^2,\alpha,\beta,-n-i} \right] \Bigg\}.
\end{aligned}
\tag{3.14}
$$

Substituting with (3.14) in (3.11), using the series expansion of the exponential function, and applying [56, Eq. (07.34.21.0084.01)], $F_1(x)$ can be expressed as:

$$
\begin{aligned}
F_1(x) = \frac{\xi^2 (\frac{mx}{\bar{\gamma}_{RF}})^m}{\Gamma(\alpha)\Gamma(\beta)\Gamma(m)} \Bigg\{ \sum_{n=0}^{\infty} \frac{(\frac{mx}{\bar{\gamma}_{RF}})^n}{n!} \sum_{i=0}^{m-1} \binom{m-1}{i} (-1)^i \sum_{k=0}^{\infty} \frac{(\frac{-mx}{\bar{\gamma}_{RF}})^k}{k!} \\
\times G_{3,5}^{3,2} \left[\frac{\xi^2 \alpha\beta x}{(\xi^2+1)\bar{\gamma}_{FSO}} \;\Big|^{1-n-i,1-k-n-m,\xi^2+1}_{\xi^2,\alpha,\beta,-k-n-m,-n-i} \right] \Bigg\}.
\end{aligned}
\tag{3.15}
$$

Substituting with (3.4) and (3.9) in (3.12), $F_2(x)$ can be expressed in the integral form as:

$$
F_2(x) = \int_0^{\gamma_{T1}} \frac{\gamma(m, \frac{m(x-\gamma_{FSO})}{\bar{\gamma}_{RF}}) \xi^2 \gamma_{FSO}^{-1}}{\Gamma(\alpha)\Gamma(\beta)\Gamma(m)} \times G_{1,3}^{3,0} \left[\frac{\xi^2 \alpha\beta}{(\xi^2+1)} \frac{\gamma_{FSO}}{\bar{\gamma}_{FSO}} \;\Big|^{\xi^2+1}_{\xi^2,\alpha,\beta} \right] d\gamma_{FSO}. \tag{3.16}
$$

By using the series representation of $\gamma(a,x)$ in (3.16) defined in [53, Eqs. (8.352.1)], and then applying the binomial expansion rule along with the series expansion of the exponential function, the term $\gamma\left(m, \frac{m(x-\gamma_{FSO})}{\bar{\gamma}_{RF}}\right)$ can be represented by:

$$
\begin{aligned}
\gamma\left(m, \frac{m(x-\gamma_{FSO})}{\bar{\gamma}_{RF}}\right) = (m-1)! \Bigg\{ 1 - e^{\frac{-mx}{\bar{\gamma}_{RF}}} \sum_{n=0}^{\infty} \frac{(\frac{m\gamma_{FSO}}{\bar{\gamma}_{RF}})^n}{n!} \sum_{k=0}^{m-1} \frac{(\frac{m}{\bar{\gamma}_{RF}})^k}{k!} \\
\sum_{j=0}^{k} \binom{k}{j} x^{k-j} (-\gamma_{FSO})^j \Bigg\}.
\end{aligned}
\tag{3.17}
$$

By plugging (3.17) in (3.16) and applying [56, Eq. (07.34.21.0084.01)], $F_2(x)$ can be evaluated as:

$$\begin{aligned}F_2(x) =&\frac{(m-1)!}{\Gamma(m)} F_{\gamma_{FSO}}(\gamma_{T1}) - \left\{ \frac{\xi^2 e^{\frac{-mx}{\bar{\gamma}_{RF}}}(m-1)!}{\Gamma(\alpha)\Gamma(\beta)\Gamma(m)} \sum_{n=0}^{\infty} \frac{(m\gamma_{T2}/\bar{\gamma}_{RF})^n}{n!} \sum_{k=0}^{m-1} \right. \\ &\left. \frac{(mx/\bar{\gamma}_{RF})^k}{k!} \sum_{j=0}^{k} \binom{k}{j} \times \left(\frac{-\gamma_{T1}}{x}\right)^j G_{2,4}^{3,1}\left[\frac{\xi^2 \alpha\beta\gamma_{T1}}{(\xi^2+1)\bar{\gamma}_{FSO}} \,\middle|^{1-n-j,\xi^2+1}_{\xi^2,\alpha,\beta,-n-j} \right] \right\}.\end{aligned} \tag{3.18}$$

Finally, the CDF of γ_c is obtained after substituting (3.15) and (3.18) into (3.10).

3.2.1 Average Spectral Efficiency

The average spectral efficiency of the proposed adaptive hybrid FSO/RF system, defined as the average number of bits transmitted over each symbol period [32], is given by:

$$\eta^{Adapt} = \sum_{n=1}^{N} 2n[F_{\gamma_c}(\gamma_{Tn+1}) - F_{\gamma_c}(\gamma_{Tn})]. \tag{3.19}$$

3.2.2 Outage Probability

When $\gamma_{FSO} < \gamma_{T1}$, and γ_c also falls below γ_{T1}, the communication system goes into outage state, in which the received SNR can't support the target BER of the system and data transmission is suspended over both links. The outage probability of the adaptive hybrid FSO/RF system can be simply calculated by evaluating the CDF of γ_c at γ_{T1} as:

$$\mathrm{P}_{out}^{Adapt} = F_{\gamma_c}(\gamma_{T1}) = F_1(\gamma_{T1}). \tag{3.20}$$

3.2.3 Average Bit-Error Rate

The average BER of the proposed adaptive hybrid FSO/RF system, defined as the ratio of the average number of erroneously received bits over the total average number of transmitted bits [32], is given by:

$$< BER >= \frac{1}{\eta^{Adapt}} \sum_{n=1}^{N} 2n\overline{BER}_n, \tag{3.21}$$

where $\overline{BER}_n$ is the average error rate of using constellation of size 2^{2n}, given by:

$$\overline{BER}_n = G_1 + G_2, \tag{3.22}$$

with G_1 corresponds to the FSO-only mode and is defined as:

$$G_1 = \int_{\gamma_{T\,n}}^{\gamma_{T\,n+1}} BER_n(\gamma_{FSO}) f_{\gamma_{FSO}}(\gamma_{FSO}) d\gamma_{FSO}, \tag{3.23}$$

and G_2 represents the combind FSO/RF mode and is defined as:

$$G_2 = \int_{\gamma_{T\,n}}^{\gamma_{T\,n+1}} \int_{0}^{\gamma_{T\,1}} BER_n(\gamma_c) f_{\gamma_{FSO}}(\gamma_{FSO}) f_{\gamma_{RF}}(\gamma_c - \gamma_{FSO}) d\gamma_{FSO} d\gamma_c. \tag{3.24}$$

G_1 and G_2 can be evaluated using numerical methods with $BER_n(\cdot)$, $f_{\gamma_{FSO}}(\cdot)$, and $f_{\gamma_{RF}}(\cdot)$ are given respectivelly by (3.2), (3.4), and (3.8).

3.3 Performance Analysis of Switch-Over Scheme with Adaptive Modulation

For comparison purposes, we introduce here the performance metrics of switch-over hybrid FSO/RF system [30]. To have fair comparison, we assume using the same adaptive modulation scheme that was used with our proposed system.

3.3.1 Average Spectral Efficiency

The average spectral efficiency of the switch-over hybrid FSO/RF system in this case is given by:

$$\eta^{Switch} = \sum_{n=1}^{N} 2n \Big\{ \left[F_{\gamma_{FSO}}(\gamma_{T\,n+1}) - F_{\gamma_{FSO}}(\gamma_{T\,n})\right] + F_{\gamma_{FSO}}(\gamma_{T\,1}) \times \left[F_{\gamma_{RF}}(\gamma_{T\,n+1}) - F_{\gamma_{RF}}(\gamma_{T\,n})\right] \Big\}. \tag{3.25}$$

3.3.2 Outage Probability

When $\gamma_{FSO} < \gamma_{T1}$, and γ_{RF} also falls below γ_{T1}, the communication system goes into outage. In this case, the outage probability of the hybrid system can be evaluated as:

$$\mathrm{P}_{out}^{Switch} = F_{\gamma_{FSO}}(\gamma_{T1})F_{\gamma_{RF}}(\gamma_{T1}). \tag{3.26}$$

3.4 Numerical Results

In this section we present several numerical examples to illustrate the math formulation and to study the proposed system's performance. We will consider three different 2^{2n}-QAM modulation schemes with $n = 1, 2$, and 3, where the corresponding thresholds γ_{T_n}, assuming $\mathrm{BER}_0 = 10^{-6}$ can be calculated using (3.1). The relevant parameters of the FSO and RF subsystems considered for the numerical results are given in Table 3.1. The strongest atmospheric turbulence commonly occurs when weather is clear and becomes weaker as the weather condition gets worse by means of either fog or rain. We consider in our numerical examples the scenario of clear weather condition and strong atmospheric turbulence ($C_n^2 = 2 \times 10^{-13}$), with weather-dependent attenuation coefficient α_{FSO}= 0.44 dB/km and RF rain attenuation $\alpha_{rain} = 0$ dB/km, along with pointing error effects [17]. We assume RF channel fading severity of $m = 5$ in all Figures.

In Fig. 3.2, we plot the average spectral efficiency of the proposed adaptive hybrid FSO/RF system as a function of the transmitted power of the FSO link P_{FSO}. It can be seen from Fig. 3.2, that average spectral efficiency increases as the FSO link's quality improves by increasing P_{FSO}. Also, we can observe that with sufficient high P_{FSO}, the average spectral efficiency of the adaptive hybrid system is the same as that of FSO-only system and switch-over hybrid system which in this case relies on FSO link. This is because the FSO link's quality is good to support the target BER alone without the need of activating the RF link. On the other hand, as the FSO link's quality degrades due to strong atmospheric turbulence in clear weather conditions, the RF link is activated along with the FSO link which leads to a significant improvement in the average spectral efficiency of the adaptive hybrid system over both switch-over hybrid FSO/RF and FSO-only systems, as can be seen from Fig. 3.2. The numerical results shown in Fig. 3.2 for the average spectral efficiency of the proposed adaptive hybrid FSO/RF system are obtained using n=30 and k=30 in (3.15) and n=30 in

Table 3.1: Parameters of FSO and RF subsystems

Parameter	Symbol	Value
FSO Subsystem		
Wavelength	λ_{FSO}	1550 nm
Transmission Rate	$1/T$	1 Gbit/s
Responsivity	η	0.75 A/W
Photodetector Diameter	D	20 cm
Transmit divergence at $1/e^2$	θ_0	2.5 mrad
Jitter standard deviation	σ_s	30 cm
Link distance	z	1000 m
RF Subsystem		
Carrier Frequency	f_{RF}	60 GHz
Bandwidth	W	250 MHz
Transmit Power	P_{RF}	-10 dBm
Transmit Antenna Gain	G_T	44 dBi
Recieve Antenna Gain	G_R	44 dBi
Noise Power Spectral Density	N_0	-114 dBm/MHz
Receiver Noise Figure	N_F	5 dB
Oxgyen Attenuation	α_{oxy}	15.1 dB/Km

(3.18), which are then plugged in (3.10) to be used in evaluating (3.19). As can be observed, evaluating the average spectral efficiency using the truncated values of (3.15) and (3.18) gives accurate results that coincide with the values that are obtained by evaluating the integrals in (3.11) and (3.12) using numerical methods before plugged in (3.10) to evaluate (3.19).

In Fig. 3.3, we plot the outage probability of the proposed adaptive hybrid system as a function of P_{FSO}. It can be seen that the proposed adaptive hybrid system gives an outage performance much better than that of switch-over hybrid system or FSO-only system with the same adaptive modulation scheme. In Fig. 3.4, we plot the average BER of the proposed adaptive hybrid system as a function of P_{FSO}. It can be shown that, the proposed adaptive hybrid system can achieve an average BER which is less than the target instantaneous BER (10^{-6} in our numerical examples). As expected, the average BER is improved as the optical link's quality increases.

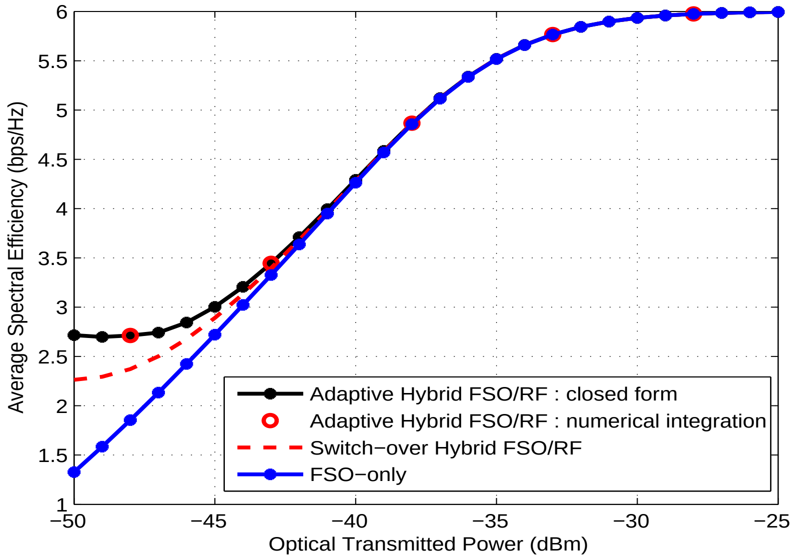

Figure 3.2: Average spectral efficiency of the proposed hybrid FSO/RF system as a function of the transmitted power of the FSO link.

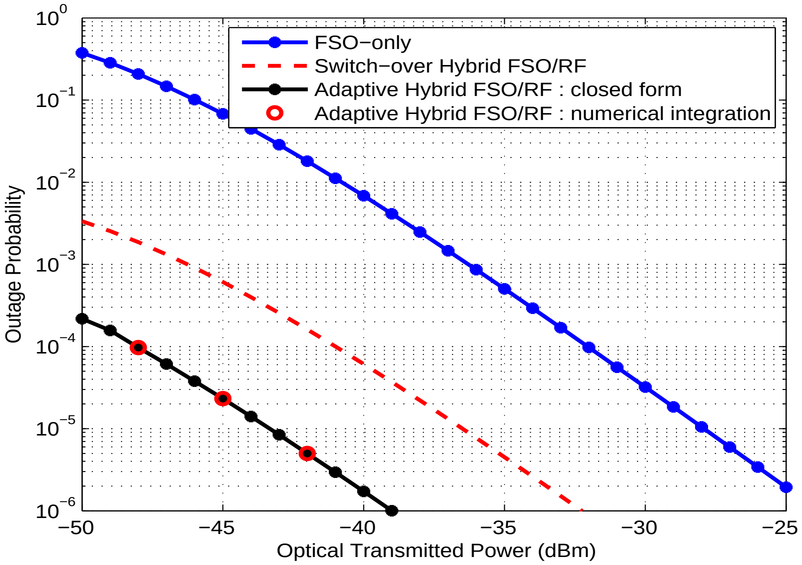

Figure 3.3: Outage probability of the proposed hybrid FSO/RF system as a function of the transmitted power of the FSO link.

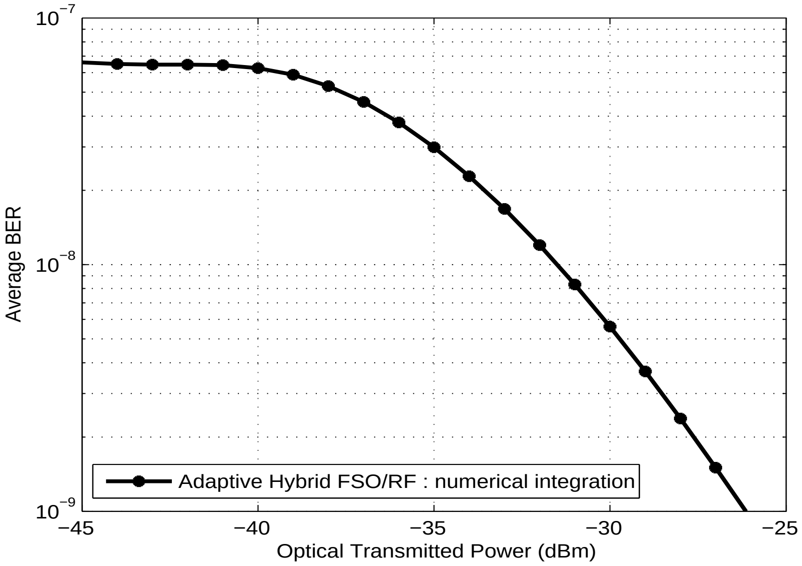

Figure 3.4: Average BER of the proposed hybrid FSO/RF system as a function of the transmitted power of the FSO link.

It is worth to mention that similar superior performance of the proposed adaptive hybrid FSO/RF system over both FSO-only and switch-over hybrid FSO/RF systems is expected in other weather conditions, mainly in fog and rain. In rain conditions, FSO link is not affected and thus the communication system can relay on it without needing to activate the RF link. On the other hand, FSO link is affected by fog which will degrade its performance, thus activating the RF link which is not affected by fog, along with the FSO link, will support the FSO link and maintain a reliable communication channel.

3.5 Summery

In this chapter, we presented a new hybrid FSO/RF system based on joint adaptive modulation and adaptive combining scheme. We offered a novel closed-form of the exact CDF of the received SNR for the proposed adaptive hybrid FSO/RF system. The performance metrics of the proposed adaptive hybrid system, mainly average spectral efficiency, outage probability, and average BER are studied. Numerical results showed that the proposed adaptive hybrid FSO/RF system has superior spectral efficiency and outage performance compared to that of switch-over hybrid FSO/RF and FSO-only systems, while maintaining good average BER.

Chapter 4

Power Adaptation Based on Truncated Channel Inversion for Hybrid FSO/RF Transmission with Adaptive Combining

In this chapter, we consider power adaptation strategies based on truncated channel inversion for hybrid FSO/RF system employing adaptive combining. Specifically, we adaptively set the RF link transmission power when FSO link quality is unacceptable to ensure constant combined SNR at receiver. Two adaptation strategies are proposed. One strategy depends on the received RF SNR, while the other one depends on the combined SNR of both links. We study the outage probability of the hybrid FSO/RF system with and without power adaptation.

The remainder of the chapter is organized as follows. In section 4.1, we introduce the system and channel models. In section 4.2, we introduce the power allocation strategies, and the outage analysis of the proposed system namely, the outage probability and the outage capacity. Finally, section 4.3 presents some numerical examples to investigate the performance of the hybrid system with and without power adaptation. Further power adaptation for FSO link is introduced in section 4.4, followed by the conclusion in section 4.5.

4.1 System and Channel Modeling

We consider a hybrid FSO/RF system, where the FSO link is active all the time with constant transmitted power. To maintain a target data rate, the received SNR should not be less than a predetermined target value denoted by γ_T. When the instantaneous SNR at the receiver of the FSO link denoted by γ_{FSO}, falls below the threshold γ_T, FSO link alone can't support the high data rate transmission. In this case, the receiver sends a feedback signal on the FSO link to activate the RF link along with the FSO link to help maintain the link reliability. When the RF link is activated, simultaneous transmission of the same data on both links takes place. At the receiver, the data received over both links will be combined using an MRC combiner. It is important to clarify that in case of using both FSO and RF links, the data rate of FSO link may be reduced to be the same as that of the RF link to facilitate diversity reception. The receiver SNR, denoted by γ_c, will be equal to γ_{FSO} when $\gamma_{FSO} \geq \gamma_T$. When $\gamma_{FSO} < \gamma_T$, γ_c will be equal to the sum of γ_{FSO} and γ_{RF} where γ_{RF} is the receiver SNR of the RF link. In this case, the transmitted power over the RF link is adapted to maintain the constant received SNR γ_T, i.e., to keep $\gamma_{FSO} + \gamma_{RF} = \gamma_T$. We will discuss the power adaptation policy in the following section.

4.1.1 Modeling the FSO Link

We assume that the FSO link experiences Gamma-Gamma fading due to atmospheric turbulence, and atmospheric loss along with pointing error impairments, for which the PDF of the received irradiance I is given by [65, Eq. (11)] (or equivalently using [53, Eq. (9.31.5)]):

$$f_I(I) = \frac{\xi^2 I^{-1}}{\Gamma(\alpha)\Gamma(\beta)} G_{1,3}^{3,0}\left[\frac{\alpha\beta I}{A_0 G_{FSO}} \;\middle|\; {}^{\xi^2+1}_{\xi^2,\ \alpha,\ \beta}\right], \qquad I \geq 0, \tag{4.1}$$

where ξ is the ratio between the equivalent beam radius at the FSO receiver aperture and the pointing error (jitter) standard deviation at the FSO receiver, A_0 is a constant term that defines the pointing error loss [17], $\Gamma(.)$ is the standard Gamma function, and α and β are the effective number of small-scale and large-scale eddies of the turbulent environment, respectively. Different values of α and β corresponds to different turbulence regimes. Expressions for calculating the parameters α and β for different propagation conditions can be found in [54]. In Eq. (4.1), $G[.]$ is the Meijer G-function as defined in [53, Eq. (9.301)], and G_{FSO} is the optical power attenuation, given by Beers-Lambert law as $G_{FSO} = \alpha_{FSO} z$ [26], with α_{FSO} being the weather-dependent attenuation coefficient (in dB/Km) and z is the link range from the transmitter to the receiver. The attenuation G_{FSO} is considered as a fixed scaling factor, and no randomness exists in its behavior [17].

Considering sub-carrier modulated FSO communication system, in which an electrical sub-carrier signal is pre-modulated[1] with the information bits before being used to modulate the optical signal for transmission, there are two techniques for FSO signal detection at the receiver side, which are Intensity Modulation/Direct Detection (IM/DD) [12] and Coherent Modulation/Heterodyne Detection (CM/HD) [13]. A unified expression for the PDF of γ_{FSO}, considering the two types of FSO detection, is given in a general form as [66]:

$$f_{\gamma_{FSO}}(\gamma_{FSO}) = \frac{\xi^2 {\gamma_{FSO}}^{-1}}{r\Gamma(\alpha)\Gamma(\beta)} G_{1,3}^{3,0}\left[\frac{\xi^2\alpha\beta}{(\xi^2+1)}\left(\frac{\gamma_{FSO}}{\bar{\gamma}_{FSO_r}}\right)^{\frac{1}{r}} \Big|_{\xi^2,\alpha,\beta}^{\xi^2+1}\right], \qquad \gamma_{FSO} \geq 0, \tag{4.2}$$

where r is the parameter defining the type of FSO detection technique (i.e., r=1 represents CM/HD technique and r=2 represents IM/DD technique) and $\bar{\gamma}_{FSO_r}$[2] is the average SNR of FSO link.

By using [56, Eq. (07.34.21.0084.01)] and some simple algebraic manipulations, the CDF of γ_{FSO} can be expressed as:

$$F_{\gamma_{FSO}}(\gamma_{FSO}) = \frac{\xi^2 r^{\alpha+\beta-2}}{(2\pi)^{r-1}\Gamma(\alpha)\Gamma(\beta)} G_{r+1,3r+1}^{3r,1}\left[\frac{B\gamma_{FSO}}{\bar{\gamma}_{FSO_r}} \Big|_{K_2,0}^{1,K_1}\right], \qquad \gamma_{FSO} \geq 0, \tag{4.3}$$

where $B = \left(\frac{\xi^2\alpha\beta}{(\xi^2+1)r^2}\right)^r$, $K_1 = \frac{\xi^2+1}{r}, ..., \frac{\xi^2+r}{r}$ has r terms, and $K_2 = \frac{\xi^2}{r}, ..., \frac{\xi^2+r-1}{r}, \frac{\alpha}{r}, ..., \frac{\alpha+r-1}{r}, \frac{\beta}{r}, ..., \frac{\beta+r-1}{r}$ has $3r$ terms.

4.1.2 Modeling the RF Link

At the RF transmitter, the digitally modulated electrical signal, which is the same as the one in FSO subsystem, is up-converted using 60 GHz RF carrier. The up-converted RF signal is transmitted and received using L branches RF transmis-

---

[1] For example, by using M-QAM digital modulation scheme, which is widely used in high-rate data transmissions over FSO links [61], and RF links [62], because of its high spectral efficiency and ease of signal modulation/demodulation process.

[2] For CM/HD, $\bar{\gamma}_{FSO_1} = \eta_e E[I]/N_0$ [66], with η_e is the effective photoelectric conversion ratio, N_0 symbolizes the AWGN sample, and $E[I]$ is the expectation of I, which by using [55, Eq. (24)] is given by $E[I] = \xi^2 A_0 G_{FSO}/(\xi^2+1)$. For IM/DD, $\bar{\gamma}_{FSO_2} = (\eta_e E[I])^2/N_0$ [66].

sion/reception scheme. The received SNR from each RF branch, denoted by $\gamma_{i_{RF}}$, follows independent and identical distribution (i.i.d) Nakagami-m fading distribution with PDF given by [67]:

$$f_{\gamma_{i_{RF}}}(\gamma_{RF}) = \left(\frac{m}{\bar{\gamma}_{RF}}\right)^{m} \frac{{\gamma_{RF}}^{m-1}}{\Gamma(m)} \exp\left(\frac{-m\gamma_{RF}}{\bar{\gamma}_{RF}}\right), \qquad \gamma_{RF} \geq 0, \tag{4.4}$$

where $\bar{\gamma}_{RF}$ is the average SNR of the ith channel with $1 \leq i \leq L$, and m is a parameter indicating fading severity. $\bar{\gamma}_{RF}$ and m are assumed to be common on all the L diversity branches. The overall received SNR of the RF link γ_{RF} will be that after the MRC combination of all the L RF channels, such that $\gamma_{RF} = \sum_{i=1}^{L} \gamma_{i_{RF}}$, the PDF of which is given by: [67]

$$f_{\gamma_{RF}}(\gamma_{RF}) = \left(\frac{m}{\bar{\gamma}_{RF}}\right)^{mL} \frac{{\gamma_{RF}}^{mL-1}}{\Gamma(mL)} \exp\left(\frac{-m\gamma_{RF}}{\bar{\gamma}_{RF}}\right), \qquad \gamma_{RF} \geq 0. \tag{4.5}$$

By using [53, Eq. (3.351.1)], and some simple algebraic manipulations, the CDF of γ_{RF} can be expressed as:

$$F_{\gamma_{RF}}(\gamma_{RF}) = \frac{1}{\Gamma(mL)} \gamma\left(mL, \frac{m\gamma_{RF}}{\bar{\gamma}_{RF}}\right), \qquad \gamma_{RF} \geq 0, \tag{4.6}$$

where $\gamma(\cdot,\cdot)$ is the lower incomplete Gamma function defined in [53, Eq. (8.350.1)].

4.2 Power Allocation Strategies and Outage Analysis

We assume constant FSO transmitting power all the time. When $\gamma_{FSO} < \gamma_T$, the RF link is activated along with the FSO link and the RF link transmitted power P_{RF} is adapted to maintain the required constant received SNR γ_T. We introduce here two different policies for RF link power adaptation. Both of them are based on the TCI principle [32].

4.2.1 TCI For RF Link Based on γ_{RF}

Power Adaptation Policy

In this power adaptation policy, the transmitter uses the CSI (specifically, γ_{FSO} and γ_{RF}) to maintain the target received SNR γ_T. Since the power adaptation is performed after activating the RF link, the RF link SNR is adaptively changed to fill the gap between γ_{FSO} and γ_T such that $\gamma_{RF} + \gamma_{FSO}{=}\gamma_T$. The RF power is adapted as long as the received RF SNR is above a certain threshold denoted by γ_{0_I}. Otherwise, data transmission is suspended. We will refer to this policy as γ_{RF}-based TCI which is mathematically given by:

$$\frac{P_{RF}(\gamma_{RF},\gamma_{FSO})}{\bar{P}_{RF}} = \begin{cases} \frac{\gamma_T - \gamma_{FSO}}{\gamma_{RF}}, & \text{if } \gamma_{RF} \geq \gamma_{0_I} \\ 0, & \text{if } \gamma_{RF} < \gamma_{0_I}, \end{cases} \tag{4.7}$$

where γ_{0_I} satisfies the average power constraint of RF link transmitter given by:

$$\int_{0}^{\gamma_T}\int_{\gamma_{0_I}}^{\infty} \frac{P_{RF}(\gamma_{RF},\gamma_{FSO})}{\bar{P}_{RF}} f_{\gamma_{RF}}(\gamma_{RF}) f_{\gamma_{FSO}}(\gamma_{FSO}) d\gamma_{RF} d\gamma_{FSO} = 1, \tag{4.8}$$

where $\bar{P}_{RF}$ is the average transmitted power over the RF link.

By substituting (4.2) and (4.5) in (4.8), and using [53, Eq. (3.381.9)] and [56, Eq. (07.34.21.0084.01)], the constraint in (4.8) can be expressed as:

$$A_1\Gamma\left(mL-1, \frac{m\gamma_{0_I}}{\bar{\gamma}_{RF}}\right)\left\{ G^{3r,1}_{r+1,3r+1}\left[\frac{B\gamma_T}{\bar{\gamma}_{FSO_r}}\ \Big|^{1,K_1}_{K_2,0}\right] - G^{3r,1}_{r+1,3r+1}\left[\frac{B\gamma_T}{\bar{\gamma}_{FSO_r}}\ \Big|^{0,K_1}_{K_2,-1}\right] \right\} = 1, \tag{4.9}$$

where $A_1 = \xi^2 r^{\alpha+\beta-2} m\gamma_T/(2\pi)^{r-1}\bar{\gamma}_{RF}\Gamma(\alpha)\Gamma(\beta)\Gamma(mL)$, and $\Gamma(\cdot,\cdot)$ is the upper incomplete Gamma function defined in [53, Eq. (8.350.2)]. As with most TCI schemes, the value for γ_{0_I} that satisfies (4.9) can be found using numerical methods, such as bisection method and Newton method [68].

Outage Probability For γ_{RF}-based TCI

According to this policy, the hybrid system goes into outage state if the RF link received SNR γ_{RF} goes below γ_{0_I}. The probability of outage in this case can be calculated as:

$$\begin{aligned} \mathrm{P}_{out} &= \mathrm{P_r}[\gamma_{FSO} < \gamma_T]\mathrm{P_r}[\gamma_{RF} < \gamma_{0_I}]. \\ &= F_{\gamma_{FSO}}(\gamma_T)F_{\gamma_{RF}}(\gamma_{0_I}), \end{aligned} \tag{4.10}$$

where $F_{\gamma_{FSO}}(.)$ and $F_{\gamma_{RF}}(.)$ are given by (4.3) and (4.6), respectively.

4.2.2 TCI For RF Link Based on $\gamma_{RF} + \gamma_{FSO}$

Power Adaptation Policy

This RF link power adaptation policy is similar to the first one. However, the RF power is adapted as long as the overall SNR after MRC combination of the RF link and the FSO link (i.e., $\gamma_{RF} + \gamma_{FSO}$) is above a certain threshold denoted by $\gamma_{0_{II}}$. Otherwise, data transmission is suspended. We will refer to this policy as $\gamma_{RF} + \gamma_{FSO}$-based TCI which is given by:

$$\frac{P_{RF}(\gamma_{RF}, \gamma_{FSO})}{\bar{P}_{RF}} = \begin{cases} \frac{\gamma_T - \gamma_{FSO}}{\gamma_{RF}}, & \text{if } \gamma_{RF} + \gamma_{FSO} \geq \gamma_{0_{II}} \\ 0, & \text{if } \gamma_{RF} + \gamma_{FSO} < \gamma_{0_{II}}, \end{cases} \tag{4.11}$$

where $\gamma_{0_{II}}$ satisfies the average power constraint over the RF link given by:

$$\int_{0}^{\gamma_T} \int_{\gamma_{0_{II}} - \gamma_{FSO}}^{\infty} \frac{P_{RF}(\gamma_{RF}, \gamma_{FSO})}{\bar{P}_{RF}} f_{\gamma_{RF}}(\gamma_{RF}) f_{\gamma_{FSO}}(\gamma_{FSO}) d\gamma_{RF} d\gamma_{FSO} = 1. \tag{4.12}$$

By substituting (4.2) and (4.5) in (4.12), and using the binomial expansion defined in [53, Eq. (1.111)] and the series expansion of the exponential defined in [53, Eq. (1.211.1)], along with [53, Eq. (3.351.2)] and [56, Eq. (07.34.21.0084.01)], the constraint in (4.12) can be expressed as:

$$\begin{aligned} &A_2 e^{\frac{-m\gamma_{0_{II}}}{\bar{\gamma}_{RF}}} \sum_{n=0}^{\infty} \frac{(m\gamma_T/\bar{\gamma}_{RF})^n}{n!} \sum_{i=0}^{mL-2} \frac{(m\gamma_{0_{II}}/\bar{\gamma}_{RF})^i}{i!} \sum_{k=0}^{i} \binom{i}{k} \left(\frac{-\gamma_T}{\gamma_{0_{II}}}\right)^k \Bigg\{ \\ &G^{3r,1}_{r+1,3r+1}\left[\frac{B\gamma_T}{\bar{\gamma}_{FSO_r}} \,\Big|^{1-n-k,K_1}_{K_2,-n-k}\right] - G^{3r,1}_{r+1,3r+1}\left[\frac{B\gamma_T}{\bar{\gamma}_{FSO_r}} \,\Big|^{-n-k,K_1}_{K_2,-n-k-1}\right]\Bigg\} = 1, \end{aligned} \tag{4.13}$$

where $A_2 = \xi^2 r^{\alpha+\beta-2} m(mL-2)!\gamma_T/(2\pi)^{r-1}\Gamma(\alpha)\Gamma(\beta)\Gamma(mL)\bar{\gamma}_{RF}$. Similar to γ_{0_I}, the value for $\gamma_{0_{II}}$ that satisfies (4.13) can be found using numerical methods. When using (4.13) to search for the value of $\gamma_{0_{II}}$, it is sufficient to use $n = 40$ to obtain stable values with accuracy to the fourth digit. This can be observed from Table 4.1 and Table 4.2, where we consider γ_T=10 dB, typical values of α and β for weak atmospheric turbulence regime (α=2.902, and β=2.51) [60], $\bar{\gamma}_{FSO_r}$=0 dB, $\xi = 1$, Nakagami parameter m=2, and L=1 to obtain the values of $\gamma_{0_{II}}$ for different values of $\bar{\gamma}_{RF}$.

Table 4.1: Values of $\gamma_{0_{II}}$ considering CM/HD (r=1) with different values of n

$\bar{\gamma}_{RF}$ (dB)	$n = 30$	$n = 35$	$n = 40$	$n = 45$
0	6.2125	6.2142	6.2142	6.2142
1	5.5250	5.5250	5.5251	5.5251
8	4.3291	4.3291	4.3291	4.3291
12	1.9091	1.9091	1.9091	1.9091

Table 4.2: Values of $\gamma_{0_{II}}$ considering IM/DD (r=2) with different values of n

$\bar{\gamma}_{RF}$ (dB)	$n = 30$	$n = 35$	$n = 40$	$n = 45$
0	7.2243	7.2264	7.2265	7.2265
4	4.9315	4.9315	4.9315	4.9315
10	3.5144	3.5144	3.5144	3.5144
12	1.2882	1.2882	1.2882	1.2882

Outage Probability for $\gamma_{RF} + \gamma_{FSO}$-based TCI

According to this policy, the hybrid system goes into outage state if MRC combination of the FSO and RF links failed to support a received SNR of $\gamma_{RF} + \gamma_{FSO} \geq \gamma_{0_{II}}$. The probability of outage in this case can be calculated as:

$$\begin{aligned}
\mathrm{P}_{out} &= \mathrm{P_r}[\gamma_{FSO} < \gamma_T, \gamma_{FSO} + \gamma_{RF} < \gamma_{0_{II}}]. \\
&= \int\limits_{0}^{\gamma_{0_{II}}} \int\limits_{0}^{min[\gamma_T, \gamma_{0_{II}} - \gamma_{RF}]} f_{\gamma_{FSO}}(\gamma_{FSO}) f_{\gamma_{RF}}(\gamma_{RF}) d\gamma_{FSO} d\gamma_{RF} \\
&= \int\limits_{0}^{\gamma_{0_{II}} - \gamma_T} \int\limits_{0}^{\gamma_T} f_{\gamma_{FSO}}(\gamma_{FSO}) f_{\gamma_{RF}}(\gamma_{RF}) d\gamma_{FSO} d\gamma_{RF} \qquad (4.14) \\
&\quad + \int\limits_{\gamma_{0_{II}} - \gamma_T}^{\gamma_{0_{II}}} \int\limits_{0}^{\gamma_{0_{II}} - \gamma_{RF}} f_{\gamma_{FSO}}(\gamma_{FSO}) f_{\gamma_{RF}}(\gamma_{RF}) d\gamma_{FSO} d\gamma_{RF}.
\end{aligned}$$

If $\gamma_T > \gamma_{0_{II}}$, which is the case most of the time, then (4.14) will be given by:

$$\begin{aligned}
\mathrm{P}_{out} &= \int\limits_{0}^{\gamma_{0_{II}}} \int\limits_{0}^{\gamma_{0II} - \gamma_{RF}} f_{\gamma_{FSO}}(\gamma_{FSO}) f_{\gamma_{RF}}(\gamma_{RF}) d\gamma_{FSO} d\gamma_{RF}. \\
&= \int\limits_{0}^{\gamma_{0_{II}}} f_{\gamma_{RF}}(\gamma_{RF}) F_{\gamma_{FSO}}(\gamma_{0_{II}} - \gamma_{RF}) d\gamma_{RF}.
\end{aligned} \qquad (4.15)$$

By substituting (4.3) and (4.5) in (4.15), making change of variable, and using the series expansion of the exponential, along with [56, Eq. (07.34.21.0084.01)], (4.15) can be evaluated as:

$$\mathrm{P}_{out} = \frac{\xi^2 r^{\alpha+\beta-2} e^{\frac{-m\gamma_{0_{II}}}{\bar{\gamma}_{RF}}} \left(\frac{m\gamma_{0_{II}}}{\bar{\gamma}_{RF}}\right)^{mL}}{(2\pi)^{r-1}\Gamma(\alpha)\Gamma(\beta)} \sum_{n=0}^{\infty} \left\{ \frac{\left(\frac{m\gamma_{0_{II}}}{\bar{\gamma}_{RF}}\right)^{n}}{n!} G_{r+2,3r+2}^{3r,2} \left[\frac{B\gamma_{0_{II}}}{\bar{\gamma}_{FSO_r}} \,\middle|_{K_2,0,-n-mL}^{-n,1,K_1} \right] \right\}. \qquad (4.16)$$

4.2.3 Outage Capacity

Practically speaking, outage capacity applies to slowly-varying channels [32], which is the case with FSO and MMW RF channels with bit-duration much smaller than the channels coherence time [17,28]. The outage capacity is defined as the maximum data rate that can be maintained in all non-outage channel states times the probability of non-outage. The outage capacity associated with a given outage probability P_{out} normalized to the communication channel bandwidth B can be expressed as [69]:

$$\frac{C(\mathrm{P}_{out})}{B} = [1 - \mathrm{P}_{out}] \log_2(1 + K\gamma_T), \tag{4.17}$$

where K is a constant term such that $K = 1$ for heterodyne detection giving an exact result and $K = e/(2\pi)$ for IM/DD giving a lower-bound result. The outage probability P_{out} in (4.17) is given by either (4.10) or (4.16) according to the power adaptation policy used on the RF link.

4.3 Hybrid FSO/RF System with Adaptive Combining Only

In this section, we analyze the outage probability of the hybrid FSO/RF system without power adaptation. We assume that the outage threshold denoted by γ_{out} is smaller than the switching threshold γ_T. Otherwise, the hybrid system will enter outage before activating RF link. When the FSO link SNR γ_{FSO} falls below γ_T, and the instantaneous receiver SNR $\gamma_c = \gamma_{FSO} + \gamma_{RF}$ falls below the outage threshold γ_{out}, the communication link can not support a target BER and goes into outage state. In this case, the outage probability of the hybrid FSO/RF system without power adaptation can be calculated as:

:

$$\begin{aligned} \mathrm{P}_{out} &= \mathrm{P_r}[\gamma_{FSO} < \gamma_T, \gamma_{FSO} + \gamma_{RF} < \gamma_{out}]. \\ &= \int_0^{\gamma_{out}} f_{\gamma_{FSO}+\gamma_{RF}}(y)dy. \end{aligned} \tag{4.18}$$

Noting that the FSO and RF links are statistically independent, $f_{\gamma_{FSO}+\gamma_{RF}}(y)$ in (4.18) can be evaluated as:

$$f_{\gamma_{FSO}+\gamma_{RF}}(y) = \int_0^{y} f_{\gamma_{FSO}}(\gamma_{FSO}) f_{\gamma_{RF}}(y - \gamma_{FSO}) d\gamma_{FSO}, \tag{4.19}$$

where $f_{\gamma_{FSO}}(.)$ and $f_{\gamma_{RF}}(.)$ are given by (4.2) and (4.5), respectively. Finally,

$$\mathrm{P}_{out} = \int_{0}^{\gamma_{out}} \int_{0}^{y} f_{\gamma_{FSO}}(\gamma_{FSO}) f_{\gamma_{RF}}(y-\gamma_{FSO}) d\gamma_{FSO} dy, \tag{4.20}$$

which can be numerically evaluated.

4.4 Numerical results

In this section we present several numerical examples to investigate the performance of the two proposed power adaptation strategies. Note that in all numerical results, we assume using optical wavelength $\lambda_{FSO} = 1550$ nm [70]. Also, note that for the numerical results shown in Figs. 4.2, 4.4, and 4.5 we assume no RF diversity, i.e., $L = 1$.

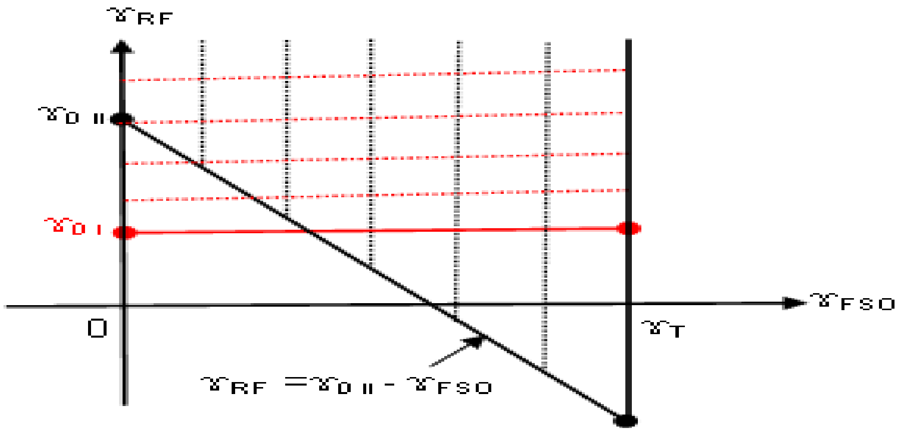

Figure 4.1: Integration regions of Eqs. (4.8) and (4.12).

In Fig. 4.2, we plot the outage probability of the hybrid system with and without power adaptation as a function of the average RF link SNR $\bar{\gamma}_{RF}$. We assume weak atmospheric turbulence (α=2.902, and β=2.51) affecting the FSO link with pointing error effect of $\xi = 1$, and RF link fading severity of $m = 2$. It can be seen from Fig. 4.2 that considering either CM/HD technique (Fig. 4.2a) or IM/DD technique (Fig. 4.2b), using the $\gamma_{RF}-$based TCI adaptation policy gives better outage performance than using the $\gamma_{RF}+\gamma_{FSO}-$based TCI adaptation policy. This is because that under the same conditions of the FSO and RF links, γ_{0_I} is less than $\gamma_{0_{II}}$. To explain this, let $f(\gamma_{RF},\gamma_{FSO}) = \frac{P_{RF}(\gamma_{RF},\gamma_{FSO})}{\bar{P}_{RF}} f_{\gamma_{RF}}(\gamma_{RF}) f_{\gamma_{FSO}}(\gamma_{FSO})$. We need the integration of

$f(\gamma_{RF}, \gamma_{FSO})$ over the red shaded area in Fig. 4.1 to be equal to 1, according to (4.8), and also we need the integration of $f(\gamma_{RF}, \gamma_{FSO})$ over the black shaded area in Fig. 4.1 to be equal to 1, according to (4.12). If we assume that γ_{0_I} is greater than or equal to $\gamma_{0_{II}}$, then the integration of $f(\gamma_{RF}, \gamma_{FSO})$ over the red shaded area will be greater than 1 which is impossible according to the constraint in (4.8). Thus, γ_{0_I} is less than $\gamma_{0_{II}}$. The analytical results for the outage probability of the hybrid system with $\gamma_{RF}+\gamma_{FSO}-$based TCI adaptation policy shown in Fig. 4.2 are obtained using n=30 in (4.16). As can be observed, evaluating the outage probability with the truncated values of n=30 gives accurate results as compared with the values obtained by evaluating the integral in (4.15) using numerical methods. It can also be seen from Fig. 4.2, that applying power adaptation (either γ_{RF}-based TCI or $\gamma_{RF}+\gamma_{FSO}$-based TCI) policy greatly improves the outage performance of the hybrid system over the case without using power adaptation. Note that we had used numerical integration to evaluate the outage probability for the hybrid system without power adaptation, given in (4.20), with outage threshold γ_{out}=9.5 dB. Note also that the value γ_{out}=9.5 dB is less than γ_T=10 dB so that the hybrid system switches to the MRC combination of the FSO and RF links before the FSO link alone goes in outage.

In Fig. 4.3, we examine the effect of the RF link diversity on the outage performance of the hybrid FSO/RF system with both power adaptation policies (Fig. 4.3a and Fig. 4.3b). It can be seen from Fig. 4.3, that as the number of the RF branches increases, the outage performance of the hybrid system greatly improves. Intuitively, the same observation shown in Fig. 4.3 is also applicable when using CM/HD technique.

In Fig. 4.4, we examine the outage performance of the proposed hybrid FSO/RF system in the presence of strong atmospheric turbulence (α=2.064, and β=1.342) affecting the FSO link with less sever pointing error effect of $\xi = 4$, and RF link fading severity of $m = 2$. It can be seen from Fig. 4.4, that the hybrid FSO/RF system employing either of the two proposed power adaptation polices achieves superior outage performance compared to the performance of the system without power adaptation in this case also.

In Fig. 4.5, we plot the outage capacity of the hybrid system with power adaptation as a function of the average RF link SNR $\bar{\gamma}_{RF}$. We assume weak atmospheric turbulence (α=2.902, and β=2.51) affecting the FSO link with pointing error effect of $\xi = 1$, and RF link fading severity of $m = 2$. It can be seen from Fig. 4.5 that considering either CM/HD technique (Fig. 4.5a) or IM/DD technique (Fig. 4.5b), using $\gamma_{RF}-$based TCI adaptation policy leads to higher outage capacity than using $\gamma_{RF}+\gamma_{FSO}-$based TCI adaptation policy. This is because using $\gamma_{RF}-$based TCI adaptation policy achieves smaller outage probability than $\gamma_{RF}+\gamma_{FSO}-$based TCI adaptation policy. However, when $\bar{\gamma}_{RF}$ becomes high, the outage capacity obtained when using $\gamma_{RF}+\gamma_{FSO}-$based TCI adaptation policy becomes the same as that obtained when using $\gamma_{RF}-$based TCI adaptation policy. This is because both $\gamma_{RF}+\gamma_{FSO}-$based TCI adaptation policy and $\gamma_{RF}-$based TCI adaptation policy achieve almost the same outage probability with high values of $\bar{\gamma}_{RF}$.

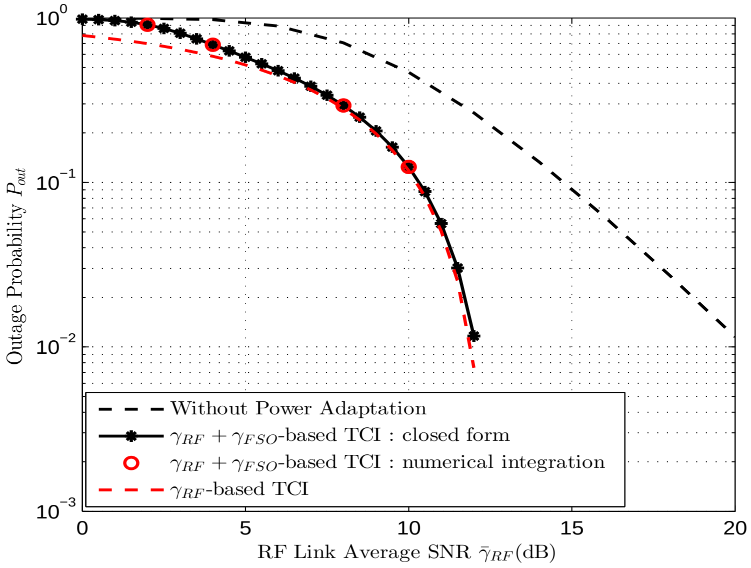

(a) Using CM/HD technique with FSO link (r=1)

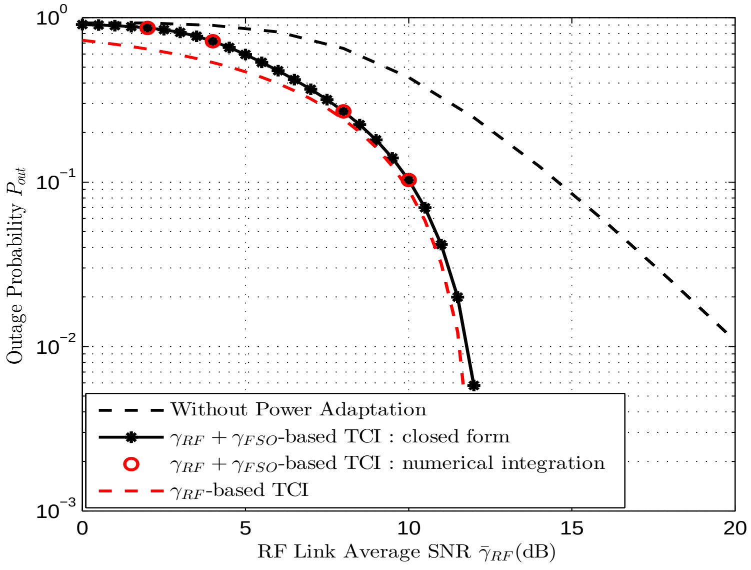

(b) Using IM/DD technique with FSO link (r=2)

Figure 4.2: Outage probability of hybrid FSO/RF system with and without power adaptation as a function of the average SNR of the RF link with γ_T=10 dB, Nakagami parameter m=2, weak atmospheric turbulence (α=2.902, and β=2.51), $\bar{\gamma}_{FSO_r}$=0 dB, and $\xi = 1$.

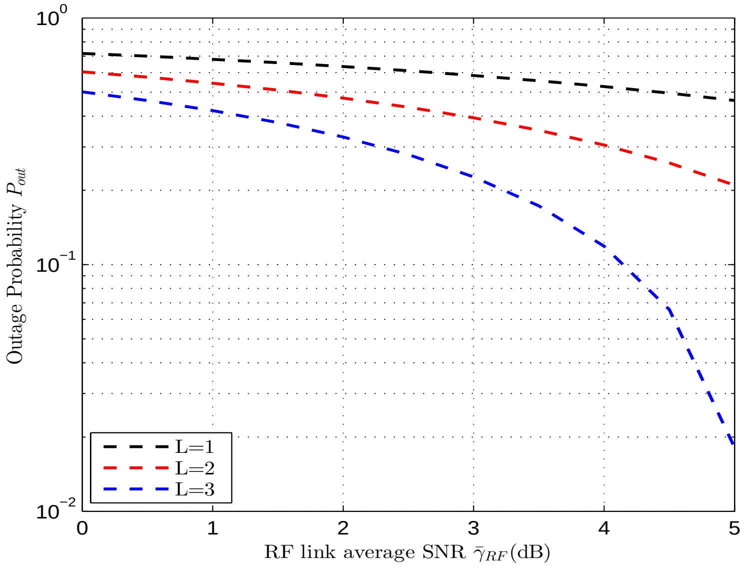

(a) Using γ_{RF}-Based TCI

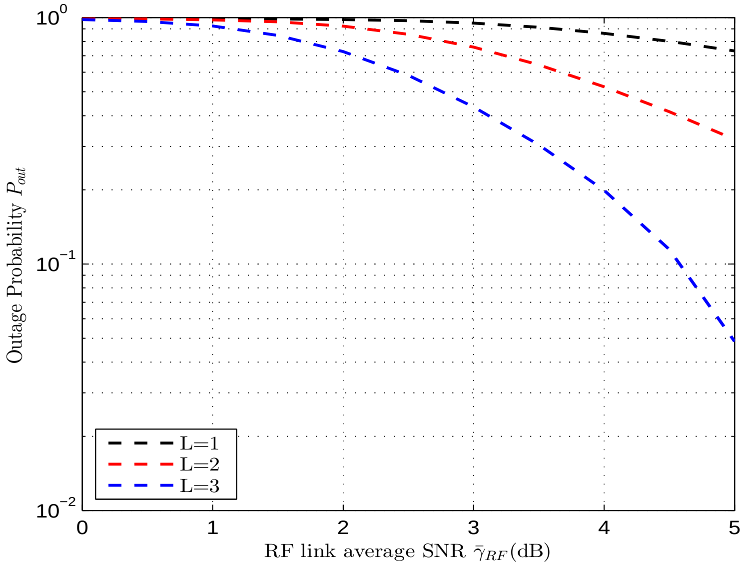

(b) Using $\gamma_{RF} + \gamma_{FSO}$-Based TCI

Figure 4.3: Outage probability of hybrid FSO/RF system with power adaptation as a function of the average SNR of the RF link considering IM/DD FSO detection technique, with γ_T=10 dB, Nakagami parameter m=2, weak atmospheric turbulence (α=2.902, and β=2.51), $\bar{\gamma}_{FSO_2}$=0 dB, and $\xi = 1$.

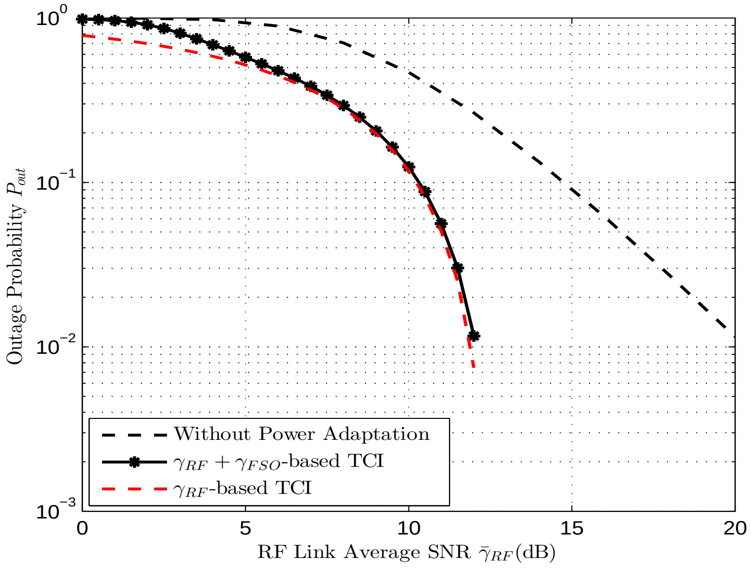

(a) Using CM/HD technique with FSO link (r=1)

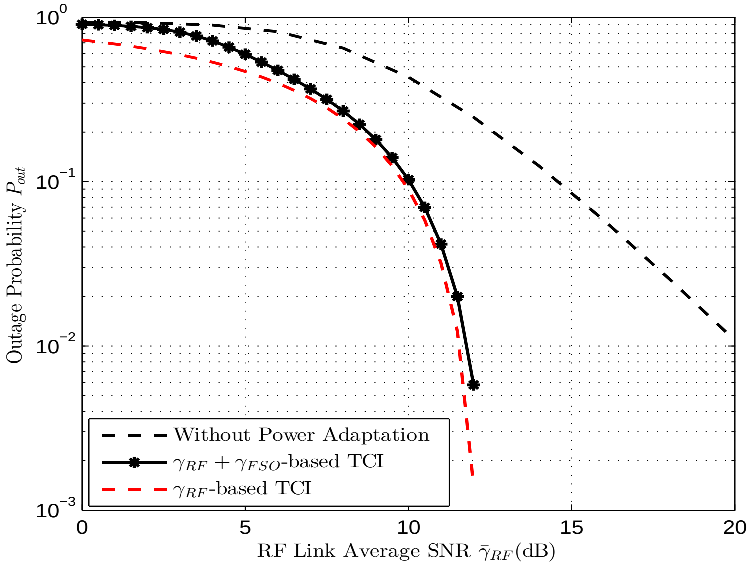

(b) Using IM/DD technique with FSO link (r=2)

Figure 4.4: Outage probability of hybrid FSO/RF system with and without power adaptation as a function of the average SNR of the RF link with γ_T=10 dB, Nakagami parameter m=2, strong atmospheric turbulence (α=2.064, and β=1.342), $\bar{\gamma}_{FSO_r}$=0 dB, and $\xi = 4$.

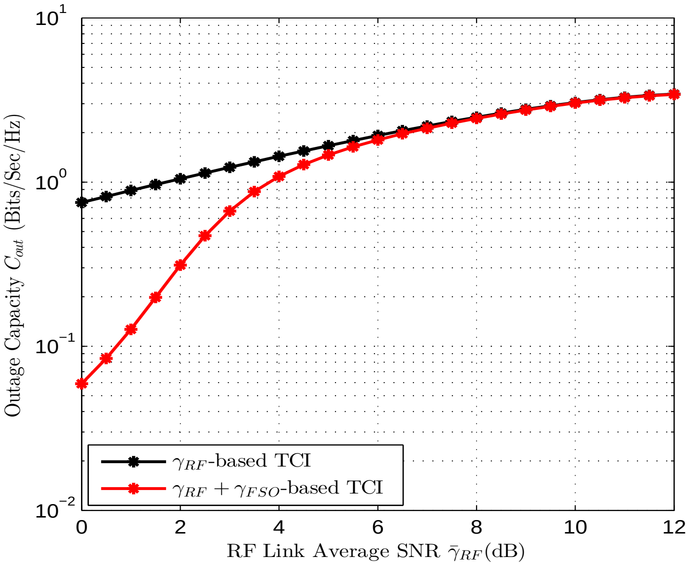

(a) Using CM/HD technique with FSO link (r=1)

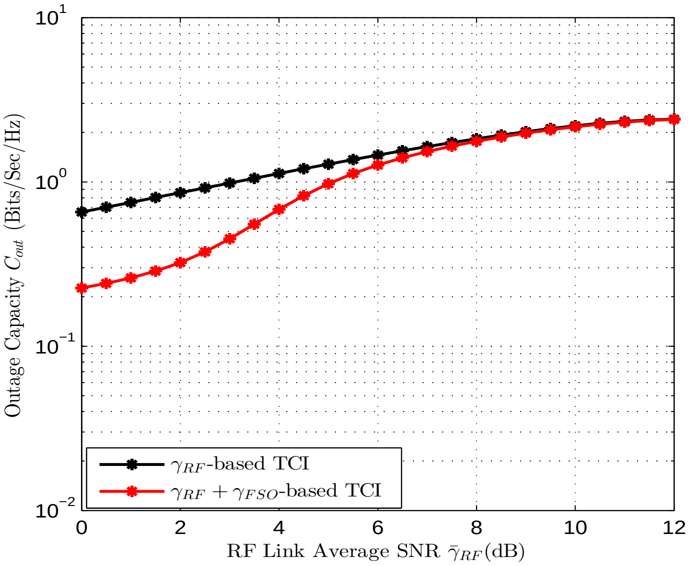

(b) Using IM/DD technique with FSO link (r=2)

Figure 4.5: Outage capacity of hybrid FSO/RF system with power adaptation as a function of the average SNR of the RF link with γ_T=10 dB, Nakagami parameter m=2, weak atmospheric turbulence (α=2.902, and β=2.51), $\bar{\gamma}_{FSO_r}$=0 dB, and $\xi = 1$.

4.5 Power Adaptation on FSO Link

To conserve more power, the transmit power over the FSO link can be adapted according to the following modified TCI policy:

$$\frac{P_{FSO}(\gamma_{FSO})}{P_{FSO_{max}}} = \begin{cases} \frac{\gamma_T}{\gamma_{FSO}}, & \text{if } \gamma_{FSO} \geq \gamma_T \\ 1, & \text{if } \gamma_{FSO} < \gamma_T. \end{cases} \tag{4.21}$$

According to this power adaptation policy, FSO power denoted by P_{FSO} gradually increases when the FSO link is in good quality (i.e., $\gamma_{FSO} \geq \gamma_T$) to reach it maximum value of $P_{FSO_{max}}$ when the FSO link quality is bad (i.e., $\gamma_{FSO} < \gamma_T$). In other words, we use constant FSO power of $P_{FSO_{max}}$ when $\gamma_{FSO} < \gamma_T$. Thus, this additional power adaptation for FSO link can further improve the power efficiency of the hybrid FSO/RF system, while maintaining the same outage performance of the system.

4.6 Summery

In this chapter, we introduced low complexity power adaptation strategy to hybrid FSO/RF systems with adaptive combining. Two power adaptation policies based on a modified TCI were implemented on the RF link of the hybrid system. We analyzed the outage performance of the proposed adaptive system and closed forms for the outage probabilities were derived. Numerical results showed that the hybrid system with power adaptation had superior outage performance compared to outage performance of the same system without power adaptation, while conserving RF power. Also, numerical results showed that γ_{RF}-based TCI adaptation policy achieves better outage performance than $\gamma_{RF} + \gamma_{FSO}$-based TCI adaptation policy.

Chapter 5

Cross Layer Analysis of Point-to-Multi-Point Hybrid FSO/RF Network

In this chapter, we consider a P2MP hybrid FSO/RF data transmission network, which consists of a number of remote nodes along with a central node. Each remote node in the network is connected to the central node via a primary FSO link. A common backup RF link is shared among all the remote nodes, where we adopt the simple switch-over hybrid FSO/RF approach. Using a common RF channel will have the major advantages of: 1) sharing the scarce RF spectrum, 2) preventing the generation of unnecessary RF interference to the environment, and 3) conserving the RF power. We study the performance of a single remote node (tagged node) rather than studying the overall system performance. Studying the tagged node allow us to investigate several performance criteria such as throughput from central node to the tagged node, the average transmit buffer size, the symbol queuing delay in the transmit buffer, the efficiency of the queuing system, the symbol loss probability, and the RF link utilization.

The remainder of the chapter is organized as follows. In section 5.1, we introduce the P2MP Hybrid FSO/RF network model and central node - remote node channel model. In section 5.2, we introduce the steady state system performance model. We study different performance metrics for the tagged node in section 5.3. Finally, section 5.4 presents some numerical examples to investigate the performance of the proposed P2MP network, followed by the chapter summary in section 5.5.

5.1 P2MP Network and Channel modeling

5.1.1 P2MP Hybrid FSO/RF Network Modeling

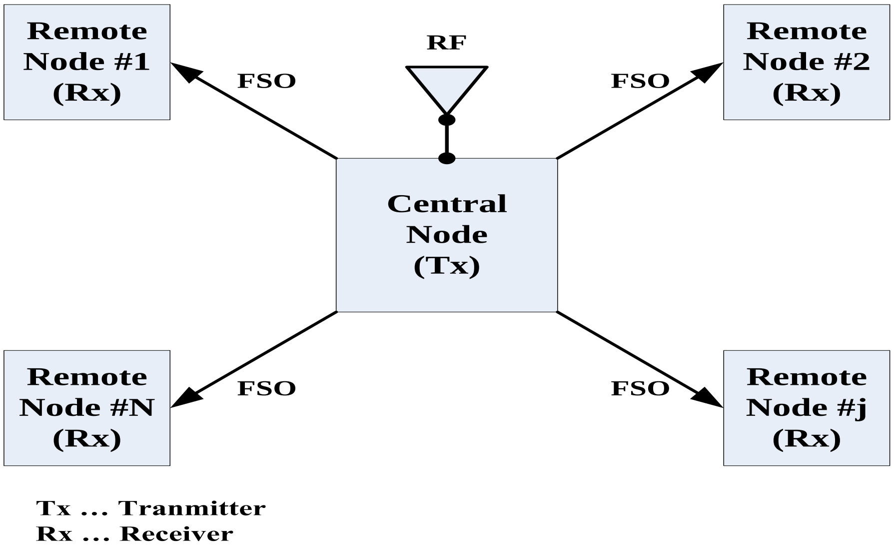

Figure 5.1: General block diagram of a P2MP Hybrid FSO/RF network.

The general block diagram of a P2MP hybrid FSO/RF network is shown in Fig. 5.1. This network consists of a central node and N remote nodes. The central node is equipped with N optical transmitters and one RF transmitter. Each remote node in the network is equipped with one optical receiver and one RF receiver. Each remote node of the network is connected to the central node through a separate primary FSO link. The central node is assumed to be aware of the quality of the N FSO links through N feedback channels. The RF transmitter of the central node is assigned a certain RF channel, which is used as a backup channel for data transmission to any remote node in case of the failure of its corresponding FSO link.

Through out the chapter, we will adopt the following assumptions:

1. When more than one FSO link fail, the central node will use the RF link to communicate with one of the corresponding remote nodes on an equal priority basis.

2. Non-saturated traffic condition is assumed. Specifically, the central node may or may not have data symbols for transmission to all N remote nodes over each time step.

3. All FSO links follow the same statistical fading distribution.
4. The data is transmitted over the FSO and RF links at the same rate.
5. No error control policy is implemented between the remote note and the central node.
6. The central node receives perfectly the states of the N FSO channels and the back-up RF channel based on feedback from the remote nodes.

The hybrid FSO/RF system used for data transmission from the central node to any remote node is composed of coherent/heterodyne FSO and RF data transmission subsystems. In this hybrid system, coded digital baseband signal, created by the signal source, is converted to an analog electrical signal through M-QAM electrical modulator. M-QAM is widely used in high-rate data transmissions over FSO links [61], and RF links [62], because of its high spectral efficiency, and low signal modulation/demodulation complexity. The QAM signal will be transmitted using either the FSO link or the RF link. At the FSO transmitter, QAM electrical signal is mixed with an optical carrier, produced by an optical frequency LO to produce the optical signal. At the FSO receiver, the received optical signal undergoes heterodyne detection process. At the RF transmitter, the frequency of the QAM electrical signal is up-converted using 60 GHz RF carrier, produced by an RF LO.

For the data transmission from the central node to any remote node, we adopt a switch-over hybrid FSO/RF transmission scheme. In this transmission scheme, only the FSO link is used for data transmission as long as the instantaneous SNR at the optical receiver of the remote node, denoted by γ_{FSO}, is above a certain threshold, defined by γ_T. When γ_{FSO} falls below the predetermined threshold γ_T, the remote node sends a 1-bit feedback signal to inform the central node to use the RF link[1] for data transmission. To meet a minimum BER requirement of BER_0, the threshold γ_T is set as [32]:

$$\gamma_T = (M-1)\left[-\frac{2}{3}\ln(5\ \text{BER}_0)\right], \quad M \geq 4 \tag{5.1}$$

---

[1] Note that the remote node is not aware whether or not the RF link is being used by the central node to transmit data to another remote node.

5.1.2 Central node - Remote node Channel Modeling

Modeling the FSO Link

The instantaneous SNR per symbol of the FSO receiver is given by [63, 64]:

$$\gamma_{FSO} = \bar{\gamma}_{FSO} h_{FSO}, \tag{5.2}$$

where $\bar{\gamma}_{FSO}$ and h_{FSO} are respectively, the average SNR and the fading gain over the FSO link, with $E[h_{FSO}]$ is normalized to unity, where $E[.]$ is the expectation operator. Assume using PLL to compensate for phase noise in the received optical signal and using large enough LO power, such that thermal and background noises can be neglected, then average SNR $\bar{\gamma}_{FSO}$ can be given by [63, 64]:

$$\bar{\gamma}_{FSO} = \frac{2E_{avg}\eta^2 P_{LO} P_{FSO} G_{FSO}}{\sigma^2_{FSO}}, \tag{5.3}$$

where E_{avg}, η, P_{LO} , P_{FSO}, G_{FSO}, and σ^2_{FSO} are respectively, the average QAM symbol energy, photodetector responsivity, LO power, average transmitted optical power, attenuation factor, and variance of shot noise which is modeled as AWGN. The attenuation factor G_{FSO} (in dB) is determined by the Beers-Lambert law as $G_{FSO} = \alpha_{FSO} z$ [26], where α_{FSO} denotes the weather attenuation coefficient (in dB/Km) and z is the link distance. The fading gain over the FSO link is defined as $h_{FSO} = h_a h_p$ [65], where h_a is Gamma-Gamma atmospheric turbulence-induced fading gain factor [54] and h_p is Gaussian pointing errors-induced fading gain factor [17].

Following the same procedure used in [65], it is easy to show that the PDF of γ_{FSO} is given by:

$$f_{\gamma_{FSO}}(\gamma_{FSO}) = \frac{\xi^2 {\gamma_{FSO}}^{-1}}{\Gamma(\alpha)\Gamma(\beta)} G^{3,0}_{1,3}\left[\frac{\xi^2\alpha\beta\gamma_{FSO}}{(\xi^2+1)\bar{\gamma}_{FSO}} \,\Big|^{\xi^2+1}_{\xi^2,\ \alpha,\ \beta}\right], \tag{5.4}$$

where ξ is the ratio between the equivalent beam radius and the pointing error (jitter) standard deviation σ_s given by $\xi = \omega_{eq}/2\sigma_s$ [17]. Here, $\omega^2_{eq} = \omega^2_z\sqrt{\pi}\mathrm{erf}(\nu)/2\nu\exp(-\nu^2)$, where erf(.) is the error function and ω_z is the optical beam radius at distance z from the transmitter aperture and $\nu = \sqrt{\pi}D/2\sqrt{2}\omega_z$ with D is the photodetector diameter. ω_z is given by $\omega_z = \theta_0 z$, where θ_0 is the transmit divergence at $1/e^2$. $\Gamma(.)$ and $G[.]$ in (5.4) are respectively, the standard Gamma function and the Meijer G-function as defined in [53, Eq. (9.301)] with α and β are the scintillation parameters. The parameters α and β are related to the refractive index structure parameter C_n^2 where the atmospheric turbulence can be modeled from weak to strong turbulence regimes. Assuming spherical optical wave propagation, expressions for calculating α and β in (5.4) are given by [54]:

$$\alpha = \left[\exp\left(\frac{0.49\chi^2}{(1+0.18d^2+0.56\chi^{\frac{12}{5}})^{\frac{7}{6}}}\right)-1\right]^{-1} \tag{5.5}$$

$$\beta = \left[\exp\left(\frac{0.51\chi^2(1+0.69\chi^{\frac{12}{5}})^{-\frac{5}{6}}}{(1+0.9d^2+0.62d^2\chi^{\frac{12}{5}})^{\frac{5}{6}}}\right)-1\right]^{-1}, \tag{5.6}$$

where $\chi^2 = 0.5C_n^2k^{7/6}z^{11/6}$ is the Rytov variance, $d = (kD^2/4z)^{1/2}$, and $k = 2\pi/\lambda_{FSO}$ is the optical wave number with λ_{FSO} is the optical wavelength.

By using [56, Eq. (07.34.21.0084.01)] and some simple algebraic manipulations, the CDF of γ_{FSO} can be expressed as:

$$F_{\gamma_{FSO}}(\gamma_{FSO}) = \frac{\xi^2}{\Gamma(\alpha)\Gamma(\beta)}G_{2,4}^{3,1}\left[\frac{\xi^2\alpha\beta\gamma_{FSO}}{(\xi^2+1)\bar{\gamma}_{FSO}}\Big|_{\xi^2,\ \alpha,\ \beta,\ 0}^{1,\ \xi^2+1}\right]. \tag{5.7}$$

Modeling the RF Link

The instantaneous SNR per symbol of the RF receiver is given by $\gamma_{RF} = \bar{\gamma}_{RF}h_{RF}^2$ [24], where h_{RF} is the fading gain over the RF channel, with $E[h_{RF}^2]$ normalized to unity, and $\bar{\gamma}_{RF}$ is the average SNR of the RF channel. The average SNR $\bar{\gamma}_{RF}$ is given by [24]:

$$\bar{\gamma}_{RF} = \frac{E_{avg}P_{RF}G_{RF}}{\sigma_{RF}^2}, \tag{5.8}$$

where P_{RF}, σ_{RF}^2, and G_{RF} are respectively, transmitted RF power, noise variance, assuming zero-mean circularly symmetric AWGN, and average power gain of the RF channel. The average power gain G_{RF} is given by [24]:

$$G_{RF}[dB] = G_T + G_R - 20\log_{10}\left(\frac{4\pi z}{\lambda_{RF}}\right) - \alpha_{oxy}z - \alpha_{rain}z, \tag{5.9}$$

where G_T and G_R denote the transmit and receive antenna gains, respectively, λ_{RF} is the wavelength of the RF channel, and α_{oxy} and α_{rain} are the attenuations caused by oxygen absorption[2] and rain, respectively. The variance of the noise in the RF channel is given by $\sigma^2_{RF} = WN_0N_F$ [24], where W is the RF bandwidth, N_0 is the noise power spectral density and N_F is the noise figure of the RF receiver.

The fading gain h_{RF} over the RF channel follows Nakagami-m distribution, which represents a wide variety of realistic LOS [59], and non LOS fading channels encountered in practice [58]. Using power transformation of random variables, it is easy to show that the PDF of γ_{RF} is given by [59]:

$$f_{\gamma_{RF}}(\gamma_{RF}) = \left(\frac{m}{\bar{\gamma}_{RF}}\right)^m \frac{{\gamma_{RF}}^{m-1}}{\Gamma(m)} \exp\left(\frac{-m\gamma_{RF}}{\bar{\gamma}_{RF}}\right). \tag{5.10}$$

By using [53, Eq. (3.351.1)], and some simple algebraic manipulations, the CDF of γ_{RF} can be expressed as:

$$F_{\gamma_{RF}}(\gamma_{RF}) = \frac{1}{\Gamma(m)}\gamma\left(m, \frac{m\gamma_{RF}}{\bar{\gamma}_{RF}}\right), \tag{5.11}$$

where $\gamma(\cdot,\cdot)$ is the lower incomplete Gamma function defined in [53, Eq. (8.350.1)].

5.2 Steady State System Performance Modeling

Since all the remote nodes are identical, we can study the system performance by focusing on one remote node, which we called the tagged node. We will use the term "other nodes" to refer to the $N-1$ remaining remote nodes.

5.2.1 Probability of Data Transmission Link Availability for a Tagged Node

We derive the probability that there is a link available for data transmission from the central node to a tagged node. We define a to be the probability that a certain FSO link is in poor quality and can't be used for data transmission from the central node to the corresponding remote node, which is given by:

$$a = \mathrm{P_r}[\gamma_{FSO} < \gamma_T] = F_{\gamma_{FSO}}(\gamma_T), \tag{5.12}$$

where $F_{\gamma_{FSO}}(.)$ is given by (5.7).

---

[2] Oxygen absorption at 60 GHz attenuates the signal at all times, regardless of the weather [57].

As we are using the same type of digital modulation on both FSO and RF links, we will use the same threshold γ_T to measure the quality of the RF link from the central node to the tagged node. We define b to be the probability that the RF link is in poor quality and can't be used for data transmission by the central node, which is given by:

$$b = \mathrm{P_r}[\gamma_{RF} < \gamma_T] = F_{\gamma_{RF}}(\gamma_T), \tag{5.13}$$

where $F_{\gamma_{RF}}(.)$ is given by (5.11).

Considering the FSO link from the central node to a tagged remote node, we define P_n to be the probability that n FSO links out of the remaining $N-1$ FSO links are in poor condition and the central node needs to use the back-up RF link for data transmission to the corresponding n remote nodes at a given time step. In this case, P_n is given by the binomial distribution as:

$$P_n = \binom{N-1}{n} a^n (1-a)^{N-n-1}, \quad n = 0, 1, 2, ..., N-1. \tag{5.14}$$

Given that the FSO link to the tagged node is in poor quality and the RF link is in good quality, we define P_{RF} to be the probability that the central node uses the RF link to transmit data to the tagged node. Based on assumption (1), P_{RF} is given by:

$$\begin{aligned} P_{RF} =& \mathrm{P_r}[\text{No other nodes need RF}] \\ & + \mathrm{P_r}[\text{tagged node and one other node need RF}]/2 \\ & + \mathrm{P_r}[\text{tagged node and two other nodes need RF}]/3 \\ & + ... \\ & + \mathrm{P_r}[\text{All other nodes need RF}]/N \\ =& P_0 + \frac{1}{2}P_1 + \frac{1}{3}P_2 + ... + \frac{1}{N}P_{N-1} \\ =& \sum_{n=0}^{N-1} \frac{1}{n+1} P_n. \end{aligned} \tag{5.15}$$

Substituting with (5.14) in (5.15) and after some algebraic manipulations with the help of the binomial theorem [71, Eq. (1.2.1.1)] , P_{RF} can be given in a more simplified form as:

$$P_{RF} = \frac{1}{aN}[1 - (1-a)^N]. \tag{5.16}$$

Note that, substituting with $N = 1$ in (5.16) leads to $P_{RF} = 1$ which corresponds to the case of point to point data transmission link from the central node to the tagged remote node with the RF link always available for data transmission conditioning that it is in good quality.

According to the quality of the FSO link from the central node to the tagged node, either the FSO link or the RF link is used for data transmission. For the RF link to be used for data transmission to a tagged node, it should be in a good quality and is not used for data transmission to another node. Thus, the probability that there is a link available for data transmission from the central node to the tagged node, denoted by P_{avl}, is defined as:

$$P_{avl} = \underbrace{1 - a}_{\text{Probability of using FSO link}} + \underbrace{a(1 - b)P_{RF}}_{\text{Probability of using RF link}} . \tag{5.17}$$

Substituting (5.16) in (5.17), P_{avl} will be given by:

$$P_{avl} = 1 - a + \left(\frac{1 - b}{N}\right)[1 - (1 - a)^N]. \tag{5.18}$$

5.2.2 Discrete-Time Markov Chain Model for the Tagged Node

The central node assigns a first-in-first-out (FIFO) transmit buffer of size B symbols for every remote node. The data symbols arrive at the transmit buffer at rate R_{in} symbols/second. This symbol rate R_{in} is related to the input data rate r in bits/second by $R_{in} = r/\log_2 M$, where M is the order of the M-QAM scheme used. The symbol arrival rate R_{in} is assumed to be the same for all the N transmit buffers. We define R_{out} as the symbol departure rate. To prevent transmit buffer overflow, we must ensure that R_{out} is greater than or equal to R_{in}. Here, the symbol arrival rate R_{in} changes over time with maximum value equal to R_{out}.

The number of symbols stored in the transmit buffer represent the state of the buffer. Thus, the buffer is in state α_i when there are i symbols in the buffer (i.e., in the queue) ready for transmission. The future state of the buffer depends only on its current state and the change from one state to another will occur at discrete time values corresponding to symbol arrival and departure events. Thus, we can use the discrete-time Markov chain to model the states of the transmit buffer for the tagged node. The time step of the discrete-time Markov chain, denoted by T, is chosen as [72]:

$$T = \frac{1}{\max(R_{in}, R_{out})} = \frac{1}{R_{out}}. \tag{5.19}$$

We define the probability of symbol arrival ω as the probability that a symbol arrives at the buffer within the time step T. Or in other words, ω is the probability that a time step T has a symbol.

Based on our choice for the time step T in (5.19), the resulting Markov chain is a single-arrival, single-departure queue. The corresponding state transition diagram of the transmit buffer of the tagged node is shown in Fig. 5.2. In Fig. 5.2, $f_0 = 1 - \omega + \omega P_{avl}$, $v = \omega(1 - P_{avl})$, $u = (1 - \omega)P_{avl}$, $f = 1 - (u + v)$, and $f_B = 1 - u$ are the states transition probabilities.

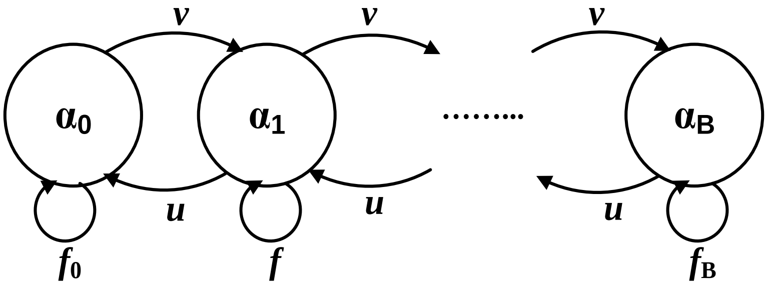

Figure 5.2: The state transition diagram for the transmit buffer of a tagged node.

The corresponding state transition matrix $\mathbf{P}$ is given by:

$$\mathbf{P} = \begin{bmatrix} f_0 & u & 0 & ... & 0 & 0 & 0 \\ v & f & u & ... & 0 & 0 & 0 \\ 0 & v & f & ... & 0 & 0 & 0 \\ \vdots & \vdots & \vdots & \ddots & \vdots & \vdots & \vdots \\ 0 & 0 & 0 & ... & f & u & 0 \\ 0 & 0 & 0 & ... & v & f & u \\ 0 & 0 & 0 & ... & 0 & v & f_B \end{bmatrix} \tag{5.20}$$

The steady state distribution vector $\mathbf{s}$ corresponding to Fig. 5.2 and (5.20) is given by:

$$\mathbf{s} = [s_0 \quad s_1 \quad ... \quad s_B]^T, \tag{5.21}$$

where s_i, $0 \leq i \leq B$, is the probability that the transmit buffer of the tagged node is in state α_i, satisfying the condition:

$$\sum_{i=0}^{B} s_i = 1. \tag{5.22}$$

At steady state, the distribution vector $\mathbf{s}$ settles down to a unique value and satisfies the following equation [72]:

$$\mathbf{P}\ \mathbf{s} = \mathbf{s}, \tag{5.23}$$

where $\mathbf{s}$ in this caes is an eigen vector for the state transition matrix $\mathbf{P}$ with corresponding eigen value equals to 1. From (5.23), we can write the following set of difference equations:

$$\begin{aligned} v\ s_0 - u\ s_1 &= 0 && (5.24)\\ v\ s_0 - v\ s_1 - u\ s_1 + u\ s_2 &= 0 && (5.25)\\ v\ s_{i-1} - v\ s_i - u\ s_i + u\ s_{i+1} &= 0,\ 0 < i < B && (5.26) \end{aligned}$$

The solution of this set of difference equations can be given in general form as [72]:

$$s_i = \rho^i s_0, \qquad 0 \leq i \leq B, \tag{5.27}$$

where

$$\rho = \frac{v}{u} = \frac{\omega(1 - P_{avl})}{(1 - \omega)P_{avl}}. \tag{5.28}$$

The solution for s_0 is obtained by substituting (5.27) in (5.22) which gives:

$$\sum_{i=0}^{B} \rho^i s_0 = 1. \tag{5.29}$$

After some algebraic manipulations of (5.29), we can obtain s_0 as:

$$s_0 = \frac{1 - \rho}{1 - \rho^{B+1}}. \tag{5.30}$$

Combining (5.27) and (5.30) the steady state distribution for the other states is given by:

$$s_i = \frac{(1-\rho)\rho^i}{1-\rho^{B+1}}, \qquad 0 \le i \le B. \tag{5.31}$$

5.3 Performance Metrics for the Tagged Node

The steady state distribution vector $\mathbf{s}$ allows us to analyze the various performance metrics as explained in the following subsections.

5.3.1 Throughput from Central Node to the Tagged Node

We define the throughput Th as the probability of transmitting a symbol over a symbol period. Conditioning on the status of the buffer, Th can be calculated as:

$$Th = \omega P_{avl} s_0 + \sum_{i=1}^{B} P_{avl} s_i, \tag{5.32}$$

where the first term on the RHS is the probability a symbol leaves the buffer when the buffer is empty. The second term on the RHS is the probability a symbol leaves the buffer when it is not empty. Using (5.22), the expression in (5.32) becomes:

$$Th = P_{avl}[1 - s_0(1-\omega)]. \tag{5.33}$$

The throughput in units of symbols/second is given by:

$$th = Th\ R_{out} \quad \text{[symbols/second]} \tag{5.34}$$

5.3.2 Average Buffer Size

The average buffer size Q_a is the average number of symbols in the buffer, which can be expressed as:

$$Q_a = \sum_{i=0}^{B} i s_i. \tag{5.35}$$

The above expression represents the weighted sum of the number of symbols in the buffer. Substituting (5.31) in (5.35) and using [71, Eq. (1.2.2.3)] the average buffer size after simplification is given by:

$$Q_a = \frac{\rho[1-(B+1)\rho^B + B\rho^{B+1}]}{(1-\rho)(1-\rho^{B+1})}. \tag{5.36}$$

5.3.3 Average Buffer Queuing Delay

The average queuing delay T_q is the average number of time steps that a symbol spends in the buffer before being transmitted. Using Little's result, this delay is given by [72]:

$$T_q = \frac{Q_a}{Th}. \tag{5.37}$$

The average queuing delay in units of seconds is given by:

$$t_q = \frac{Q_a}{th} \quad \text{[seconds]}. \tag{5.38}$$

5.3.4 Symbol Loss Probability

A symbol is lost when it arrives to a full transmit buffer and the symbol at the head of the queue does not leave. The symbol loss probability P_L is given by:

$$P_L = \omega s_B (1 - P_{avl}). \tag{5.39}$$

The symbol loss rate R_L in units of symbols/second is given by:

$$R_L = P_L \; R_{out} \quad \text{[symbols/second]}. \tag{5.40}$$

As a verification of the results, we can see that:

$$\omega = Th + P_L, \tag{5.41}$$

which is consistent to the traffic conservation principle [72], dictating that the input data rate must equal the output symbol rate plus the symbol loss rate.

5.3.5 Efficiency of the Queue

The efficiency of the queue φ is defined as the ratio of probability of a symbol leaving the buffer relative to the probability that a symbol arriving at the buffer. This can be expressed as:

$$\varphi = \frac{Th}{w} = \frac{P_{avl}[1 - s_0(1 - w)]}{w}, \tag{5.42}$$

The efficiency φ gives an indication of symbol loss due to buffer overflow. A value of $\varphi = 1$ implies no buffer overflow. A value of $\varphi < 1$ implies buffer overflow and potential symbol loss.

5.3.6 RF Link Utilization

The probability that the RF link is needed in a given time step, denoted by N_e, can be calculated as:

$$\begin{aligned} N_e &= 1 - \{\mathrm{P_r}[\gamma_{FSO} \geq \gamma_T]\}^N \\ &= 1 - \{1 - \mathrm{P_r}[\gamma_{FSO} < \gamma_T]\}^N \\ &= 1 - (1 - a)^N. \end{aligned} \tag{5.43}$$

Then the RF link utilization U defined as the probability that the RF link is used in a given time step can be calculated as:

$$U = (1 - b)N_e. \tag{5.44}$$

5.4 Numerical Results

In this section, we present several numerical examples to illustrate our analysis. We assume RF channel fading severity of m=5. Assume using 16-QAM digital modulation, γ_T is chosen to be equal to 21 dB to satisfy a minimum target BER of 10^{-6}. The relevant parameters of the FSO and RF subsystems considered for the numerical results in this paper are provided in Table 5.1 [17], [24], and [64]. The average QAM symbol energy E_{avg} is assumed to be normalized to unity. The strongest atmospheric turbulence commonly occurs when weather is clear and becomes weaker as the weather condition gets worse by means of either fog or rain. The values of C_n^2 varies from 10^{-15} to 2×10^{-13} as the atmospheric turbulence strength varies from weak to strong [17]. Mainly, the FSO link is affected by foggy weather. Thus, we consider in our numerical examples the scenario of moderate foggy weather condition with weather attenuation coefficient $\alpha_{FSO} = 42.2$ dB/Km and moderate atmospheric turbulence with $C_n^2 = 5 \times 5^{-14}$ and no rain with RF rain attenuation $\alpha_{rain} = 0$ dB/Km.

Note that, under foggy weather condition and no rain and by using the parameters given in Table 5.1, $a = 0.90$ and $b = 0.22$. These values of a and b are used in Figs. 5.3 - 5.7. In Fig. 5.8 we use arbitrary values of a with $b = 0.22$.

Table 5.1: Parameters of FSO and RF subsystems

Parameter	Symbol	Value
FSO Subsystem		
Wavelength	λ_{FSO}	1550 nm
Oscillator Power	P_{LO}	10^{-2} W
Shot Noise Variance	σ^2_{FSO}	5×10^{-12}
Responsivity	η	0.5 A/W
Photodetector Diameter	D	20 cm
Transmit Power	P_{FSO}	15 dBm
Transmit divergence at $1/e^2$	θ_0	2.5 mrad
Jitter standard deviation	σ_s	30 cm
Link distance	z	1000 m
RF Subsystem		
Carrier Frequency	f_{RF}	60 GHz
Bandwidth	W	250 MHz
Transmit Power	P_{RF}	25 dBm
Transmit Antenna Gain	G_T	43 dBi
Receive Antenna Gain	G_R	43 dBi
Noise Power Spectral Density	N_0	-114 dBm/MHz
Receiver Noise Figure	N_F	5 dB
Oxygen Attenuation	α_{oxy}	15.1 dB/Km

In Fig. 5.3, we plot the throughput Th as function of the symbol arrival probability ω for different values of N. The throughput goes into two phases viz linear and saturation. The linear phase occurs at low ω values. The saturation phase occurs for higher values of ω. The transition point occurs when the buffer is not empty (i.e., $s_0 = 0$). From (5.30), this condition occurs when $\rho = 1$. From (5.28), $\rho = 1$ occurs when the symbol arrival probability $\omega = P_{avl}$. Therefore, the linear phase of the throughput occurs in the region $\omega \in [0, P_{avl})$. The saturation phase of the throughput occurs in the region $\omega \in [P_{avl}, 1]$. Furthermore, at saturation the throughput decreases with increasing N. This is due to the increasing competition to access the shared RF link.

The dotted red line in Fig. 5.3 shows the throughput of the tagged node when there is no backup RF link. It is worth noting that this throughput is independent of value of N. While all the other lines show the cases when there is a backup RF link.

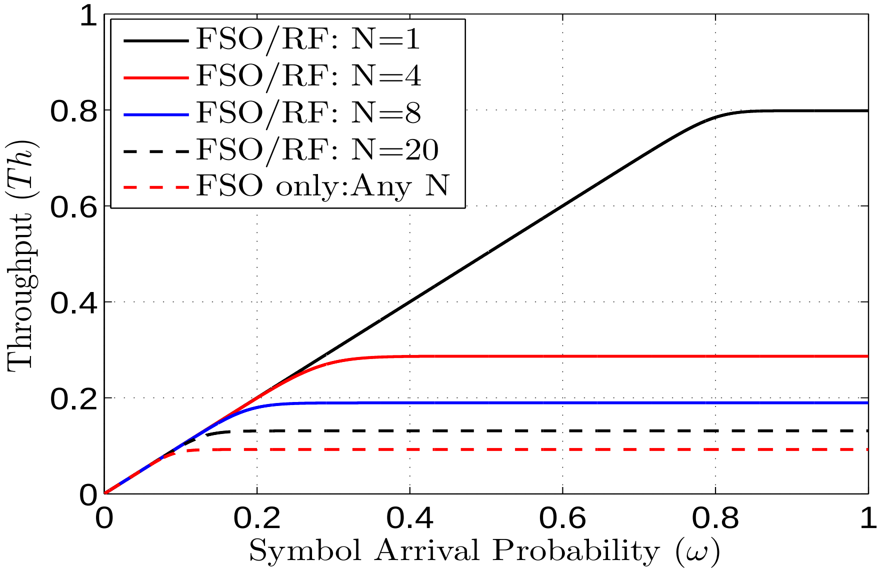

Figure 5.3: Throughput with $B = 10$ symbols.

It can be seen that using a common backup RF link had improved the throughput.

It is worth to mention that numerical simulations have shown that reducing the buffer size B results in smoother transitions between the linear and the saturation phases of the throughput. The buffer size B has no impact on the saturation values.

In Fig. 5.4, we plot the average buffer size Q_a as function of the symbol arrival probability ω for different values of N. Fig. 5.4 shows two situations for $N = 1$. The first situation is the red dotted line when there is no backup RF link. In this situation, the buffer starts filling at low symbol arrival probabilities. This is because the FSO link is in bad quality due to the foggy weather. The second situation is the solid black line when there is backup RF link and only one remote node. In this situation, the buffer starts filling at high symbol arrival probabilities. This is because the central node uses the backup RF link. The average buffer size Q_a increases with smaller values of ω as N increases. The average buffer size Q_a saturates at the maximum buffer size B as expected.

In Fig. 5.5, we plot the average queuing delay T_q as function of the symbol arrival probability ω for different values of N. The average queuing delay T_q shows an S-type behavior, where it starts at low values then starts increasing after a certain symbol arrival probability value. It then saturates. The saturation value increases with increasing values of N. The best performance occurs for the case when there is a single remote node with a backup RF link. The worst performance occurs when

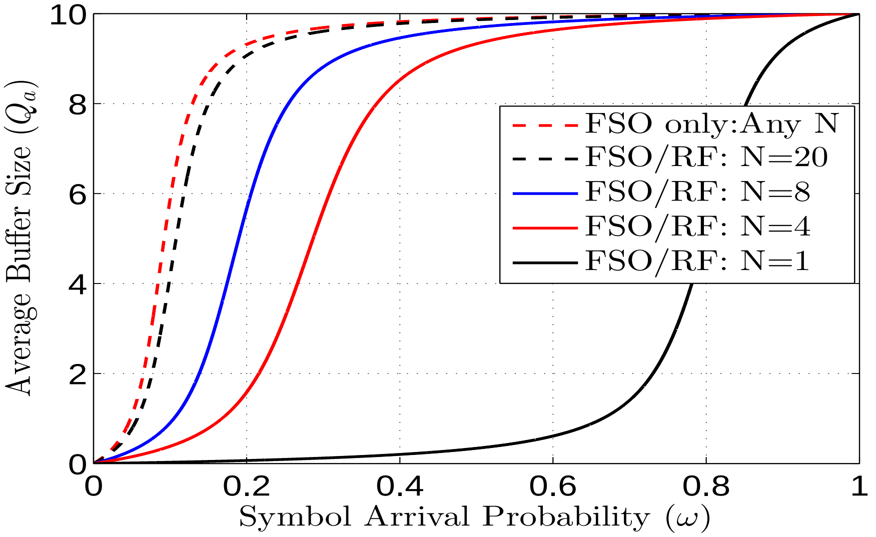

Figure 5.4: Average buffer size with $B = 10$ symbols.

there is no backup RF link. For the cases that $N > 1$ and there is a backup RF link shown in the figure by the red, blue, and dotted black lines, it is noted that the average queuing delay T_q is not equal to zero at very low value of ω. This is because, as N increases the probability P_{avl} decreases and a symbol will wait in the buffer until a link is available for its transmission. The dotted red line indicates the case when using the FSO links only without a backup RF link. We note the same observation of non-zero delay at very low value of ω. This is because there is no backup RF link and the symbol will wait until the FSO link becomes available. The special case for $N = 1$ shown in the figure by the black line will have the least average queuing delay T_q.

In Fig. 5.6, we plot the symbol loss probability P_L as function of the symbol arrival probability ω for different values of N. The symbol loss probability goes into two phases viz zero loss and linear. The zero loss phase occurs at low ω values. The linear phase occurs for higher values of ω. The transition point occurs when the buffer is full with probability $s_B > 0$. This condition is equivalent to the condition $s_0 = 0$. From (5.30), this condition occurs when $\rho = 1$. From (5.28), this occurs when the symbol arrival probability $\omega = P_{avl}$. Therefore, the zero loss phase of the symbol loss probability occurs in the region $\omega \in [0, P_{avl})$. The linear phase of the symbol loss probability occurs in the region $\omega \in [P_{avl}, 1]$.

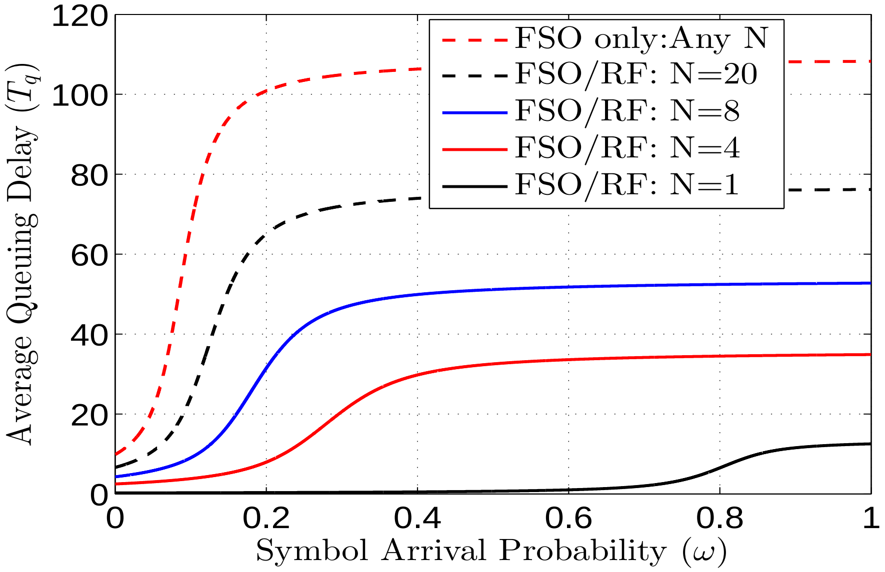

Figure 5.5: Average queuing delay with $B = 10$ symbols.

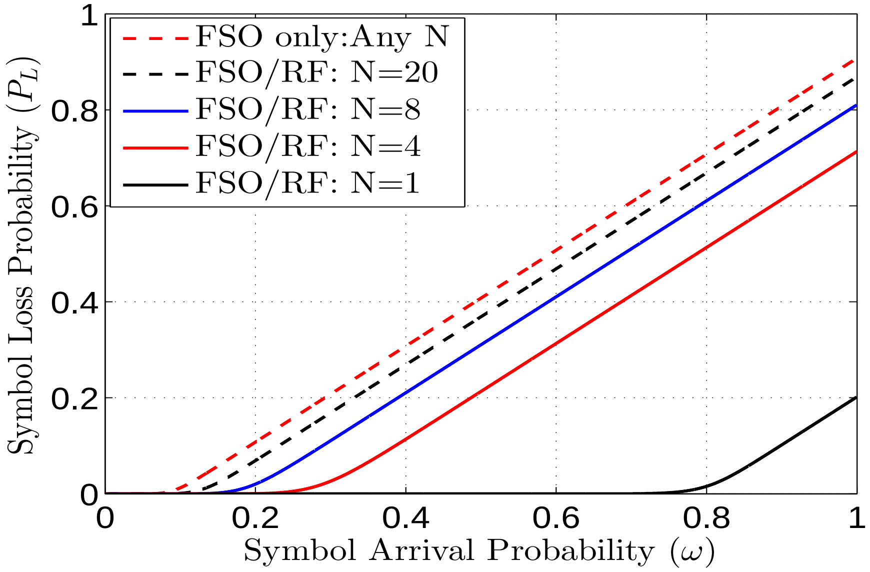

Figure 5.6: Symbol loss probability with $B = 10$ symbols.

In Fig. 5.7, we plot the efficiency φ as function of the symbol arrival probability ω for different values of N. The efficiency φ goes into two phases viz unity efficiency and decreasing efficiency. The unity efficiency phase occurs at low ω values. The decreasing efficiency occurs for higher values of ω. The transition point occurs when the buffer is not empty (i.e., $s_0 = 0$). From (5.30), this condition occurs when $\rho = 1$.

From (5.28), this occurs when the symbol arrival probability $\omega = P_{avl}$. Therefore, the unity efficiency phase occurs in the region $\omega \in [0, P_{avl})$. The decreasing efficiency phase occurs in the region $\omega \in [P_{avl}, 1]$. Furthermore, the efficiency decreases as N increases. This is due to the increasing competition to access the shared RF link. The dotted red line in Fig. 5.7 shows the efficiency of the tagged node when there is no backup RF link. It is worth noting that this efficiency is independent of value of N. While all the other lines show the cases when there is a backup RF link. It can be seen that using a common backup RF link had improved the efficiency.

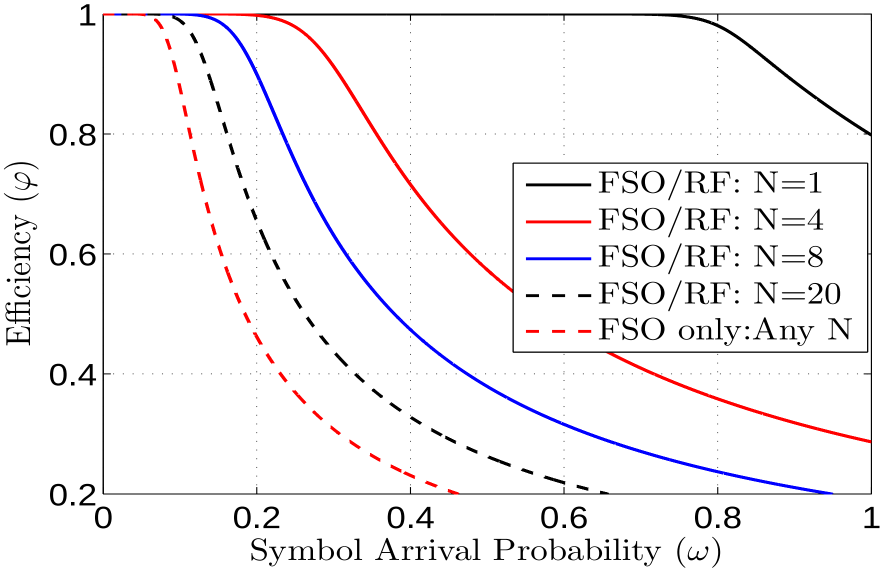

Figure 5.7: Efficiency with $B = 10$ symbols.

In Fig. 5.8, we plot the RF utilization U as function of the number of the remote nodes N for different values of the poor quality probability of the FSO link a. The RF utilization U increases as N increases until it saturates. This is because, as N increases the probability that more FSO links are in poor quality increases and thus more remote nodes will need to access the RF link. The value of the saturation depends on the quality of the RF link. For a fixed value of N, the RF link utilization increases as the FSO link quality degrads.

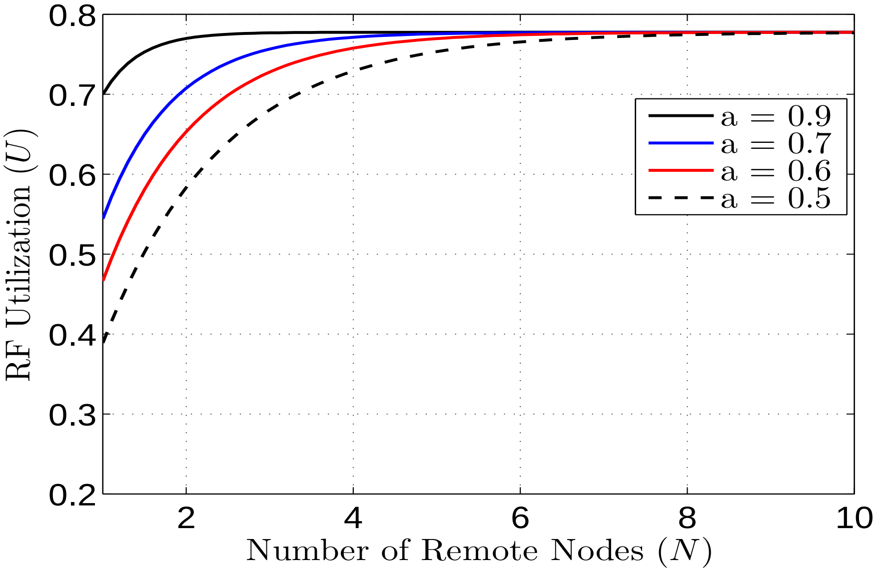

Figure 5.8: RF channel utilization

5.5 Summary

In this chapter, we proposed a novel P2MP network based on hybrid FSO/RF transmission system. A common backup RF link is used by the central node for data transmission to any remote node in case of the failure of its corresponding FSO link. The central node assigns a transmit buffer for every remote node. We studied the performance of a single remote node (tagged node) rather than studying the overall system performance. A discrete-time Markov chain model was developed for the transmit buffer of the link between the central node and the tagged remote node. Studying the tagged node allowed us to investigate several performance criteria such as throughput from central node to the tagged node, the average transmit buffer size, the symbol queuing delay in the transmit buffer, the efficiency of the queuing system, the symbol loss probability, and the RF link utilization. Numerical examples showed that the P2MP Hybrid FSO/RF network achieves considerable performance improvement over the P2MP FSO-only network.

Chapter 6

Dual-Hop VLC/RF Transmission System with Energy Harvesting Relay under Hard Delay Constraint

In this chapter, we introduce a dual-hop VLC/RF system as a new hybrid VLC/RF approach to extend the coverage of indoor VLC systems. In this approach, a second-hop RF link is used to extend the coverage of a first-hop VLC link by introducing a relay between the two hops. In order to reduce power consumption, the relay is equipped with a Photovoltaic module that harvests indoor light energy and converts it into electrical energy. The relay uses the harvested energy to retransmit the data received over the first-hop VLC link to a mobile terminal over the second-hop RF link. We investigate the data packet transmission performance of the proposed system. A main Quality-of-Service (QoS) requirement in many data services such as video and real-time multimedia streaming, high throughput file transfers and Voice-over-IP is to transmit a data packet within a strict end-to-end delay constraint. Considering the QoS requirement of transmitting a data packet of certain size from the data source to the mobile terminal within a strict time delay constraint, the probability of data packet loss is analyzed.

The remainder of the chapter is organized as follows. In section 6.1, we introduce the system and channel models of the dual-hop VLC/RF transmission system with energy harvesting relay. In section 6.2, we introduce the model for the indoor light energy harvesting at the relay. In section 6.3, we present the packet loss probability analysis of the proposed hybrid transmission system. Finally, section 6.4 presents some numerical examples to investigate the performance of the introduced system, followed by the chapter summary in section 6.5.

6.1 Dual-Hop VLC/RF Transmission System Modeling

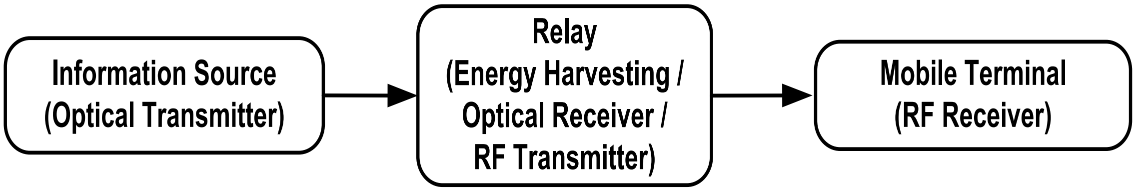

Figure 6.1: General block diagram of a dual-hop hybrid VLC/RF transmission system with energy harvesting relay.

The general block diagram of a dual-hop hybrid VLC/RF transmission system with energy harvesting relay is shown in Fig. 6.1. We assume here a time division relaying scheme which composes of two time slots. In the first time slot of duration T_1 seconds, the source terminal uses a LED optical transmitter to transmit a data packet of size B bits over the VLC channel to the relay. At the same time, the relay harvests light energy from indoor artificial light sources and from sunlight energy entering the room. In the second time slot of duration T_2 seconds, the relay harvests more light energy from the available indoor light sources and uses the harvested energy to retransmit the data packet to the mobile terminal over the second-hop RF channel. With the introduction of parameter $\alpha \in [0, 1)$, we specify the portion of T_2 used for the excess light energy harvesting as αT_2 and the portion of T_2 used for data packet retransmission as $(1 - \alpha)T_2$ as shown in Fig. 6.2. It is worth to mention here that there is no harvested energy during the RF transmission duration $(1 - \alpha)T_2$. This is because during the RF transmission, the harvested energy storage device (for example a battery) is discharging and simultaneous charging and discharging for the storage device is very challenging to implement. The relay is assumed to have a buffer to hold the data packet for the time duration of αT_2 before the data packet retransmission process begins.

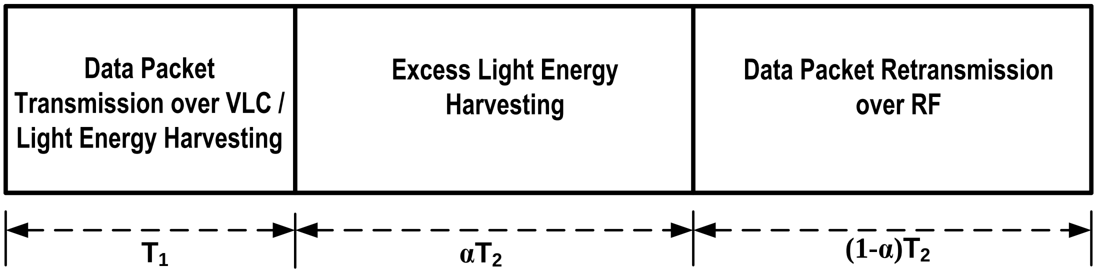

Figure 6.2: Equivalent time representation of the dual-hop hybrid VLC/RF transmission system with energy harvesting relay.

To comply with a certain QoS requirement, the total time to transmit one data packet from the source terminal to the mobile terminal $T_1 + T_2$ must not exceed a strict delay constraint of T_d seconds.

6.1.1 Modeling the First-hop from LED Source to Relay

We assume that the VLC channel can support data rate up to one Gbits/second [73]. Then, the duration of the first time slot T_1 is related to the first-hop data rate, denoted by R_1, as

$$T_1 = \frac{B}{R_1} \quad \text{[Second]}. \tag{6.1}$$

The relay terminal is assumed to be located in a fixed position, where the photo-detector[1] used for data detection at the relay has a clear LOS link to the LED source. Since the VLC channel gain depends mainly on the irradiance angle, the incidence angle of the optical signal and the distance from the LED to the photo-detector [45], which are fixed in this case, the VLC channel is considered a static channel with constant data rate R_1 here.

6.1.2 Modeling the Second-hop from Relay to Mobile Terminal

The relay will use the harvested energy during T_1 and αT_2 for its data packet retransmission to the mobile terminal during $(1-\alpha)T_2$. In the steady state, the initial stored energy present at the start of the data packet transmission over the VLC channel will

---

[1] This photo-detector can be a passive device that does not require an additional power supply for data detection [49].

be equal to the energy remaining in the harvested energy storage device after the RF retransmission of the data packet. Here, we assume that the digital signal processing operation to retrieve the data at the relay, before the RF retransmission process, only consumes a very small portion of the harvested energy, which can be neglected. Thus, the total RF retransmission energy equals to the total harvested energy. Then under the steady state condition, the total RF retransmission power, denoted by P_2, in this case is given by:

$$P_2 = \frac{P_h(T_1 + \alpha T_2)}{(1-\alpha)T_2}, \tag{6.2}$$

where P_h is the electrical power that is converted from the light energy harvested over time duration of $T_1 + \alpha T_2$ and stored in the storage device.

Accordingly, the instantaneous received SNR at the mobile terminal, denoted by γ_2, can be written as [32]:

$$\begin{aligned} \gamma_2 &= \frac{|h_2|^2 P_2}{G_2 \sigma} \\ &= \frac{|h_2|^2 P_h (T_1 + \alpha T_2)}{G_2 \sigma (1-\alpha) T_2}, \end{aligned} \tag{6.3}$$

where $|h_2|^2$ is the RF channel power gain with $E[|h_2|^2]$ normalized to unity, where $E[.]$ is the expectation operator, and σ is the power of the AWGN noise. G_2 in (6.3) is the second-hop path loss defined as [74]:

$$G_2 = \left(\frac{4\pi d_0}{\lambda}\right)^2 \left(\frac{d_2}{d_0}\right)^{\gamma}, \tag{6.4}$$

with λ is the RF carrier wavelength, d_0 is the reference distance ($d_0 = 1$m for indoor environment [74]), d_2 is the distance from the relay to the mobile terminal, and γ is the path loss exponent (typically, γ takes values 1.6 - 1.8 for indoor situations [74]).

The RF fading gain $|h_2|$ is modeled by Nakagami-m distribution, which represents a wide variety of realistic LOS and non LOS fading channels encountered in practice [58]. The PDF of $|h_2|^2$ is given by [59]:

$$f_{|h_2|^2}(z) = \frac{m^m z^{m-1}}{\Gamma(m)} \exp\left(-mz\right), \quad z \geq 0, \tag{6.5}$$

where m is the Nakagami-m parameter indicating the fading severity over the second-hop RF channel. By using [53, Eq. (3.351.1)], and some simple algebraic manipulations, the CDF of $|h_2|^2$ can be expressed as:

$$F_{|h_2|^2}(z) = \frac{1}{\Gamma(m)}\gamma\left(m, mz\right), \quad z \geq 0, \tag{6.6}$$

where $\gamma(\cdot,\cdot)$ is the lower incomplete Gamma function defined in [53, Eq. (8.350.1)].

The highest data rate that can be supported by the second-hop RF channel, denoted by R_2, is related to the SNR γ_2 and is given by the well-known Shannon formula as [32]:

$$R_2 = W\log_2\left(1+\gamma_2\right) \quad \text{[bits/second]}, \tag{6.7}$$

where W is the RF channel bandwidth in Hertz (Hz).

6.2 Modeling Energy Harvesting at the Relay

We now propose a statistical model for the harvested energy which will be used in analyzing the packet loss probability in the next section. The relay is equipped with an excess photovoltic module[2] which harvests light energy from indoor artificial light sources and sunlight energy entering the room and converts it into electrical energy. The harvested electrical power by the photovoltic cell P_h is given by [50]:

$$P_h = 0.75 I_{sc} V_{oc}, \tag{6.8}$$

where I_{sc} and V_{oc} are, respectively, the short circuit current and the open circuit voltage of the photovoltaic cell. The short circuit current I_{sc} varies with the variations in the light intensity I as $I_{sc} = CI$, where C is a constant that depends on the type of the photovoltic cell used[3] and its manufacture parameters [50]. The open circuit voltage V_{oc} is related to I_{sc} as [50]:

$$V_{oc} = V_t \ln\left(\frac{I_{sc}}{I_0}+1\right), \tag{6.9}$$

where V_t is the thermal voltage ($V_t \approx 25$ mVolt) and I_0 is the dark saturation current of the photovoltic cell, which is the photovoltic cell leakage current in the absence of

---

[2] Note that, this photovoltic module is different from the photo-detector that is used for data packet reception over the VLC channel.

[3] For example the amorphous silicon (a-Si) photovoltic cells which have a relatively high efficiency at low light levels, compared to other types of photovoltic cells [51], that makes them particularly suited for indoor uses.

light (I_0 is in the order of $10^{-9} \sim 10^{-12}$ Ampere [75]). Thus, the harvested electrical power P_h in (6.8) can be rewritten as:

$$P_h = 0.75\ V_t\ I_{sc} \ln\left(\frac{I_{sc}}{I_0} + 1\right). \tag{6.10}$$

Due to the random motion of the people within the room, the photovoltic module is susceptible to shadowing effect and will receive various reflected light components. Thus, the intensity of the incident light on the photovoltic cell I is a random variable which can be modeled by the common Log-normal distribution in such cases [32]. Accordingly, the short circuit current of the photovoltic cell I_{sc}, which depends on the incident light intensity I, is also a random variable that follows the Log-normal distribution $I_{sc} \sim \mathrm{LN}(\mu_x, \sigma_x)$, where μ_x and σ_x are the mean and the standard deviation of I_{sc}. Then, the PDF of I_{sc} is given by:

$$f_{I_{sc}}(x) = \frac{1}{x\sqrt{2\pi}\sigma_{\ln x}} \exp\left[-\frac{(\ln(x) - \mu_{\ln x})^2}{2\sigma_{\ln x}^2}\right], \tag{6.11}$$

where $\mu_{\ln x}$ and $\sigma_{\ln x}$ are the mean and standard deviation of the logarithmic samples of I_{sc} and are related to μ_x and σ_x by [56]:

$$\mu_{\ln x} = \ln\left(\frac{\mu_x^2}{\sqrt{\mu_x^2+\sigma_x^2}}\right), \quad \sigma_{\ln x} = \sqrt{\ln\left(\frac{\sigma_x^2}{\mu_x^2} + 1\right)}. \tag{6.12}$$

Proposition 1. *The output power from the photovoltic cell can be modeled as a Log-normal distribution, $P_h \sim LN(\mu_y, \sigma_y)$, where μ_y and σ_y are the mean and the standard deviation of P_h. Then, the PDF of P_h is given by:*

$$f_{P_h}(y) = \frac{1}{y\sqrt{2\pi}\sigma_{\ln y}} \exp\left[-\frac{(\ln(y) - \mu_{\ln_y})^2}{2\sigma_{\ln y}^2}\right], \tag{6.13}$$

where $\mu_{\ln y}$ and $\sigma_{\ln y}$ are the mean and standard deviation of the logarithmic samples of P_h and are related to μ_y and σ_y by:

$$\mu_{\ln y} = \ln\left(\frac{\mu_y^2}{\sqrt{\mu_y^2+\sigma_y^2}}\right), \quad \sigma_{\ln y} = \sqrt{\ln\left(\frac{\sigma_y^2}{\mu_y^2} + 1\right)}. \tag{6.14}$$

The mean μ_y of P_h is calculated as:

$$\mu_y = \int_0^\infty 0.75V_t \; x \ln\left(\frac{x}{I_0} + 1\right) f_{I_{sc}}(x)dx, \tag{6.15}$$

which can be evaluated by numerical integration, and the standard deviation σ_y of P_h is calculated as:

$$\sigma_y = V_t \; \sigma_x \; \left[\frac{\mu_x}{\mu_x + I_0} + \ln\left(\frac{\mu_x}{I_0} + 1\right)\right]. \tag{6.16}$$

Proof: see appendix A.

6.3 Packet Loss Probability Analysis of the Dual-hop VLC/RF system

The main goal here is to successfully transmit the data packet within a fixed time duration of T_d. An important performance metric in this case is the packet loss probability.

Given the total transmission time constraint T_d, the data packet retransmission time duration of $(1 - \alpha)T_2$ must not exceed the value of $T_d - T_1 - \alpha T_2$. As such the relay must retransmit the data packet with minimum data rate of R_{2_T} given by:

$$R_{2_T} = \frac{B}{T_d - T_1 - \alpha T_2} \tag{6.17}$$

to satisfy the strict end-to-end delay constraint of T_d.

The data packet will be lost if the data rate in (6.17) exceeds the Shannon limit given in (6.7). Or in other words, the data packet will be lost if the RF channel can not support the requirement of this minimum data rate R_{2_T}. Then the probability of data packet loss is given by:

$$P_{PL} = P_r[R_2 < R_{2_T}]. \tag{6.18}$$

Substituting with (6.7) in (6.18) and after some mathematical manipulation, (6.18) can be rewritten as:

$$P_{PL} = P_r[\gamma_2 < \gamma_{2T}], \tag{6.19}$$

where $\gamma_{2T} = 2^{\frac{R_{2_T}}{W}} - 1$.

This means that the packet is lost if the received SNR γ_2 at the mobile terminal is less than the threshold value of γ_{2T}. This can happen due to insufficient harvested light energy at the relay or poor RF channel from the relay to the mobile terminal. Thus, after substitution with (6.3) in (6.19), P_{PL} can be calculated as:

$$\begin{aligned} P_{PL} &= P_r\left[\frac{|h_2|^2 P_h(T_1+\alpha T_2)}{G_2\sigma(1-\alpha)T_2} < \gamma_{2T}\right] \\ &= P_r\left[|h_2|^2 < \frac{A}{P_h}\right], \end{aligned} \tag{6.20}$$

where $A = G_2\sigma\gamma_{2T}(1-\alpha)T_2/(T_1+\alpha T_2)$.

Conditioning on P_h, the probability of packet loss P_{PL} in (6.20) is given by:

$$\begin{aligned} P_{PL} &= \int_0^\infty P_r\left[|h_2|^2 < \frac{A}{y} \mid y\right] f_{P_h}(y)dy \\ &= \int_0^\infty \frac{\gamma\left(m, m\frac{A}{y}\right)}{\Gamma(m)} \frac{1}{y\sqrt{2\pi}\sigma_{\ln y}} \exp\left[-\frac{(\ln(y)-\mu_{\ln y})^2}{2\sigma_{\ln y}^2}\right] dy. \end{aligned} \tag{6.21}$$

By using the change of variable $t = \frac{\ln(y)-\mu_{\ln y}}{\sqrt{2}\ \sigma_{\ln y}}$, P_{PL} in (6.21) can be rewritten as:

$$P_{PL} = \frac{1}{\sqrt{\pi}\ \Gamma(m)} \int_{-\infty}^{\infty} f(t)\ e^{-t^2} dt, \tag{6.22}$$

where $f(t) = \gamma\left(m, mAe^{-\left(\sqrt{2}\sigma_{\ln y}t+\mu_{\ln y}\right)}\right)$, with $\gamma(\cdot,\cdot)$ as the lower incomplete Gamma function defined in [53, Eq. (8.350.1)].

The term $\int_{-\infty}^{\infty} f(t)\ e^{-t^2}dt$ in (6.22) has the form of the Gaussian-Hermite integration which can be closely approximated as [76]:

$$\int_{-\infty}^{\infty} f(t)\ e^{-t^2}dt \approx \sum_{i=1}^{N} \omega_i f(t_i), \tag{6.23}$$

where t_i and ω_i are abscissas and weight factors for the Gaussian-Hermite integration. t_i and ω_i for different values of N are available in [76, Table (25.10)], or can be calculated by a simple MATLAB program. Therefore, P_{PL} can be approximately calculated in a closed form as:

$$P_{PL} = \frac{1}{\sqrt{\pi}\,\Gamma(m)} \sum_{i=1}^{N} \omega_i f(t_i). \tag{6.24}$$

There is a trade-off between the portion of the second time slot αT_2 consumed for excess light energy harvesting and the time portion $(1-\alpha)T_2$ used for data packet retransmission over the second-hop. If α is large, more light energy will be harvested and more power will be available for the retransmission process, while less time will be available for the data packet retransmission process. On the other hand, if α is small, less light energy will be harvested and less power will be available for the retransmission process, although the time available for the data packet retransmission process is large in this case. Thus, we optimize the parameter α in terms of minimizing the data packet loss probability.

The optimal parameter α^*, which minimizes the packet loss probability P_{PL} can be obtained by solving $\partial P_{PL}/\partial\alpha = 0$ for α. However, it will be difficult to obtain the optimal α^* in closed form. As an alternative method, we can treat the problem as one-dimensional optimization problem with uncertainty range of $[0, 1)$, and use numerical methods, such as Golden-section search method [68] to search for the optimal α^*.

6.4 Numerical Results

In this section, we present numerical examples to illustrate our analysis. We assume that a data packet of size $B = 8000$ bits is to be transmitted from the LED source to the mobile terminal within the time delay constraint of $T_d = 1000$ micro seconds. The LED source is transmitting with data rate of $R_1 = 1$ Gbits/second. We assume the mean and the standard deviation of the short-circuit of the photovoltic cell to be $\mu_x = 3 \times 10^{-5}$ Ampere and $\sigma_x = 0.5 \times 10^{-5}$ Ampere. The RF carrier frequency is $f = 2.4$ GHz and the RF channel bandwidth is $W = 20$ MHz which are taken from the WiFi 802.11 g protocol, along with RF AWGN power of $\sigma = 5 \times 10^{-12}$ Watt and RF fading severity of $m = 3$.

In Fig. 6.3, we plot the packet loss probability as function of the parameter α for different values of the distance d_2 from the relay to the mobile terminal and a fixed path loss exponent of $\gamma = 1.6$. The numerical results shown in Fig. 6.3 are obtained using N=30 in (6.24). It can be observed that evaluating P_{PL} using the

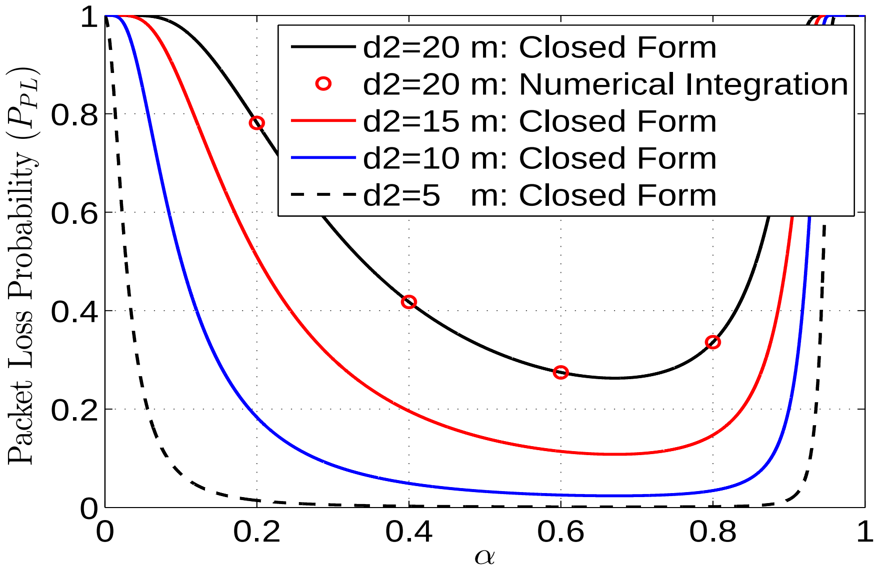

Figure 6.3: Packet loss probability for different values of d_2 with $\gamma = 1.6$.

approximated closed form gives accurate results that coincide with the values of P_{PL} obtained by evaluating the integral in (6.21) using numerical methods. Starting from a small value of α close to zero in Fig. 6.3, P_{PL} decreases with the increase of α until it reaches its minimum value at α^*. This is because, as α increases, more light energy is harvested at the relay and thus more electrical power is available for data packet retransmission process. However, as α increases over α^*, the time available for data packet retransmission is reduced and the data rate R_{2_T} increases. Although more light energy was harvested, the RF channel can not support the minimum required data rate R_{2_T} to maintain the time delay constraint of T_d. Thus, P_{PL} starts to increase. By numerical search, we can find that the optimal portion of the second-hop time duration T_2 to harvest more light energy is $\alpha^* = 0.6713$ in this case. By simple calculation, we can find that $R_{2_T} = 24.5$ Mbits/second at $\alpha = \alpha^*$. We can observe that the value of α^* is independent of the distance d_2. This could be explained with the aid of (6.20) and (6.24). Performing the partial differentiation of P_{PL} in (6.24) with respect to α will include performing the partial differentiation of A defined in (6.20) with respect to α. As G_2 is a multiplicative term of A, then when equating the partial derivative with zero to find the optimal α, the term G_2 will be eliminated. Thus, G_2 does not affect the value of α^*.

For a fixed value of α in Fig. 6.3, the available power for RF transmission is fixed. Therefore, as the remote terminal moves far away from the relay (i.e., d_2 increases), the performance of the hybrid VLC/RF transmission system degrades, as expected.

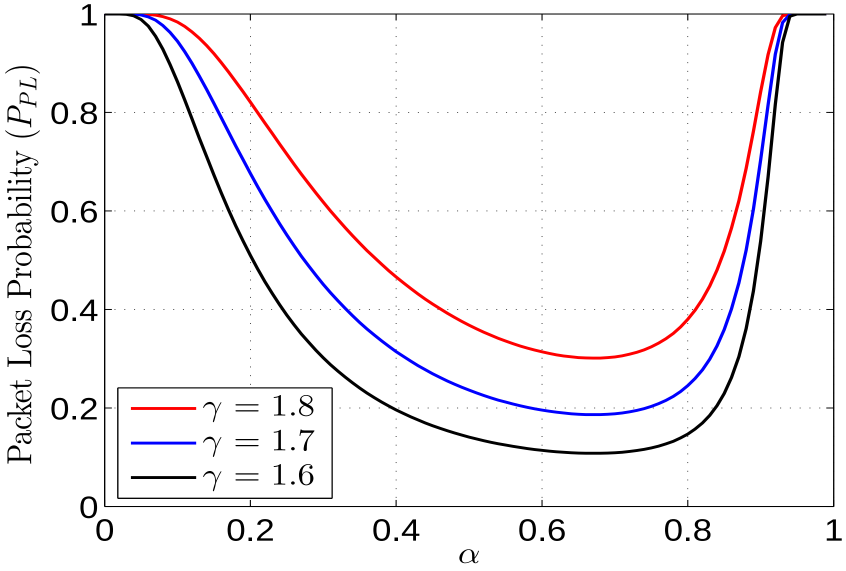

Figure 6.4: Packet loss probability for different values of γ with $d_2 = 15m$.

In Fig. 6.4, we plot the packet loss probability as function of the parameter α for different values of the path loss exponent γ and fixed value of the remote terminal distance from the relay of $d_2 = 15$ m. It can be seen from Fig. 6.4, that as γ increases, the packet loss probability increases due to the increase of the RF channel path loss.

In Fig. 6.5, we plot the packet loss probability P_{PL} as function of the parameter α for different values of the packet size B and fixed value of the remote terminal distance from the relay of $d_2 = 15$ m and a fixed path loss exponent of $\gamma = 1.6$. The relation between P_{PL} and α follows the same trend as in Fig. 6.3. It can be seen that increasing the packet size B leads to an increase in the packet loss probability for the same value of α. This can be explained with the aid of (6.17). Increasing the packet size B leads to proportionate increase in the RF transmission rate R_{2T}. This leads to increase in packet loss probability P_{PL}. It can be noticed that as B increases, the optimal value α^* decreases.

It is worth noting that the value of μ_x reflect the amount of light energy that can be harvested. Thus, as μ_x increases, more electrical power on average will be available for the data packet retransmission process over the second-hop RF channel, and thus the probability of packet loss will decrease and all the curves in Fig. 6.3 and Fig. 6.4 will go down. Also, it is worth noting that the system performance in terms of the data packet loss probability is improved by increasing the delay time constraint

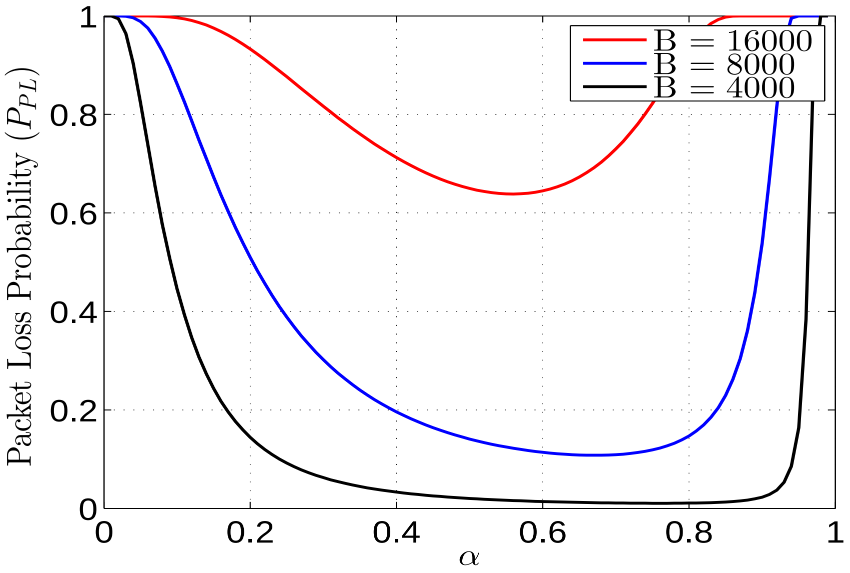

Figure 6.5: Packet loss probability for different values of B with $d_2 = 15m$ and $\gamma = 1.6$.

T_d. This is because increasing T_d allows more time to harvest light energy and to retransmit the data packet over the second-hop RF channel at lower data rate.

6.5 Summary

In this chapter, we introduced a dual-hop VLC/RF transmission system with an energy harvesting relay to extend the coverage of indoor VLC systems. The relay between the two hops harvests indoor light energy which is used to retransmit the data packet to the mobile terminal over the RF channel. We considered a main QoS constraint for the data services applications, which is transmitting a data packet to the mobile terminal within a strict end-to-end time delay. Considering this QoS constraint, we analyzed the probability of data packet loss. The parameter α determines the time available for excess light energy harvesting and the time available for data packet retransmission. This parameter was found to affect the system performance. An optimal value of α exists that minimizes packet loss probability. This optimal value was found to be independent of the mobile terminal distance and the path loss exponent. However, the optimal value of α showed inverse dependence on the packet size. For a certain value of packet size B, the optimal value α^* can be determined off-line using standard optimization techniques such as golden-section search method.

Chapter 7

Optimal Design of Dual-Hop VLC/RF Communication System with Energy Harvesting

In this chapter, we introduce a dual-hop VLC/RF system as a new approach in hybrid VLC/RF systems to extend the coverage of indoor wireless system based on VLC. In this proposed hybrid VLC/RF system, the optical source, specifically a LED source uses a SIM scheme to transmit the information over a VLC channel to a relay. The relay uses DD scheme to retrieve the information. The relay harvests energy from the LED light. Then, the second-hop RF transmission uses the harvested energy over the first-hop VLC transmission to retransmit these information to a mobile terminal.

The remainder of the chapter is organized as follows. In section 7.1, we introduce the dual-hop VLC/RF transmission system model. In section 7.2, we design the optimal VLC bias and analysis the performance of the proposed system in terms of its average end-to-end data rate. Finally, section 7.3 presents some numerical examples to investigate the performance of the proposed hybrid VLC/RF transmission system, followed by the chapter summary in section 7.4.

7.1 Dual-Hop VLC/RF Transmission System Modeling

The general block digram of a dual-hop hybrid VLC/RF communication system with energy-harvesting relay is shown in Fig. 7.1. Assuming time division relaying scheme,

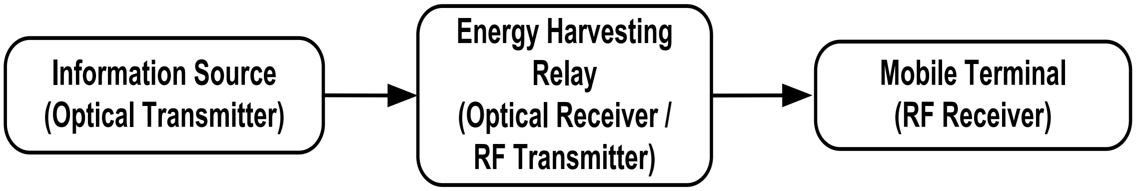

Figure 7.1: General block digram of a dual-hop hybrid VLC/RF system

in the first time slot of duration T_1, the information source terminal sends its signal over the VLC channel to the relay terminal. In the second time slot of duration T_2, the relay retransmits the source information to the mobile terminal over the RF channel. The relay harvests the light energy from the LED source during T_1 and T_2. Here, the relay is assumed to be located in a fixed position, where it has a clear LOS communication link to the LED source. On the other hand, the designated user can move freely within the room. A detailed block digram of the proposed system is shown in Fig. 7.2, which will be discussed in the following subsections.

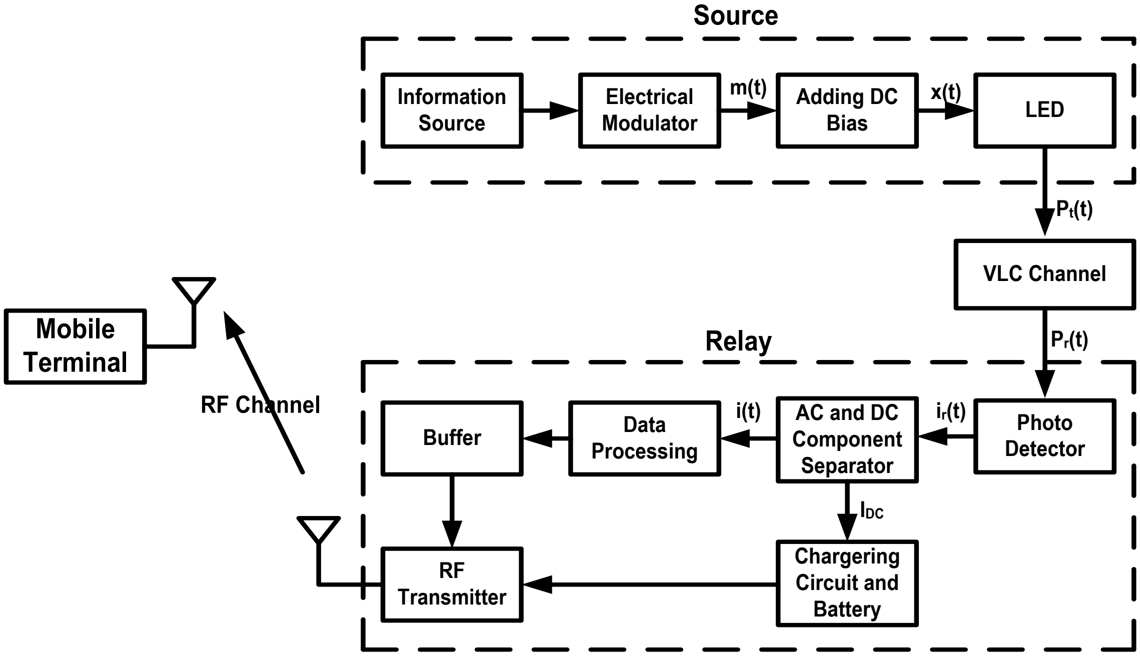

Figure 7.2: Detailed block digram of a dual-hop hybrid VLC/RF system

7.1.1 Optical Signal Transmission and Detection

The bit stream from the information source is first used to modulate an RF subcarrier to produce signal $m(t)$. A DC bias B is added to the electrical modulated signal to insure that $m(t)$ is non-negative, before being used to modulate the optical intensity of a LED array. At the same time, this DC bias places the LED in the proper operation mode. The transmitted optical signal can be written as:

$$P_t(t) = NP_{LED}[B + m(t)], \tag{7.1}$$

where N is the number of LEDs in the LED array, and P_{LED} is the single LED power with units of Watt/Ampere assuming identical LEDs. At the relay, the received optical power is converted into electrical current through direct detection at the photo-detector. The electrical current $i_r(t)$ at the output of the photo-detector can be written as:

$$i_r(t) = \eta H P_t(t) + n(t) = I_{DC} + i(t) + n(t), \tag{7.2}$$

where η is the photo-detector responsivity in A/W and H is the VLC channel power gain. $n(t)$ is an AWGN coming from ambient shot light noise and thermal noise, with zero mean and total variance $\sigma_1^2 = \sigma_{shot}^2 + \sigma_{thermal}^2$, where σ_{shot}^2 is the shot noise variance and $\sigma_{thermal}^2$ is the thermal noise variance [79]. Thus, the noise power is given by $\sigma_1^2 = N_0 W$, where N_0 is the noise power spectral density and W is the modulation bandwidth for the LED [45].

The VLC channel power gain H is given by [80]:

$$H = \frac{A_r(\xi + 1)}{2\pi d_1^2} \cos^{\xi}(\phi) \cos(\psi), \tag{7.3}$$

where A_r is the physical area of the photo-detector, ξ is the Lambert index that depends on the semi-angle at half luminance $\phi_{1/2}$, as $\xi = -1/\log_2 \cos(\phi_{1/2})$, d_1 is the transmission distance from the LED to the illuminated surface of the photo-detector, ϕ is the irradiance angle, and ψ is the incidence angle.

7.1.2 Information Processing at the Relay

From (7.2), the AC component $i(t) = \eta HNP_{LED}m(t)$ carries the information. To avoid clipping distortion by the nonlinearity of the LED, the input electrical signal to the LED must be within the linear region of LED operation. This can be done by adjusting the DC bias current B such that it is within the dynamic range of operation of the LED denoted by $D \underline{\Delta} I_H - I_L$, where I_L denotes the minimum input bias current and I_H denotes the maximum input bias current. In this case, the input electrical signal $m(t)$ varies around the DC bias B with peak amplitude given by:

$$A = \begin{cases} B - I_L, & \text{if } B < \frac{I_L + I_H}{2} \\ I_H - B, & \text{if } B \geq \frac{I_L + I_H}{2}. \end{cases} \tag{7.4}$$

Thus, the received electrical power P_r^e will be given by $P_r^e = (\eta HNP_{LED}A)^2$. The received electrical SNR at the relay, denoted by γ_1, can then be defined as:

$$\gamma_1 = \frac{(\eta HNP_{LED}A)^2}{\sigma_1^2}. \tag{7.5}$$

7.1.3 Energy Harvesting at the Relay

The maximum amount of energy that the relay can harvest is given by [50]:

$$E_h = 0.75 I_{DC} V_{oc} (T_1 + T_2), \tag{7.6}$$

where $I_{DC} = \eta HNP_{LED}B$ is the DC component of the output current $i_r(t)$ from the photo-detector and V_{oc} is the open circuit voltage of the photo-detector. V_{oc} is related to I_{DC} as $V_{oc} = V_t \ln\left(\frac{I_{DC}}{I_0} + 1\right)$ [50], where V_t is the thermal voltage ($V_t \approx 25$ mVolt) and I_0 is the dark saturation current of the photo-detector (I_0 is in the order of $10^{-9} \sim 10^{-12}$ Ampere [75]). E_h is upper bounded by $E_h = 0.75 T_1 V_t I_{DC}^2 / I_0$.

The harvested energy is used for three purposes in our system: 1) to power data processing electronics, 2) to power charging circuit electronics, and 3) to charge the battery for the RF transmission. In general, the data processing and charging management circuit consumes much less energy compared to the RF transmission.

7.1.4 Information Transmission over RF Channel

The relay will use the harvested energy E_h, which is stored in the battery, to retransmit the data to the mobile terminal during T_2. At steady state condition, the RF retransmission power is equal to E_h/T_2. Accordingly, the instantaneous received SNR at the mobile terminal, denoted by γ_2 can be defined as:

$$\gamma_2 = \frac{|h_2|^2 E_h/T_2}{G_2\sigma_2}, \tag{7.7}$$

where $|h_2|^2$ is the RF channel power gain with $E[|h_2|^2]$ normalized to unity, where $E[.]$ is the expectation operator, and σ_2 is the noise power assuming AWGN noise. G_2 is the second-hop path loss defined as $G_2 = (4\pi d_0/\lambda)^2 (d_2/d_0)^\gamma$, with λ is the used RF carrier wavelength, $d_0 = 1m$ is the reference distance, d_2 is the distance from the relay to the destination terminal, and γ is the path loss exponent (typically, γ takes values 1.6 - 1.8 in indoor situations [74]). The RF fading gain h_2 is modeled by Nakagami-m distribution. The PDF of $|h_2|^2$ is given by [59] as

$$f_{|h_2|^2}(|h_2|^2) = \frac{m^m (|h_2|^2)^{m-1}}{\Gamma(m)} \exp\left(-m|h_2|^2\right), |h_2|^2 \geq 0, \tag{7.8}$$

where m is the Nakagami-m parameter indicating the fading severity over the second-hop RF channel. Accordingly, the received SNR γ_2 will have the following PDF and CDF, respectively as [59]

$$f_{\gamma_2}(\gamma_2) = \frac{\left(\frac{m}{\bar{\gamma}_2}\right)^m {\gamma_2}^{m-1}}{\Gamma(m)} \exp\left(-\frac{m\gamma_2}{\bar{\gamma}_2}\right), \gamma_2 \geq 0, \tag{7.9}$$

$$F_{\gamma_2}(\gamma_2) = \frac{1}{\Gamma(m)} \gamma\left(m, \frac{m\gamma_2}{\bar{\gamma}_2}\right), \gamma_2 \geq 0, \tag{7.10}$$

where $\bar{\gamma}_2$ is the average SNR of the second-hop RF channel given by $\bar{\gamma}_2 = E_h/T_2 G_2 \sigma_2$ and $\gamma(\cdot,\cdot)$ is the lower incomplete Gamma function defined in [53, Eq. (8.350.1)].

7.2 Average End-to-End Data Rate Analysis with Optimal VLC Bias Design

Suppose that the LED source transmits data to the relay with rate R_1 bits/second/Hz and the relay retransmits the data to the mobile terminal with rate R_2 bits/second/Hz. The data rate of the whole system will be limited by the smaller data rate between the two hops, given by $R = \min(R_1, R_2)$, where R_1 is given by the lower bound on the capacity of the VLC channel [81] as $R_1 = \log_2\left(1 + \frac{e}{2\pi}\gamma_1\right)$, and R_2 is given by the well-known Shannon formula as $R_2 = \log_2(1 + \gamma_2)$. We assume that the signals transmitted over two hops have the same bandwidth. It is clear that increasing the DC bias B will lead to an increase in the amount of harvested energy at the relay which leads to an increase in the data rate of the second-hop RF channel R_2. However, to transmit more information over the first-hop VLC channel, we need to reduce the DC bias B to increase the received electrical power P_r^e and thus increase R_1. Thus, the optimal DC bias needs to be designed. In what follows, we present two methods to design the optimal VLC DC bias.

7.2.1 Optimal VLC Bias Design Based on Average End-to-End Data Rate (ADR-Based method)

Since the first-hop VLC channel is static channel in its nature and the second-hop RF channel is dynamic channel, then the average end-to-end data rate, denoted by $\bar{R}$, can be obtained by using the law of total expectation as:

$$\begin{aligned}\bar{R} &= E[\min(R_1, R_2)] \\ &= E[R_1|R_1 \leq R_2]\mathrm{P_r}[R_1 \leq R_2] + E[R_2|R_1 > R_2]\mathrm{P_r}[R_1 > R_2] \\ &= R_1[1 - F_{\gamma_2}(c)] + F_{\gamma_2}(c)\int\limits_0^c \log_2(1+\gamma_2)\, f_{\gamma_2}(\gamma_2)d\gamma_2,\end{aligned} \tag{7.11}$$

where $c = 2^{R_1} - 1$. To evaluate the integral part of (7.11), after the substitution with (7.9), we first express $\log_2(1+\gamma_2)$ as $\ln(1+\gamma_2)/\ln(2)$. Then, by applying the integration by part rule, and using [53, Eqs. (2.33.10) and (8.352.7)], along with the binomial expansion rule, $\bar{R}$ can be expressed in this case in a closed form as:

$$\bar{R} = R_1[1 - F_{\gamma_2}(c)] - \frac{F_{\gamma_2}(c)}{\Gamma(m)\ln(2)}\Bigg\{\ln(1+c)\Gamma\left(m, \frac{mc}{\bar{\gamma}_2}\right) - (m-1)!\exp\left(\frac{m}{\bar{\gamma}_2}\right) \sum_{i=0}^{m-1}\sum_{k=0}^{i}\frac{(-m/\bar{\gamma}_2)^{i-k}}{k!(i-k)!}\left[\Gamma\left(k, \frac{m}{\bar{\gamma}_2}\right) - \Gamma\left(k, \frac{m(1+c)}{\bar{\gamma}_2}\right)\right]\Bigg\}, \tag{7.12}$$

where $\Gamma(\cdot,\cdot)$ is the upper incomplete Gamma function defined in [53, Eq. (8.350.2)]. The optimal bias B_A^*, which maximizes the average end-to-end data rate $\bar{R}$ can be obtained by solving $\frac{\partial \bar{R}}{\partial B} = 0$ for B. However, it will be difficult to obtain the optimal B_A^* in closed form.

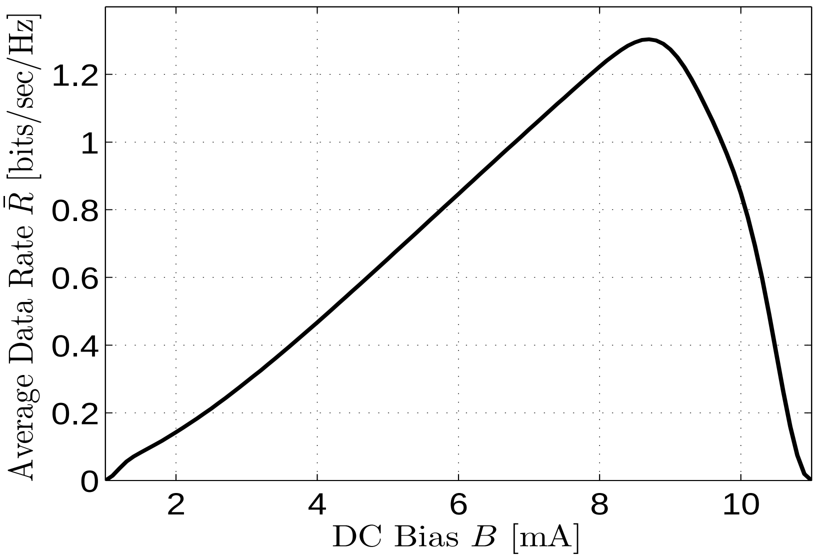

Figure 7.3: Average data rate for ADR-based method with $d_2 = 10m$ and $m = 1$.

It is clear from Fig. 7.3 that $\bar{R}$ is a unimodal function in B. Thus, we can treat the problem as one-dimensional optimization problem with uncertainty range of $[I_L, I_H]$, and use numerical methods, such as Golden-section search method [68], to search for the optimal B_A^*.

7.2.2 Optimal VLC Bias Design Based on Instantaneous End-to-End Data Rate (IDR-Based method)

To maximize the instantaneous end-to-end data rate R, we need to solve the following optimization problem:

$$\begin{aligned} \underset{B}{\text{maximize}} \quad & R(B) = \min(R_1, R_2) \\ \text{subject to} \quad & B \in [I_L, I_H]. \end{aligned}$$

Normally, such max-min problem has solution at $R_1 = R_2$, which when we consider the constraint $B \in [I_L, I_H]$, leads to the solution:

$$B_1 = \frac{c_1 I_H - \sqrt{c_1 c_2 I_H^2 |h_2|^2}}{c_1 - c_2 |h_2|^2}, \tag{7.13}$$

with $c_1 = eG_2\sigma_2 T_2 I_0$ and $c_2 = 1.5\pi\sigma_1^2(T_1+T_2)V_T$, where we plot R_1 and R_2 as function of B in Fig. 7.4 using parameters given in section 7.3.

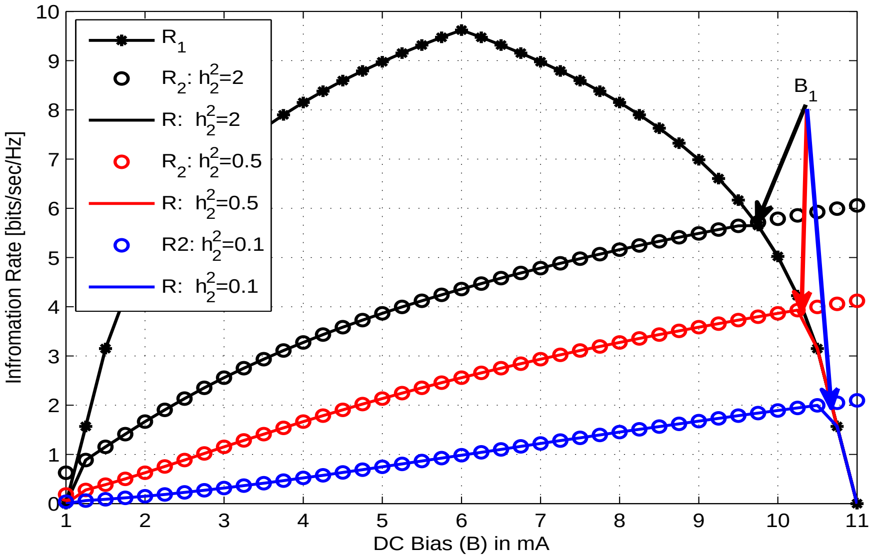

Figure 7.4: System data rates with $d_2 = 10$m.

When second-hop RF channel gain $|h_2|^2$ increases (i.e., the quality of the second-hop RF channel improves), the intersection point of R_2 with R_1 (whose projection on the DC bias B-axis equals to B_1) moves up towards the peak of R_1 and thus the end-to-end data rate R of the whole system increases with a decrease in the required

DC bias B. However, the maximum end-to-end data rate is constrained by the peak value of R_1, which corresponds to the case when $B_1 = (I_L + I_H)/2$ (equals to 6 mA in Fig. 7.4 that occurs when:

$$|h_2|^2 \equiv |h_2|_T^2 = \frac{\left(\sqrt{c_1 c_2 I_H^2} - \sqrt{c_1 c_2 I_H^2 - 4c_1 c_2 c_m (I_H - c_m)}\right)^2}{4c_2^2 c_m^2}, \tag{7.14}$$

where $c_m = (I_L + I_H)/2$. Thus, the optimal DC bias, denoted by B_I^*, in this case can be chosen according to the following criteria:

$$B_I^* = \begin{cases} B_1, & \text{if } |h_2|^2 \leq |h_2|_T^2 \\ \frac{I_L+I_H}{2}, & \text{if } |h_2|^2 > |h_2|_T^2, \end{cases} \tag{7.15}$$

with optimum data rate $R(B_I^*) = R_1(B_I^*) = R_2(B_I^*)$. Accordingly, the average end-to-end data rate, with optimal DC bias B_I^* chosen based on the instantaneous RF channel power gain $|h_2|^2$, is obtained by averaging the optimal data rate $R(B_I^*)$ over the distribution of $|h_2|^2$ as:

$$\bar{R} = \int_0^{|h_2|_T^2} R(B_I^*) f_{|h_2|^2}(|h_2|^2) d|h_2|^2 + \int_{|h_2|_T^2}^{\infty} R(B_I^*) f_{|h_2|^2}(|h_2|^2) d|h_2|^2. \tag{7.16}$$

The first integral part of (7.16) can be evaluated numerically as it is hard to be obtained in closed form. The second integral part of (7.16), can be given in a closed form as $\frac{\Gamma\left(m, m|h_2|_T^2\right)}{\Gamma(m)} R_1|_{B_I^*=(I_L+I_H)/2}$ by using [53, Eq. (3.351.2)].

7.3 Numerical Results

In this section, we present numerical examples to illustrate our analysis by using the parameters given in Table 7.1 [45, 79]. We assume $T_1 = T_2 = 1$ second.

In Fig. 7.5, we plot the average data rate of the whole system as a function of the distance d_2 from the relay to the mobile terminal. For the ADR-based method, the RF channel path loss G_2 varies with d_2. For each value of G_2, we use the Golden-section search method with an accuracy of 10^{-6} to find the optimal DC bias B_A^* and the corresponding average end-to-end data rate to obtain the ADR-based curve. For the IDR-based method, we use (7.16) to obtain the IDR-based curve. It can be seen from

Table 7.1: Parameters of VLC and RF subsystems

Parameter	Symbol	Value
Single LED Power	P_{LED}	$20\ mW/A$
Minimum Bias Current	I_L	$1\ mA$
Maximum Bias Current	I_H	$11\ mA$
Semi-angle at Half Luminance	$\phi_{1/2}$	$15\ deg.$
Irradiance Angle	ϕ	$20\ deg.$
Incidenece Angle	ψ	$20\ deg.$
VLC Channel Range	d_1	$1.5\ m$
Physical Area of Photo-detector	A_r	$0.04\ m^2$
Photo-detector Responsivity	η	$0.53\ A/W$
Number of LEDs in the Array	N	10
VLC Noise Power Spectral Density	N_0	$10^{-21}\ A^2/Hz$
Modulation Bandwidth for LED	W	$40\ MHz$
Dark Saturation Current of Photo-detector	I_0	$10^{-9}A$
RF Noise Power	σ_2	$10^{-8}\ W$
RF Path Loss Exponent	γ	1.6

Fig. 7.5 that, the average data rate decreases as d_2 increases, using either ADR-based method or IDR-based method in choosing the optimal DC bias. However, the average end-to-end data rate had shown improvement when the optimal DC bias is chosen based on the instantaneous RF channel power gain $|h_2|^2$ (IDR-based method) over the method when the optimal DC bias is chosen based on RF channel path loss G_2 (ADR-based method), especially, at smaller distances between the mobile terminal and the relay. As the distance d_2 increases, the performance of the two methods approach to each other. Note that, the performance advantage of the IDR-based method comes at the cost of requiring instantaneous channel knowledge of $|h_2|^2$ at the LED source to calculate the optimal DC bias B_I^* according to the criteria given by (7.15).

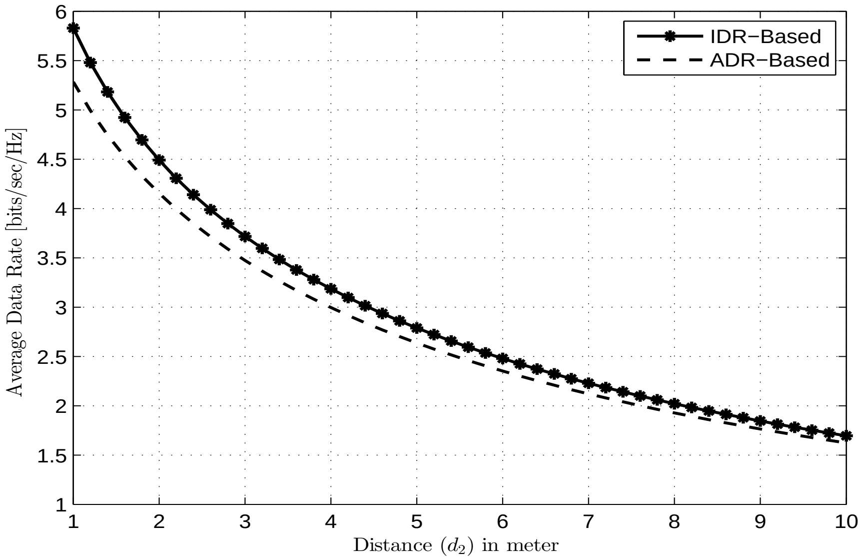

Figure 7.5: System average data rate with optimal DC bias.

7.4 Summary

In this chapter, we presented a dual-hop heterogeneous communication system that composed of two different types of communication links, specifically, VLC and RF links. A relay between the two hops is able to harvest energy from the VLC link and uses it to retransmit the data to a mobile terminal over the RF link. The DC bias imposed on the electrical signal at the LED source, before being transmitted over the first-hop VLC channel, affects both the power of the transmitted electrical signal over the first-hop VLC channel and the amount of energy harvested by the relay. Thus, it affects the data rates of both hops of the hybrid VLC/RF system. Two methods of designing the optimal DC bias were introduced and the corresponding end-to-end average data rate of the system in each case was analyzed. One method is based on the second-hop RF channel's instantaneous power gain (IDR-based method) and the other one is based on the second-hop RF channel's path loss (ADR-based method). The IDR-based method was shown to give better average data rate performance over the ADR-based method. However, the performance advantage of the IDR-based method comes at the cost of requiring instantaneous second-hop RF channel knowledge at the LED source.

Chapter 8

Conclusions and Future Work

In this chapter, we conclude the thesis by summarizing the accomplished work and suggesting some potential further research topics.

8.1 Conclusions

In this thesis, we first presented and analyzed a new transmission scheme for hybrid FSO/RF systems. This transmission scheme is based on adaptive combining. The exact CDF of the received SNR for the proposed hybrid FSO/RF system with adaptive combining is obtained, which is used to study the system outage performance. Hybrid FSO/RF system with adaptive scheme had shown improved outage performance compared to FSO-only and RF-only systems in all weather conditions and atmospheric turbulence regimes.

To effectively use the available resources of hybrid FSO/RF systems with adaptive combining scheme, we also presented two new joint adaptive schemes. One is joint adaptive modulation and adaptive combining scheme. We obtained a closed-form of the exact CDF of the received SNR for the proposed adaptive hybrid FSO/RF system. This proposed adaptive hybrid FSO/RF system had shown improved spectral efficiency and outage performance compared to that of switch-over hybrid FSO/RF and FSO-only systems, while maintaining good average BER. The other joint adaptive scheme is joint power adaptation and adaptive combining scheme. In this adaptive scheme, two new power adaptation policies that are based on a modified TCI were implemented on the RF link of the hybrid FSO/RF system. These two policies were defined as γ_{RF}-based TCI adaptation policy and $\gamma_{RF} + \gamma_{FSO}$-based TCI adaptation policy. Closed form for the system outage probability for each policy was derived. Hybrid FSO/RF system with this joint adaptive scheme had shown improved outage performance compared to outage performance of the same system without power adaptation, while conserving RF power. Also, we have showed that γ_{RF}-based TCI adaptation policy achieves better outage performance than $\gamma_{RF} + \gamma_{FSO}$-based TCI adaptation policy.

Considering a multi-user scenario, we proposed and analyzed a new P2MP Hybrid FSO/RF Network. In this network, a common backup RF link is used by the central node for data transmission to any remote node in case of the failure of its corresponding FSO link. We developed a discrete-time Markov chain model for the transmit buffer of the link between the central node and a single remote node (tagged node). Studying the tagged node allowed us to investigate several performance criteria such as throughput from central node to the tagged node, the average transmit buffer size, the symbol queuing delay in the transmit buffer, the efficiency of the queuing system, the symbol loss probability, and the RF link utilization. Using a common backup RF link in the P2MP Hybrid FSO/RF network had achieved considerable performance improvement over the P2MP FSO-only network.

To extend the coverage of indoor VLC systems, we introduced a dual-hop VLC/RF transmission system with an energy harvesting relay. We proposed two approaches for energy harvesting at the relay between the two hops. In the first approach, the relay harvests indoor light energy. Considering QoS constraint of a strict end-to-end time delay, we analyzed the probability of data packet loss. The parameter α that determines the time available for excess light energy harvesting and the time available for data packet retransmission was found to affect the system performance. An optimal value of α that minimizes packet loss probability was found to be independent of the mobile terminal distance and the path loss exponent.

In the second approach, the relay harvests energy from the received optical signal. The amount of harvested energy is related to the DC bias that was imposed on the electrical signal at the LED source. Two methods of designing the optimal DC bias were introduced and the corresponding end-to-end average data rate of the system in each case was analyzed. One method is based on the second-hop RF channel's instantaneous power gain (IDR-based method) and the other one is based on the second-hop RF channel's path loss (ADR-based method). The IDR-based method was shown to give better average data rate performance over the ADR-based method at the cost of requiring instantaneous second-hop RF channel knowledge at the LED source.

8.2 Future Work

The ideas proposed in this thesis can be expanded in the future in different directions:

1. We have focused in this thesis, mainly in chapters 2-5, for outdoor data transmission on the FSO systems which require line-of-sight. UV systems can achieve outdoor NLOS data transmission. However, there are a lot of challenges in using UV systems. Many open research topics in this field including channel modeling, performance limitation, trade-off studies such as data rate and communication range trade-offs, and UV transceiver design can be considered in future work.

2. We have assumed in chapter 5 that, when more than one FSO link fail, the central node will use the RF link to communicate with one of the corresponding remote nodes on an equal priority basis. Using other protocols such as unequal priority protocol, round robin protocol, random delay protocol, and delay aware scheduling protocol will affect the Markov chain model and thus the system performance. These arbitration/scheduling protocols can be considered in future work.

3. We have introduced a dual-hop VLC/RF system in chapters 6 and 7. In this system, we assumed that LED source already have the data to be transmitted. However, the LED source should access the backbone information network to acquire the data. Power Line Communication (PLC) systems utilize the ubiquitous power line network to power the LED sources while serving as the backbone network for the VLC systems. Hybrid PLC/VLC/RF systems can be considered in future work.

Appendix A

Proof of Proposition 1

We had adopted the distribution fitting approach to validate proposition 1. First we generate one million log-normally distributed random numbers x that represent the samples of I_{sc} with mean $= \mu_x$ and variance $= \sigma_x^2$. The histogram of I_{sc} and its log-normal distribution fitting is shown in Fig. A.1a. By using these samples, we generate another set of samples y for the output power P_h by using the relationship $y = 0.75V_t\ x \ln\left(\frac{x}{I_0} + 1\right)$. By drawing the histogram of P_h, it can be observed that it fits a log-normal distribution as shown in Fig. A.1b. The red curve in Fig. A.1b is the log-normal distribution fitting to the histogram for two different values of I_0. This red curve is plotted by using the MATLAB function `histfit`. Other distributions were attempted but it was found that the log-normal distribution provides the best fit. Thus, we conclude that P_h follows a a log-normal distribution $P_h \sim \mathrm{LN}(\mu_y, \sigma_y)$, where μ_y and σ_y are the mean and the standard deviation of P_h.

Also, since I_{sc} is in the order of $10^{-3} \sim 10^{-6}$ Ampere [77], which is very large compared to I_0, then the term $\ln(\frac{I_{sc}}{I_0} + 1)$ in (6.10) tends to be constant and P_h in (6.10) will be a monotonically increasing function in I_{sc}. Thus, it is logic to find that the output power P_h has the same statistical distribution as I_{sc}, i.e., log-normal distribution.

Defining the function $f(x) = P_h = 0.75V_t\ x \ln\left[\frac{x}{I_0} + 1\right]$, then μ_y is calculated as [78]:

$$\mu_y = \int_0^\infty f(x) f_{I_{sc}}(x) dx, \tag{A.1}$$

where $f_{I_{sc}}(x)$ is the PDF of I_{sc} given by (6.11), and σ_y is calculated approximately as [78]:

$$
\begin{aligned}
\sigma_y &\approx \sigma_x \ \frac{df(x)}{dx}\ |_{x=\mu_x} \\
&= 0.75\ \sigma_x\ V_t \left[\frac{x}{x+I_0} + \ln\left(\frac{x}{I_0}+1\right)\right]_{x=\mu_x} \\
&= 0.75\ \sigma_x\ V_t \left[\frac{\mu_x}{\mu_x+I_0} + \ln\left(\frac{\mu_x}{I_0}+1\right)\right].
\end{aligned}
\tag{A.2}
$$

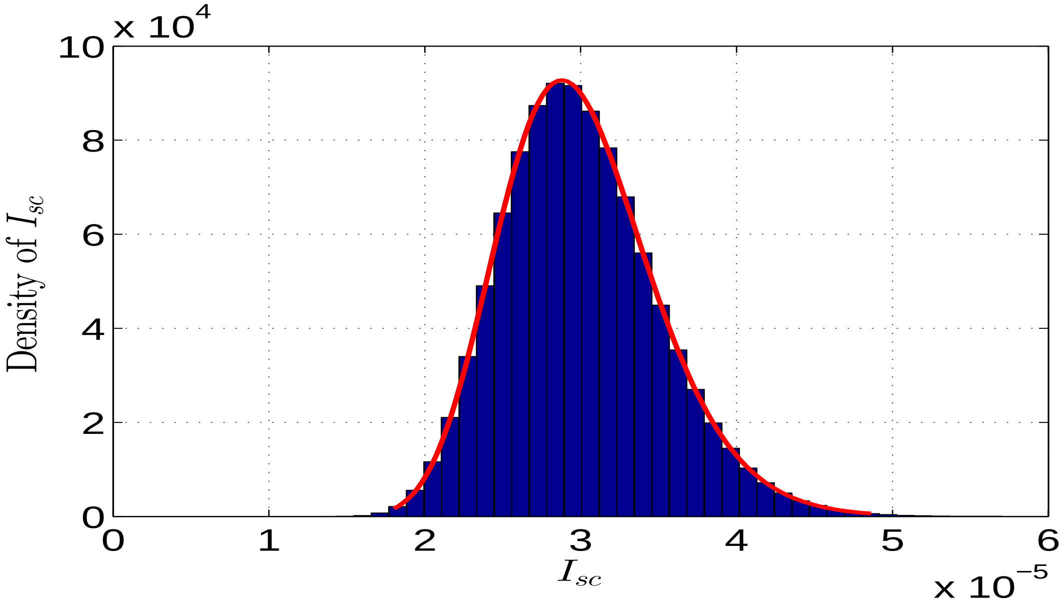

(a) Histogram of I_{sc} assuming $\mu_x = 3 \times 10^{-5}$ Ampere, $\sigma_x = 0.5 \times 10^{-5}$ Ampere.

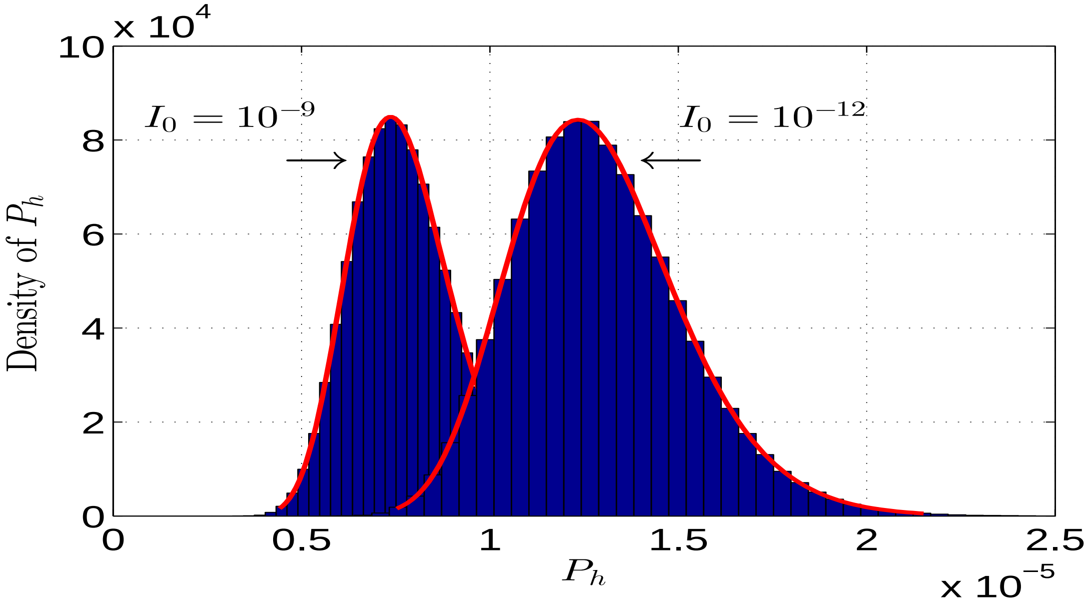

(b) Histogram of corresponding P_h for $I_0 = 10^{-9}$ and 10^{-12} Amperes.

Figure A.1: Histograms of I_{sc} and P_h and their log-normal distribution curve fitting.

Bibliography

[1] H. Henniger, and O. Wilfert, “An introduction to free-space optical communications”, *Radio Engineering*, vol. 19, no. 2, pp. 203–212, June 2010.

[2] D. M. Reilly, D. T. Moriarty, and J. A. Maynard, “Unique properties of solar blind ultraviolet communication systems for unattended ground sensor networks”, *SPIE Proceedings, Unmanned/Unattended Sensors and Sensor Networks*, vol. 5611, November 2004.

[3] P. M. Butala, H. Elgala, T. D.C. Little, and P. Zarkesh-Ha, “Multi-wavelength visible light communication system design”, *2014 IEEE Globecome Workshops (GC Wkshps)*, Austin, TX, December 2014.

[4] A. Majumdar and J. Ricklin, “Free-Space Laser Communications, principles and Advances”, *Springer, NY, USA*, 2008.

[5] E. Leitgeb, S. S. Muhammad, C. Chlestil, M. Gebhart, and U. Birnbacher, “Reliability of FSO links in next generation optical networks”, *Proceedings of 2005 7th International Conference Transparent Optical Networks (Volume: 1)*, July 2005.

[6] D. Schulz, V. Jungnickel, C. Alexakis, M. Schlosser, J. Hilt, A. Paraskevopoulos, L. Grobe, and P. Farkas, “Robust Optical Wireless Link for the Backhaul and Fronthaul of Small Radio Cells”, *Journal of Lightwave Technology*, vol. 34, no. 6, pp. 1523–1532, March 2016.

[7] E. Leitgeb, M. Loschnigg, U. Birnbacher, G. Schwarz, and A. Merdonig, “High reliable optical wireless links for the last mile access”, *10th Anniversary International Conference on Transparent Optical Networks*, June 2008, Athens.

[8] F. Ahdi, and S. Subramaniam, “Optimal placement of FSO relays for network disaster recovery”, *2013 IEEE International Conference on Communications (ICC)*, June 2013, Budapest.

[9] M. A. Khalighi and M. Uysal, "Survey on free space optical communication: A communication theory perspective," *IEEE Communication Surveys and Tutorial*, vol. 16, no. 4, pp. 2231–2258, Fourth quater 2014.

[10] N. Kumar, V. K. Jain, and S. Kar, "Evaluation of the performance of FSO system using OOK and M-PPM modulation schemes in inter-satellite links with turbo codes," *2011 International Conference on Electronice, Communication and Computing Technologies (ICECCT)*, September 2011, Pauls Nagar.

[11] M. R. Bhatnagar, and M. K. Arti, "Performance Analysis of Hybrid Satellite-Terrestrial FSO Cooperative System", *IEEE Photonics Letters*, vol. 25, no. 22, pp. 2197–2200, November 2013.

[12] S. Hranilovic and F. R. Kschischang, "Optical intensity-modulated direct detection channels: Signal space and lattice codes", *IEEE Transactions on Information Theorey*, vol. 49, no. 6, pp. 1385–1399, June 2003.

[13] Mingbo Niu, Xuegui Song, Julian Cheng, and Jonathan F. Holzman, "Performance Analysis of Coherent Wireless Optical Communications With Atmospheric Turbulence," *OSA Optics Express*, vol. 20, pp. 6511–6520, March 2012.

[14] I. S. Ansari, F. Yilmaz, and M.-S. Alouini, "Performance analysis of free-space optical links over Mlaga ($\mathcal{M}$) turbulence channels with pointing errors", *IEEE Transactions on Wireless Communications*, vol. 15, no. 1, pp. 91–102, January 2016.

[15] J. Park, E. Lee, C.-B. Chae, and G. Yoon, "Impact of pointing errors on the performance of coherent free space optical systems," *IEEE Photonics Technology Letters*, vol. 28, no. 2, pp. 181–184, January 2016.

[16] S. Arnon, "Effects of atmospheric turbulence and building sway on optical wireless-communication systems", *Optics Letters*, vol.28, no. 2, pp. 129–131, 2003.

[17] A. A. Farid, and S. Hranilovic, "Outage capacity optimization for free-space optical links with pointing errors", *Journal of Lightwave Technology*, vol. 25, no. 7, pp. 1702–1710, July 2007.

[18] D. K. Borah, and D. G. Voelz, "Pointing error effects on free-space optical communication links in the presence of atmospheric turbulence", *Journal of Lightwave Technology*, vol.27, no. 18, pp. 3965–3973, September 2009.

[19] E. Zedini, A. Chelli and M-S. Alouini, “On the performance analysis of hybrid ARQ with incremental redundancy and with code combining over free-space optical channels with pointing errors”, *IEEE Photonics Journal*, vol. 6, no. 4, pp. 1–19, August 2014.

[20] A. Al-Habash, L. C. Andrews, and R. L. Philips, “Mathematical model for the irradiance probability density function of a laser beam propagating through turbulent media”, *Opt. Eng.*, vol. 40, no. 8, pp. 1554–1562, August 2001.

[21] N. Guo, R. Qiu, S. Mo, and K. Takahashi,“60-GHz millimeter-wave radio: principle, technology, and new results, *EURASIP Journal of Wireless Communication and Networking*, pp. 1–7, January 2007

[22] M. Usman, H-C. Yang and M-S. Alouini, “Practical switching-based hybrid FSO/RF transmission and its performance analysis, *IEEE Photonics Journal*, vol. 6, no. 5, pp. 1–13, October 2014.

[23] S. Vangala, and H. P.-Nik, “Optimal hybrid RF-wireless optical communication for maximum efficiency and reliability”, in *2007 41st Annual Conference on Information Science and Systems (CISS’07)*, March 2007, Baltimore, MD.

[24] N. D. Chatzidiamantis, G. K. Karagiannidis, E. E. Kriezis, and M. Matthaiou, “Diversity combining in hybrid RF/FSO systems with PSK modulation”, in *2011 IEEE International Conference on Communication (ICC)*, June 2011, Kyoto.

[25] A. Kamboj, R. Mallik, M. Agrawal, and R. Schober, “Diversity combining in FSO systems in presence of non-Gaussian noise”, in *2012 International Conference on Signal Processing and Communications (SPCOM)*, July 2012, Bangalore.

[26] B. He and R. Schober, “Bit-interleaved coded modulation for hybrid RF/FSO systems”, *IEEE Transactions on Communications*, vol. 57, no. 12, pp. 3753–3763, December 2009.

[27] T. Rakia, H.-C. Yang, M.-S. Alouini, and F. Gebali, “Outage Analysis of Practical FSO/RF Hybrid System with Adaptive Combining”, *IEEE Communication Letters*, vol. 19, no. 8, pp. 1366–1369, August 2015.

[28] N. Letzepis, K. D. Nguyen, A. G. Fabregas, and W. G. Cowley, “Outage analysis of the hybrid free-space optical and radio-frequency channel”, *IEEE Journal on Selcected Areas in Communications*, vol. 27, no. 9, pp. 1709–1719, December 2009.

[29] Y. Tang, M. B.-Pearce, and S. G. Wilson, “Link adaptation for throughput optimization of parallel channels with application to hybrid FSO/RF systems”, *IEEE Transactions on Communications*, vol. 60, no. 9, pp. 2723–2732, September 2012.

[30] V. V. Mai, and A. T. Pham, “Adaptive Multi-Rate Designs for Hybrid FSO/RF Systems over Fading Channels”, in *2014 IEEE Globecom Workshops (GC Wkshps)*, 2014, Austin, TX.

[31] T. Rakia, H.-C. Yang, F. Gebali, and M.-S. Alouini, “Joint Adaptive Modulation and Combining for Hybrid FSO/RF Systems”, *15th IEEE International Conference on Ubiquitous Wireless Broadband, ICUWB’2015* , Montreal, Canada, 2015.

[32] A. Goldsmith, Wireless Communication, 5th ed., *Cambridge University Press, USA*, 2005.

[33] T. Rakia, H.-C. Yang, M.-S. Alouini, and F. Gebali, “Power Adaptation Based on Truncated Channel Inversion for Hybrid FSO/RF Transmission with Adaptive Combining”, *IEEE Photonics Journal*, vol. 7, no. 4, pp. 1–12, August 2015.

[34] T. Rakia, H.-C. Yang, F. Gebali, and M.-S. Alouini, “Outage Performance of Hybrid FSO/RF System with Low-Complexity Power Adaptation”, *IEEE Global Communications Conference, Globecom’2015*, San Deigo, USA, 2015.

[35] H. Moradi, M. Falahpour, H. H. Refai, P. G. LoPresti, and M. Atiquzzaman, “On the capacity of hybrid FSO/RF links”, *IEEE Globel Tecommunication Conference (Globecom’ 2010).*, December 2010, Miami, FL.

[36] N. Letzepis, K. Nguyen, A. G. Fabregas, and W. Cowley, “Outage analysis of the hybrid free-space optical and radio-frequency channel”, *IEEE Journal on Selected Areas in Communications*, vol. 27, no. 9, pp. 1709–1719, December 2009.

[37] P. Wang, N. Xiang, Q. Gao, R. Wang, L. Guo, and Y. Yang“On the performances of Nth best user selection scheme in multiuser diversity free-space optical systems over exponentiated Weibull turbulence channels,” *IEEE Photonics Journal*, vol. 8, no. 2, April 2016.

[38] S. Zhalehpour, M. Uysal, O. A. Dobre, and T. Ngatched“Outage capacity and throughput analysis of multiuser FSO systems,” *2015 IEEE 14th Canadian Workshop on Information Theory (CWIT)*, July 2015, St. John’s, NL.

[39] W. Du, Z. Ji, and Z. Wang, "Self-adaptive truncated binary exponential back off scheme for WiMAX P2MP network with heavy traffic", *11th IEEE Singapore International Conference on Communication Systems (ICCS 2008)*, November 2008, Singapore.

[40] C. Hongda, W. Chunhui, L. Honglei, C. Xiongbin, G. Zongyu, C. Shigang, and W. Qin, "Advances and prospects in visible light communications", *Journal of Semiconductors*, vol. 37, no. 1, pp. 1–10, January 2016.

[41] S. Shao, A. Khreishah, and I. Khalil, "Joint link scheduling and brightness control for greening VLC-based indoor access networks", *Journal of Optical Communications and Networking* vol. 8, no. 3, pp. 148–161, March 2016.

[42] M-S. Kim, I-S. Jang, S-K. Lim, and T-K. Kang, "Implementation of ZigBee-VLC system to support light control network configuration", *18th International Conference on Advanced Communication Technology (ICACT)*, Febrauary 2016, Pyeongchang.

[43] F. Delgado, I. Quintana, J. A. Rabadan, C. Quintana, and R. Perez-Jimenez, "Design and Implementation of an Ethernet-VLC Interface for Broadcast Transmissions," *IEEE Communication Letters*, vol.14, no. 12 298–299, pp. 1089–1091, December 2010.

[44] Y.-J. Zhu, W.-Y. Wang, and G. Xin, "Faster-than-Nyquist signal design for multiuser multicell indoor visible light communications", *IEEE Photonics Journal*, vol. 8, no. 1, February 2016.

[45] D. A. Basnayaka and H. Haas, "Hybrid RF and VLC systems: Improving user data rate performance of VLC systems", *2015 IEEE 81st Vehicular Technology Conference (VTC Spring)*, Glasgow, May 2015.

[46] M. B. Rahaim, A. M. Vegni, and T. D.C. Little, "A hybrid radio frequency and broadcast visible light communication system", *2nd IEEE Workshop on Optical Wireless Communications*, pp. 792 –796, Houston, Tx, December 2011.

[47] K. Cui, J. Quan, and Z. Xu, "Performance of indoor optical femtocell by visible light communication," *Optics Communications*, vol. 298–299, pp. 59–66, July 2013.

[48] B. Li, J. Wang, R. Zhang, H. Shen, C. Zhao, and L. Hanzo, “Multiuser MISO transceiver design for indoor downlink visible light communication under per-LED optical power constraints,” *IEEE Photonics Journal*, vol. 7, no. 4, August 2015.

[49] Z. Wang, D. Tsonev, S. Videv, and H. Haas, “Towards self-powered solar panel receiver for optical wireless communication”, *2014 IEEE International Conference on Communications (ICC)*, pp. 3348–3353, June 2014.

[50] C. Li, W. Jia, Q. Tao, and M. Sun, “Solar cell phone charger performance in indoor environment,” *2011 IEEE 37th Annual Northeast Bioengineering Conference (NEBEC)*, Troy, NY, April 2011.

[51] A.S. Weddell, N.R. Harris, and N.M. White, “An efficient indoor photovoltaic power harvesting system for energy-aware wireless sensor nodes”, in *Proceedings of the Eurosensors XXII*, Dresden, Germany, September 2008.

[52] J. Li, J. Q. Liu, and D. P. Taylor, “Optical Communication Using Subcarrier PSK Intensity Modulation Through Atmospheric Turbulence Channels,” *IEEE Transactions on Communications*, vol. 55, no. 8, pp. 1598–1606, August 2007.

[53] I. S. Gradshteyn, and I. M. Ryzhik, Table of Integrals, Series, and Products, *Elsevier Acadimic Press, USA*, 2007.

[54] L. C. Andrews, and R. L. Phillips, *Laser Beam Propagation Through Random Media*, 2nd ed., SPIE Optical Engineering Press, Washington, USA, 2005.

[55] V. S. Adamchik, and O. I. Marichev, “The algorithm for calculating integrals of hypergeometric type functions and its realization in REDUCE system”, *International Symposia on Symbolic and Algebraic Computation (ISSAC’90)*, pp. 212–224, Tokyo, Japan, 1990.

[56] I. Wolfram Research,*Mathematica Edition*: Version 8.0. Champaign, Illinois: Wolfram Research, Inc., 2010.

[57] S. Bloom and D. J. T. Heatley, “The last mile solution: Hybrid FSO radio,” *white paper, AirFiber Inc., 802-0008-000 M-A1*, pp. 1–20, May 2002.

[58] H. A. Suraweera, P. J. Smith, and J. Armstrong, “Outage probability of cooperative relay networks in Nakagami-m fading channels”, *IEEE Communication Letters*, vol. 10, no. 12, pp. 834–836, December 2006.

[59] M. K. Simon, and M.- S. Alouini, *Digital Communication over Fading Channels*, John Wiley and Sons Inc., USA, 2005.

[60] X. Tang, Z. Ghassemlooy, S. Rajbhandari, W. O. Popoola, and C. G. Lee, "Coherent polarization shift keying modulated free space optical links over a Gamma-Gamma turbulence channel", *American Journal of Engineering and Applied Sciences*, vol. 4, no. 4, pp. 520–530, January 2012.

[61] B. T. Vu, N. T. Dang, T. G. Thang, and A. T. Pham, "Bit error rate analysis of rectangular QAM/FSO systems using APD receiver over atmospheric turbulence channels", *Journal of Optical Communication and Networking*, vol. 5, no. 5, pp. 437–446, April 2013.

[62] X. Lei, P. Fan, and L. Hao, "Exact symbol error probability of general order rectangular QAM with MRC diversity reception over Nakagami-m fading channels", *IEEE Communication Letters*, vol. 11, no. 12, pp. 958–960, December 2007.

[63] M. Niu, J. Cheng, and J. F. Holzman, "Error rate analysis of M-ary coherent free-space optical communication systems with K-distributed turbulence", *IEEE Transactions on Commununications*, vol. 59, no. 3, pp. 664–668, March 2011.

[64] M. Niu, J. Cheng, and J. F. Holzman, "Error rate performance comparison of coherent and subcarrier intensity modulated optical wirelss communications", *Journal of Optical Communication and Networking*, vol. 5, no. 6, pp. 554–564, June 2013.

[65] H. G. Sandalidis, T. A. Tsiftsis, G. K. Karagiannidis, and M. Uysal, "BER performance of FSO links over strong atmospheric turbulence channels with pointing errors", *IEEE Communication Letters*, vol. 12, no. 1, pp. 44–46, January 2008.

[66] I. Ansari, F. Yilmaz, and M-S. Alouini, "Performance analysis of FSO links over unified Gamma-Gamma turbulence channels", Proceedings *IEEE Vehicular Technology Conference (VTC Spring'2015)*, Glasgow, Scotland, UK, May 2015.

[67] H-C. Yang, and M-S. Alouini, *Order Statistics in Wireless Communication*, Cambridge University Press, UK, 2011.

[68] A. Antoniou, and W.-S. Lu *Practical Optimization: Algorithms and Engineering Applications*, Marcel Springer, USA, 2007.

[69] A. Lapidoth, S. M. Moser, and M. A. Wigger, “On the capacity of free-space optical intensity channels”, *IEEE Transactions on Information Theory*, vol. 55, no. 10, pp. 4449– 4461, October 2009.

[70] I. E. Lee, Z. Ghassemlooy, W. P. Ng, and M. Uysal, “ Performance analysis of free space optical links over turbulence and misalignment induced fading channels”, *8th International Symposium on Communication Systems, Networks and Digital Signal Processing (CSNDSP)*, pp. 1–6, Poznan, Poland, 2012.

[71] A. Jeffrey, Handbook of Mathematical Formulas and Integrals, *Academic Press*, San Diego, 1995.

[72] F. Gebali, Analysis of Computer Networks, second edition, *Springer*, New York, 2015.

[73] F.-M. Wu, C.-T. Lin, C.-C. Wei, C.-W. Chen, H.-T. Huang, and C.-H. Ho, “1.1-Gb/s white-LED-based visible light communication employing carrier-less amplitude and phase modulation”, *IEEE Photonics Technology Letters*, vol. 24, no. 19, pp. 1730–1732, October 2012.

[74] T.S. Rappaport, *Wireless Communications Principles and Practice*, 2nd ed., Prentice Hall, New Jersey, 2002.

[75] Gilbert M. Masters, *Renewable and Efficient Electric Power Systems, 2nd ed.*, John Wiley and sons, Inc., New Jersey, 2014.

[76] M. Abramowitz and I. A. Stegun, Eds., *Handbook of Mathematical Functions: with Formulas, Graphs, and Mathematical Tables*, Dover Publications, New York, 1965.

[77] C. Carvalho, and N. Paulino, *CMOS Indoor Light Energy Harvesting System for Wireless Sensing Applications*, Springer, Switzerland, 2016.

[78] B. M. Ayyub, and R. H. McCuen, *Probability, Statistics, and Reliability for Engineers and Scientists, 3th ed.*, CRC press, USA, 2011.

[79] P. Fahamuel, J. Thompson, and H. Haas, “Improved indoor VLC MIMO channel capacity using mobile receiver with angular diversity detectors,” *2014 IEEE Global Communication Conference*, Austin, TX, December 2014

[80] T. Komine and M. Nakagawa, "Fundamental analysis for visible-light communication system using LED lights," *IEEE Transactions on Consumer Electronics*, vol. 50, no. 1, pp. 100–107, February 2004.

[81] J.-B. Wang, Q.-S. Hu, J. Wang, M. Chen and J.-Y. Wang, "Tight bounds on channel capacity for dimmable visible light communications," *Journal of Light wave Technology*, vol. 31, no.23, pp. 3771–3779, December 2013.